

UNIVERSITY OF TRENTO  
Department of Physics



# Spin dynamics in two-component Bose-Einstein condensates

DOCTORAL THESIS  
SUBMITTED TO THE  
DOCTORAL SCHOOL OF PHYSICS – XXXIII CYCLE  
BY

*Arturo Farolfi*

FOR THE DEGREE OF  
DOCTOR OF PHILOSOPHY – DOTTORE DI RICERCA

Supervisor: Prof. Gabriele FERRARI  
Referees: Prof. Markus K. OBERTHALER  
Prof. Leticia TARRUELL

April, 2021



The background of the page features a large, light gray watermark of the University of Trento seal. The seal is circular and contains a central eagle with spread wings, a sun in the upper left, and a star at the top. The text "UNIVERSITAS ATHEENSINA STUDIORUM" is written around the perimeter of the seal.

Arturo Farolfi

Spin dynamics in two-component Bose-Einstein  
condensates

PH.D. THESIS IN PHYSICS

UNIVERSITY OF TRENTO  
April, 2021





*Acknowledgements:*

*To my family, for being there for me.*

*To Giulia, for being the fantastic person she is.*

*To my supervisors, for the support and the teaching.*

*To the friends, mountain-dwellers, Folkini and other fellows for making me have fun.*



# Contents

<b>Introduction</b>	<b>1</b>
<b>1 Theoretical background on two-component BECs</b>	<b>5</b>
1.1 Bose-Einstein condensates of weakly interacting gases . . . . .	5
1.1.1 The Gross-Pitaevskii equation . . . . .	5
1.2 BECs mixtures . . . . .	9
1.2.1 Two-component GPE . . . . .	10
1.2.2 Coherently-coupled mixtures . . . . .	15
1.3 Landau-Lifshitz model in two-component BECs . . . . .	17
1.3.1 Josephson equation . . . . .	17
1.3.2 Josephson dynamical regimes . . . . .	19
1.3.3 Landau-Lifshitz equation . . . . .	20
1.3.4 From GPE to LLE . . . . .	21
1.3.5 Josephson model with cold gases . . . . .	24
<b>2 Experimental apparatus and magnetic shield characterization</b>	<b>27</b>
2.1 Magnetic shield characterization . . . . .	28
2.1.1 Review of magnetic shielding principle . . . . .	29
2.1.2 Attenuation measurement . . . . .	32
2.2 Experimental apparatus . . . . .	35
2.2.1 Experimental requirements . . . . .	35
2.2.2 Sources of magnetic noise . . . . .	36
2.2.3 Vacuum chamber . . . . .	36
2.2.4 Support structure . . . . .	37
2.2.5 Magnetic coils . . . . .	39
2.2.6 Antennas and microwave system . . . . .	41
2.2.7 Optical traps . . . . .	44
2.2.8 SRS current source . . . . .	47
2.2.9 Imaging systems . . . . .	47
2.2.10 Laser light source . . . . .	48

2.3	Production of the condensed sample . . . . .	49
2.3.1	Atomic source . . . . .	49
2.3.2	MOT . . . . .	49
2.3.3	Gray Molasses . . . . .	50
2.3.4	Evaporative cooling . . . . .	50
2.4	Measurement of magnetic field stability . . . . .	51
2.4.1	Spectroscopic measurement of magnetic field . . . . .	51
2.4.2	Long term magnetic field stability . . . . .	54
2.4.3	Field inhomogeneities . . . . .	57
2.4.4	Coherence time . . . . .	59
<b>3</b>	<b>Observation of Magnetic Solitons</b>	<b>63</b>
3.1	Theoretical background on Magnetic solitons . . . . .	63
3.1.1	Simulations . . . . .	65
3.2	Full state reconstruction . . . . .	68
3.2.1	Magnetization imaging and MS identification . . . . .	68
3.2.2	Relative phase imaging . . . . .	69
3.2.3	Interferometer calibration . . . . .	71
3.3	Production of MSs by phase-imprinting . . . . .	73
3.3.1	Vectorial optical dipole potential . . . . .	74
3.3.2	Calibration of the phase imprint pulse . . . . .	75
3.4	In trap dynamics . . . . .	80
3.5	Evolution and decay of the MS . . . . .	81
3.5.1	MS width . . . . .	81
3.5.2	MS decay . . . . .	83
3.6	Collisions . . . . .	84
3.6.1	Opposite magnetization collisions . . . . .	84
3.6.2	Same magnetization collisions . . . . .	85
<b>4</b>	<b>Spin quantum torque in magnetic heterostructures in cold gases</b>	<b>89</b>
4.1	Manipulation of an elongated JJ . . . . .	90
4.1.1	Realization of 1D spin dynamics . . . . .	90
4.1.2	Spectroscopic density shift . . . . .	93
4.1.3	Density-dependent ARP . . . . .	95
4.1.4	Plasma oscillations . . . . .	97
4.2	Breaking of magnetic heterostructures . . . . .	99
4.2.1	Analogy with magnetic materials . . . . .	99
4.2.2	Breaking of magnetic interfaces . . . . .	100
4.2.3	Velocity of the wavefront . . . . .	104
4.2.4	Correlation length . . . . .	105
4.2.5	3D system . . . . .	107
	<b>Conclusions</b>	<b>111</b>

# Introduction

Bose-Einstein condensates (BECs) of ultra-cold atoms have been the object of a large research effort, that started a century ago and is now a rich research topic with many active research groups around the world. A deep knowledge of its underlying physics has been acquired, for example on the thermodynamics of the gas, superfluidity, topological excitations and many-body physics. However, many topics are still open for investigation, thanks to the flexibility and the high degree of control of these systems. Shortly after the first realization of Bose-Einstein condensation, also the research on multi-component BECs of alkali atoms begun thanks to the internal structure of the electronic ground state. These internal states can be coherently coupled with an external electromagnetic field and can interact via mutual mean-field interaction, with different behaviours depending on the values of the interaction constants between the states. Multi-component systems of different internal states offer richer dynamics and effects not present in a single-component, such as ground states with different magnetic ordering, density as well as spin dynamics and internal Josephson effects. Of the numerous multi-component systems available, two-component mixtures of  $^{23}\text{Na}$  atoms in the hyperfine states  $|F=1, m_F=\pm 1\rangle$  are of peculiar interest. In fact, the interaction constants of the components are such that the ground state of the mixture has anti-ferromagnetic ordering and the system is perfectly symmetric under the exchange of the two species, differently from the largely studied mixtures of  $^{87}\text{Rb}$  atoms. In this peculiar system, density- and spin-excitations have a very different energetic cost, with the latter being much less energetic, such that they can become completely decoupled from the former. Moreover, spin-excitations, that are connected to excitations in the relative-phase between the components, change drastically their nature when a coherent coupling is added between the states. Since the coupling effectively locks the relative-phase in the bulk, spin excitations become localized in the presence of the coupling. While extensive theoretical predictions on the spin dynamics of this system has been already performed, experimental confirmation was still lacking because of the high sensitivity to external forces (due to the very low energy of the spin excitations) and the difficulty of realizing a low-energy coupling between these states in the presence of environmental magnetic noise.

During the course of my Ph.D., I completed a novel experimental apparatus for the realization of coherently-coupled mixtures of sodium BECs and performed with it the first measurement of scientific relevance. The highly stable and low-noise magnetic environment of this apparatus enables the experimental investigation of a previously inaccessible regime, where the energy of the coupling becomes comparable to the energy of spin excitations of the mixture. With this apparatus, I concluded two experimental investigations: I produced non-dispersive spin-waves in a two-component BEC and investigated their dynamics, and I experimentally observed the quantum spin-torque effect on an elongated bosonic Josephson junction.

The new experimental apparatus features a magnetic environment with strongly improved stability. Magnetic noise is suppressed by five orders of magnitude using a multi-layer magnetic shield made of a high-permeability metal alloy ( $\mu$ -metal), that encases the science chamber. For this apparatus I developed a protocol, compatible with the technical limitations of the magnetic shield, to produce BECs in a spin-insensitive trapping potential. I then characterized the residual magnetic noise using spectroscopic measurements between magnetic-sensitive internal states finding a residual noise compatible with the requirements for observing spin-dynamics effects.

The first experimental result discussed in this Thesis is the production of Magnetic Solitons and the observation of their dynamics in a harmonic trap. Waves in general spread during their propagation in a medium, however this tendency can be counter-balanced by a self-focusing effect if the dispersion of the wave is non-linear, generating non-dispersive and long-lived wave packets commonly named solitons. Solitons have been found in many fields of physics, such as fluid dynamics, plasma physics, non-linear optics and cold-atoms BECs, attracting interest because of their ability to transport information and energy unaltered over long distances, as they are robust against the interaction with inhomogeneities in the medium. Of these systems, cold-atoms can be widely manipulated to generate different kinds of solitons, both in single and in multi-component systems. A new kind of them, named Magnetic Solitons [1], has been predicted in a balanced mixture of BECs of  $^{23}\text{Na}$  in  $|F = 1, m_F = \pm 1\rangle$ , however experimental observation was still lacking. In this Thesis, I present the experimental observation of Magnetic Solitons. I deterministically produced magnetic excitations via phase engineering of the condensate using a spin-sensitive optical potential. I then developed a tomographic imaging technique to semi-concurrently measure the densities of both components and the discontinuities in their relative phase, allowing for the reconstruction of all the relevant quantities of the spinor wavefunction. This allowed us to observe the dispersionless behaviour of the excitations and confirm their solitonic nature. The long-lifetime of these solitons allowed the observation of their dynamics as they perform multiple oscillation in the sample, on a timescale of the order of the second. Moreover, I engineered collisions between different kinds of Magnetic Solitons and observed their robustness to mutual interaction.

The second experimental result presented in this thesis is the observation of the breaking of magnetic heterostructures in BECs due to the quantum torque effect, an effect also found at the interface between magnetic materials. Spins in magnetic materials precess

around the axis of the effective magnetic field, and their dynamics must take into account the external field as well as non-linear magnetization and the magnetic anisotropy of the material. These effects are commonly described by the Landau-Lifshitz equation and have been mainly studied for electronic spins in magnetic heterostructures, where the strong inhomogeneity in the material at the interfaces enhances the exchange effects between spins. For homogeneous materials, this description reduces to the Josephson system, a closely related effect that is more known in cold-atoms systems. The Josephson effect arises when a macroscopic number of interacting bosonic particles is distributed in two quantum states, weakly coupled together, with the average energy of the particles occupying each of the states depending on the occupation number itself. In these conditions, the dynamics of the system depends on the difference in occupation numbers, the relative phase between the states and the self-interaction to tunnelling ratio, giving rise to macroscopic quantum effects such as oscillating AC and DC Josephson currents and self-trapping. While these phenomena have been historically studied in junctions between superconducting systems, they can be also realized with cold-atoms systems, allowing the study of Josephson junctions with finite dimensions and in regimes that are hard to reach for superconducting systems.

On this topic, during my Ph.D. I realized a set of protocols for the manipulation of the internal state of an elongated internal bosonic Josephson junction realized with two-component elongated BECs, allowing for the preparation of the initial states of interest. Leveraging the density inhomogeneity of a trapped BEC, I then realized magnetic heterostructures thanks to the simultaneous presence of self-trapped and oscillating regions in the sample. While the dynamics at short times is correctly described by the Josephson effects, at the interface between the regions the particle nature of the gas creates a strong exchange effect, named the quantum torque, that produces magnetic excitations that spread through the sample and break the local Josephson dynamics. I experimentally studied how the process sets in and triggers the spread of these magnetic excitations, while numerical simulations confirmed the dominant role played by the quantum torque effect.

## Thesis structure

- The first Chapter contains a review of theoretical concepts and existing literature. In particular I introduce the Gross-Pitaevskii equation for two-component Bose-Einstein condensates, both in the presence and in the absence of coherent coupling, and discuss existing experimental and theoretical results in the field. Then, I discuss the connection between coherently-coupled two-components BECs and spins in magnetic systems, together with the origin of the quantum torque effect in atomic systems.
- In the second Chapter I describe the experimental apparatus considering the experimental constraints arising from the physical context we want to address. I illustrate the performance assessment of a multi-layer magnetic shield, the protocol to produce an ultracold sample of atoms inside the said magnetic shield and

the characterization of the magnetic field applied to the sample using spectroscopic measurements.

- In the third Chapter I present the experimental observation of Magnetic Solitons. I discuss the protocol to reconstruct semi-concurrently the relevant components of the condensate's order parameter. The experimental technique to generate deterministically Magnetic Solitons is then described and characterized, together with the technique used to identify the solitons. These techniques allow for the observation of Magnetic Solitons and their dynamics that is then described, discussing also the behaviour of the solitons as they collide with each other.
- The fourth Chapter deals with the experimental investigation of the quantum torque effect in magnetic heterostructures. I illustrate the protocols developed to prepare the ultra-cold atoms sample in a given initial state, in a parameter regime where the coherent coupling is comparable to the energy of the mean-field interaction. I illustrate the peculiar parameters regime that is accessible by the experimental apparatus and the non homogeneous Josephson dynamics that originates in the sample. The magnetic hetero-structures produced using this homogeneous dynamics are presented, and the observation of the breaking of the structure due to quantum torque effect at the interface is reported.
- The last chapter is devoted to conclusions and outlook of this work.



# Chapter 1

## Theoretical background on two-component BECs

Bose-Einstein condensation (BEC) has been predicted one century ago and realized for the first time in weakly-interacting atomic gases 25 years ago, starting a rich research effort to understand its fundamental physics. Today, many research topics are open in this field, such as the case of two-component BECs that is the topic of this thesis.

In this Chapter, I will introduce the Gross-Pitaevskii description of BECs, both for single and for two-component systems, introducing the theoretical description for the remainder of the work.

### 1.1 Bose-Einstein condensates of weakly interacting gases

Bose-Einstein condensation can be briefly described as macroscopic occupation of the ground state of a quantum system that happens when a large number of identical bosonic particles is cooled at very low temperatures. This macroscopic occupation leads to the appearance of a complex *order parameter*, also known as the wavefunction of the condensate, that describes the long-range order between particles sharing the same quantum state. At extremely low temperatures and large density, the condensate fraction dominates over the remaining normal (thermal) component and the physics of the system is well described by a classical complex field.

#### 1.1.1 The Gross-Pitaevskii equation

In the case of atomic gases, the identical particles are single atoms of mass  $m$ , subject to an external confining potential  $V_{ext}(\mathbf{r})$ . At sufficiently low density  $n$ , the atoms can be considered as weakly interacting via elastic 2-body collisions with s-wave scattering length  $a$ . This condition of *diluteness* is expressed by the gas parameter  $na^3 \ll 1$ , and is usually very well fulfilled by ultracold atomic gases, with densities of the order of  $10^{20}$  atoms/m<sup>3</sup> and scattering lengths  $\leq 10$  nm.

The many-body Hamiltonian for identical particles is written in terms of the quantum field operator  $\hat{\Psi}$

$$\hat{H}_0 = \int d\mathbf{r} \left( \frac{\hbar^2}{2m} \nabla \hat{\Psi}^\dagger \nabla \hat{\Psi} \right) + \int d\mathbf{r} V_{ext} \hat{\Psi}^\dagger \hat{\Psi} + \frac{1}{2} \int d\mathbf{r} d\mathbf{r}' \hat{\Psi}^\dagger \hat{\Psi}^\dagger V(\mathbf{r} - \mathbf{r}') \hat{\Psi} \hat{\Psi} \quad (1.1)$$

where  $\hbar$  is the reduced Planck constant and  $V(\mathbf{r} - \mathbf{r}')$  is the two-body interaction potential. The evolution equation of the field operator is then given in the Heisenberg representation as  $i\hbar \frac{\partial}{\partial t} \hat{\Psi} = [\hat{\Psi}, \hat{H}_0]$ .

Due to the macroscopic occupation of the condensate state, we can disregard the quantum fluctuations of  $\hat{\Psi}$  and replace the field operator by a classical complex field  $\Psi = \sqrt{n}e^{-i\phi}$ , where  $n$  is the particle density and  $\phi$  the phase of the condensate. This field, loosely identified with the wavefunction of the condensate, represents a mean-field description of the many-body system known as the Bogoliubov description and is a very good approximation in the limit of large number of condensed particles and low temperature. It satisfies the normalization condition  $\int d^3\mathbf{r} |\Psi(\mathbf{r})|^2 = N$ , where  $N$  is the total particle number in the condensate. In order for the substitution to be correct, however, the two-body interaction potential must be substituted by an effective “soft” potential  $V_{eff}$  with the same low-energy scattering length. The interaction term becomes proportional to  $|\Psi(\mathbf{r})|^2$  through the coupling constant  $g = \int d\mathbf{r} V_{eff} = 4\pi\hbar^2 a/m$ . The evolution equation for the classical field is known as Gross-Pitaevskii equation (GPE) [2, Chap. 5]

$$i\hbar \frac{\partial}{\partial t} \Psi(\mathbf{r}, t) = \left( -\frac{\hbar^2}{2m} \nabla^2 + V_{ext}(\mathbf{r}, t) + g|\Psi(\mathbf{r}, t)|^2 \right) \Psi(\mathbf{r}, t). \quad (1.2)$$

This equation is the main theoretical tool to describe the dynamics of BECs, and typically it is solved numerically.

Typical experiments with ultracold atoms BECs are performed applying a harmonic trapping potential, via optical or magnetic forces, along the three spatial directions  $x$ ,  $y$ ,  $z$

$$V_{ext} = \frac{1}{2}m (\omega_x^2 x^2 + \omega_y^2 y^2 + \omega_z^2 z^2) \quad (1.3)$$

where  $\omega_i$  is the trapping frequency along the direction  $i$ . A typical energy scale for the system is given by the average trapping frequency  $\omega_{ho} = (\omega_x \omega_y \omega_z)^{1/3}$  as well as a typical length scale by the harmonic oscillator length  $a_{ho} = \sqrt{\hbar/m\omega_{ho}}$ .

### Thomas-Fermi limit

A useful limit of Eq. (1.2) is the ground state of the condensate found in the stationary (time-independent) case. By setting the time derivative to 0 and substituting  $\Psi(\mathbf{r}, t) = \Phi(\mathbf{r})e^{-i\mu t/\hbar}$  we obtain a stationary equation to be solved self-consistently for the *chemical potential*  $\mu$  and the ground-state wavefunction  $\Phi(\mathbf{r})$

$$\mu \Phi(\mathbf{r}) = \left( -\frac{\hbar^2}{2m} \nabla^2 + V_{ext}(\mathbf{r}) + g|\Phi(\mathbf{r})|^2 \right) \Phi(\mathbf{r}) \quad (1.4)$$

For large values of the mean-field energy ( $Na/a_{ho} \gg 1$ ), the kinetic energy term in the above equation can be neglected and the ground-state wavefunction of a trapped BEC is determined only by the external potential

$$|\Phi(\mathbf{r})|^2 = n(\mathbf{r}) = \frac{\mu - V_{ext}(\mathbf{r})}{g}. \quad (1.5)$$

This condition is known as Thomas-Fermi limit. In the case of harmonic trapping, the chemical potential depends on atom number and trapping parameters as

$$\mu = \frac{\hbar\omega_{ho}}{2} \left( 15 \frac{Na}{a_{ho}} \right)^{2/5} \quad (1.6)$$

and the density distribution of the condensate has a characteristic inverted-parabola profile, with peak density  $n_0 = \mu/g$ , with spatial dimensions equal to the Thomas-Fermi radii

$$R_i = \sqrt{\frac{2\mu}{m\omega_i}} \quad (1.7)$$

The kinetic energy term becomes instead dominant when the density is inhomogeneous at small length scales. An additional characteristic length scale is the *healing length* of the condensate

$$\xi = \frac{\hbar}{\sqrt{2mgn}}, \quad (1.8)$$

corresponding to the size of a density variation with kinetic energy ( $\sim \hbar^2/2m\xi_s^2$ ) equal to the interaction energy  $gn$ .

### Dispersion relation

The dispersion relation of small-amplitude excitations on the ground state can be obtained linearizing the GPE around equilibrium and, for a homogeneous system, one finds the result [2]

$$(\hbar\omega)^2 = \left( \frac{\hbar^2 k^2}{2m} \right)^2 + \frac{\hbar^2 k^2}{m} gn \quad (1.9)$$

where  $\omega$  and  $k$  are the frequency and wavevector of the plane-wave excitation, respectively. In the  $k \rightarrow 0$  limit, the excitations have a linear dispersion with velocity

$$c = \omega/\kappa = \sqrt{gn/m} \quad (1.10)$$

usually referred as the *sound velocity* in the condensate.

### 1DGPE

Typical ultracold-atoms experiments are performed with cigar-shaped elongated samples, due to the harmonic trap having two of the trapping frequencies much larger than

the third one. Since one of the dimensions of the system is much larger than the others the 3D GPE is often reduced to a single dimension (1DGPE) by decomposition of the condensate wavefunction in a transverse time-invariant component  $\Psi_\rho$  and in a 1D complex function evolving under the 1DGPE.

A common choice to reduce the dimension [2, Chap. 24] is to consider equal trapping frequency  $\omega_\perp$  along the transverse directions and transverse confinement much larger than the chemical potential ( $\hbar\omega_\perp \gg \mu$ ). The transverse component then corresponds to the Gaussian ground state of the transverse harmonic confinement. Integrating out the transverse directions, one gets the rescaled interaction constant  $\tilde{g} = 2\hbar\omega_\perp a$  for the 1DGPE.

In experiments, however, the chemical potential is often larger than the transverse confinement and the condensate retains its 3D nature, while having an essentially one-dimensional geometry. Along the radial directions, the wavefunction becomes dependent on the linear density and the 1DGPE may not be an accurate approximation. This effect can be taken into account to describe excitations larger than the transverse size using a non-polynomial Schrödinger equation [3].

### Solitonic waves

In this Section I anticipate the topic of solitonic waves in BECs, that is object of the experimental measurements of Chap. 3. The dispersion relation Eq. (1.9) is valid as long as the excitations do not change the property of the ground state of the GPE. This assumption, however, does not apply to large amplitude excitations, for which the non-linearity of the GPE cannot be neglected. Considering the condensate as a propagating non-linear medium opens the study of a variety of phenomena in wave propagation [4].

A widely-known phenomenon inherent to non-linear media is represented by non-dispersing waves, known as solitons, where the natural dispersion of the wave is balanced by the non-linearity of the medium. A solitonic solution of the propagation equation has a constant or periodic shape and is localized in a finite region, while non-solitonic waves are dispersive (as each frequency component propagates at a different velocity) and thus spread over time everywhere in the medium. Moreover, a solitonic wave is robust against other perturbations in the medium. These characteristics are more typical of particles than of waves, hence the description of the propagation of solitons can often be given in terms of propagation of particles with an effective mass dependent on the characteristics of the medium.

Solitons are found in very different physical systems, such as water canals, non-linear optics, plasma physics, superfluid He<sup>4</sup> and even gravitation waves [5, 6, 7, 8]. In all these systems, the underlying propagation equation determines the existence and the shape of its solitonic solutions. For example, solitons in non-linear optics are described by the integrable Manakov equations, where single solitons analytical solutions not only exists, but are sufficiently robust that two solitons can cross each-other and emerge unchanged (and analytical two-solitons solutions exist).

In single-component ultracold atomic gases, solitons with positive effective mass exist as density-depletions for repulsive interaction [9, 10, 11] and as density-bumps for

attractive interaction [12, 13]. Density-bumps solitons with repulsive interaction and negative effective mass can be created by engineering the dispersion relations of the BEC [14]. The solitonic solution can be calculated analytically from the 1DGPE, as a solution moving at a constant velocity  $v$  and imposing its localization via appropriate boundary conditions. The resulting soliton has a size comparable to the healing length of the condensate, a density depletion proportional to  $1 - v^2/c^2$  and a finite phase jump from one side to the other of the soliton. In the stationary case  $v = 0$  the density is zero at the center of the soliton and the phase jump is  $\pi$ , while at finite velocity both the depletion and the phase jump are reduced, giving the name dark- and grey-solitons to this kind of solutions. Particular attention must be drawn to the dynamical stability of this solution. While the soliton is stable in a purely one-dimensional system, as is often the case for highly elongated samples, in higher dimensions the soliton is unstable towards fluctuations of the density profile and decays into vortices or vortex rings. These solitonic solutions can be connected to many fields in physics, since the 1DGPE can be recast in the form of the analytically-solvable Korteweg–de Vries equation, assuming weak non-linearities [15].

## 1.2 BECs mixtures

The Gross-Pitaevskii description presented in the previous Section assumes that the quantum system has a single lowest-energy state in which condensation happens. At the same time, in mixtures of different species, simultaneous condensation may happen, creating a *quantum mixture*. Generally, the components of the mixture interact via their mean-field energy, and the ground-state and dynamics of the mixture can heavily depend on the interaction constants of the components. In particular cases, additional effects arise due to spin-changing collisions and coherent coupling between the systems.

The research on quantum mixtures utilized atoms of different atomic component (or isotopes) to create a large variety of mixtures of degenerate gases with different interactions and statistics. For example, mixtures of two bosonic components have been realized using  $^7\text{Li}$ - $^{133}\text{Cs}$  [16],  $^{41}\text{K}$ - $^{87}\text{Rb}$  [17] or  $^{87}\text{Rb}$ - $^{133}\text{Cs}$  [18]. Mixtures of a bosonic and a fermionic component, instead, have been realized with  $^{41}\text{K}$ - $^6\text{Li}$  [19],  $^{23}\text{Na}$ - $^{40}\text{K}$  [20],  $^{40}\text{K}$ - $^{87}\text{Rb}$  [21],  $^6\text{Li}$ - $^{23}\text{Na}$  [22] or  $^6\text{Li}$ - $^7\text{Li}$  [23, 24]. Mixtures of two fermionic components have been realized with  $^6\text{Li}$ - $^{40}\text{K}$  [25, 26]. In all these systems, the populations of each component of the mixture are fixed as no conversion between the components is possible and the interaction between the components happens only through their mean-field.

Another possibility to realize quantum mixtures is to utilize the same atomic species in different internal states. In this case, the components have the same statistics but population interconversion is possible, for example via spin-changing collisions or through coherent coupling. The spin degree of freedom allows for the realization of multi-component order parameter, with characteristics typical of both superfluid and magnetic systems, such as quantum phase coherence, long-range order and symmetry breaking. In alkali and alkali-earth atoms, most mixtures of sub-states of the same hyperfine manifold are long-lived and allow for the study of spinor gases with spin-1/2 [27, 28, 29, 30], spin-1

[31, 32, 33, 34, 35] and spin-2 [36, 37]. These states can be coherently manipulated via optical or radiofrequency fields, making them suitable subjects for experimental investigation of spinor quantum fluids. A review of the large literature available on the subject is [38].

The peculiar case of binary mixtures offers a large variety of systems with different characteristics. In this Section, I will give an introduction to the main characteristics of binary mixtures, for both homogeneous and trapped systems: the stability, miscibility, buoyancy of their ground-states, as well as modifications to collective modes and excitation spectrum.

### 1.2.1 Two-component GPE

The Gross-Pitaevskii description developed for single-component BECs can be readily extended to multi-component mixtures as a series of coupled GPEs, where the  $i$ -th component has order parameter  $\Psi_i(r, t)$ , mass  $m_i$ , and is subject to an external potential  $V_{i,ext}$ . Each component is interacting with itself via mean-field with s-wave scattering length  $a_{ii}$  and with the  $j$ -th component with  $a_{ij}$ . The presence of a density-density interaction between the components generates correlations between the densities  $n_1$  and  $n_2$  of the two components. The static and dynamic properties of the mixture depend on the (relative) values of the interaction constants deriving from these scattering lengths.

For two-component mixtures three interaction constants are necessary: two *intra-component* coupling constants  $g_{11} = 4\pi\hbar^2 a_{11}/m_1$  and  $g_{22} = 4\pi\hbar^2 a_{22}/m_2$ , one *inter-component* coupling constant  $g_{12} = 2\pi\hbar^2 a_{12}/m_r$  with  $1/m_r = 1/m_1 + 1/m_2$ . The coupled GPEs are then:

$$i\hbar \frac{\partial}{\partial t} \Psi_1 = \left( -\frac{\hbar^2}{2m_1} \nabla^2 + V_{1,ext} + g_{11}|\Psi_1|^2 + g_{12}|\Psi_2|^2 \right) \Psi_1 \quad (1.11)$$

$$i\hbar \frac{\partial}{\partial t} \Psi_2 = \left( -\frac{\hbar^2}{2m_2} \nabla^2 + V_{2,ext} + g_{22}|\Psi_2|^2 + g_{12}|\Psi_1|^2 \right) \Psi_2 \quad (1.12)$$

The mixture stability is ensured for positive values of  $g_{11}$  and  $g_{22}$ . In the following we will assume components of equal mass  $m_1 = m_2 = m$ , as this is the case of mixtures of different internal states of the same atomic species.

#### Miscibility condition

For an external uniform potential, the ground-state of the system is a uniform mixture if the coupling constants satisfy the inequality:

$$g_{12} < \sqrt{g_{11}g_{22}} \quad (1.13)$$

In this condition, the distributions of the components maximize their overlap. In the opposite case, a phase-separated configuration is energetically favourable, where the two components occupies different regions and minimize their overlap. This condition sets the *miscibility* of the mixture, namely the tendency of the two components to occupy

the same volume. The dynamic stability against local density fluctuations is ensured by the more stringent condition

$$|g_{12}| < \sqrt{g_{11}g_{22}}. \quad (1.14)$$

When the latter condition is violated and  $g_{12} < 0$ , the system can realize self-bound quantum droplets, that are stabilized by beyond-mean-field effects [39, 30, 40].

### Buoyancy condition

In the presence of an external trapping potential, the miscibility condition does not suffice to guarantee a uniform ground-state of the mixture, as the density distributions  $n_1$  and  $n_2$  of the components depend also on the intra-component coupling constants. With condition Eq. (1.14) satisfied, in the Thomas-Fermi limit Eq. (1.5) can be recast for the two-component system as

$$\mu_1 - V_{1,ext}(r) - g_{11}n_1(r) - g_{12}n_2(r) = 0 \quad (1.15)$$

$$\mu_2 - V_{2,ext}(r) - g_{22}n_2(r) - g_{12}n_1(r) = 0, \quad (1.16)$$

from which one can derive that the two distributions are in general different, except for the special case  $g_{11} = g_{22}$  and  $V_{1,ext} = V_{2,ext}$ . The tendency of the mixture to have unequal spatial distribution is referred with the name of *buoyancy* and can be present also for miscible mixtures. In the case of buoyant mixtures, the system minimizes its energy by localizing the component with smaller intra-component interaction constant in the center of the trap, where the density is higher. The other component “floats” on the first at the edge of the trap, where its density is lower.

Miscibility and buoyancy are well-defined concepts only when the atom number in each component is fixed. In the presence of coherent coupling, as is the case of the next Sections, these concepts will require revisiting.

### Dispersion relation

The dispersion of collective oscillations of a two-component miscible mixture can be obtained similarly as the single-component case. However, “in-phase” and “out-of-phase” oscillations of the two components have different dispersion relations, depending on the intra- and inter-component coupling constants. For  $g_{11} = g_{22}$ , in-phase oscillations correspond to total density ( $d$ ) excitations while out-of-phase oscillations to spin excitations ( $s$ ). The two modes corresponds, respectively, to modulations of the sum  $n_1 + n_2$  or the difference  $n_1 - n_2$  of the densities. While for unequal interaction constants the modes are hybridized, the distinction is useful as they reduce to pure density (or spin) modes in the limit  $g_{11} \rightarrow g_{22}$ . The dispersion relations for Bogoliubov excitations are [41]

$$(\hbar\omega_{d,s})^2 = \left(\frac{\hbar^2 k^2}{2m}\right)^2 + \hbar^2 k^2 c_{d,s}^2 \quad (1.17)$$

where the value of the sound velocity for the excitations in the  $k \rightarrow 0$  limit is

$$c_{d,s}^2 = \frac{g_{11}n_1 + g_{22}n_2 \pm \sqrt{(g_{11}n_1 - g_{22}n_2)^2 + 4n_1n_2g_{12}^2}}{2m}. \quad (1.18)$$

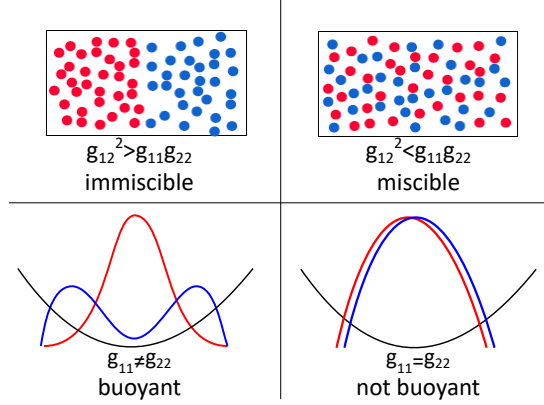


Figure 1.1: Schematic representation of a immiscible mixture with phase-separated components (top left) and a miscible homogeneous mixture (top right) in a box potential. In a harmonic trapping potential is added, a miscible mixture can be buoyant (bottom left) or not buoyant (bottom right).

The  $+$  and  $-$  sign holds for density and spin excitations, respectively. Of particular interest is the case of equal densities  $n_1 = n_2 = n/2$  and symmetric coupling constants  $g_{11} = g_{22} \equiv g$ , as the above equation simplifies into

$$c_s = \sqrt{(g - g_{12})n/2m} \quad (1.19)$$

$$c_d = \sqrt{(g + g_{12})n/2m}. \quad (1.20)$$

They express the *sound velocity*  $c_d$  and *spin-sound velocity*  $c_s$  in the condensate. It should be noted that the values of the two sound velocities can be greatly different, due to the different dependence on the coupling constants. Experimental observation of the two sound velocities for mixtures of  $^{23}\text{Na}$  in  $|1, \pm 1\rangle$  has been reported in [42].

### Spin healing length

Similarly to Eq. (1.8), one can define the *spin-healing length*

$$\xi_s = \frac{\hbar}{\sqrt{2m\delta gn}}, \quad (1.21)$$

by imposing that the kinetic energy of a spin excitation to be equal to  $\delta gn$ . This is the length required for the order parameter to return to its bulk value in the presence of a spin excitation, and so sets the typical size of the excitation. It should be noted how the spin-healing length can be greatly different from the healing length due to its dependence on  $\delta g$ , and even diverges in the limit  $g_{12} \rightarrow g$ .

### In-trap oscillations

Collective oscillations in a harmonically trapped sample are studied within the hydrodynamic formalism as fundamental trap modes. For binary mixtures, the same treatment



must be applied separately for density and spin oscillations. In the case of equal densities and symmetric coupling constants discussed above, the total density modes of the mixture are the same as the single-component case. The spin modes, instead, are softened by the inter-component interaction, as their frequency is lowered by  $\sqrt{(g - g_{12})/g}$  and their sensitivity to external forces enhanced. For example, the spin dipole mode has frequency

$$\omega_{SD} = \sqrt{\frac{g - g_{12}}{g + g_{12}}} \omega_{ho} \quad (1.22)$$

that has been experimentally observed in the case of  $^{23}\text{Na}$  [43]. For immiscible or buoyant mixtures, the inhomogeneity of the ground state prevents the existence of small harmonic oscillations.

### Solitonic waves

In two-component one-dimensional systems a richer variety of solitonic solutions exist thanks to the existence of both density- and spin-modes, and by the possibility of changing the conditions of the system from polarized and unpolarized (respectively, unequal or equal densities at large distance from the soliton). Interestingly, while the density solitons are substantially unchanged, new kinds of solitons exist in the spin channel.

Solitonic solutions can be found analytically in the symmetric case of equal interaction constants (Manakov limit), where the two-component GPE become integrable by the inverse scattering transform method [4, 15]. Many particular solutions exist in this regime, i.e., the dark-bright soliton in a polarized system [44, 45], or the dark-dark soliton in an unpolarized system [46]. In the case of unpolarized system, a rich variety of solitonic solutions are present, such as Gardner and algebraic solitons, breathers and “solibore” solutions [15].

In the case of a miscible mixture with equal intra-component interactions and weak spin channel ( $\delta g \ll g$ ), an analytical solution named *magnetic soliton* exists when the densities are equal [1]. More discussions on magnetic solitons and their experimental observation are reported in Chap. 3.

While the solitonic waves discussed before are one-dimensional objects and not, in general, stable in higher dimensions, different solitonic solutions exist in higher dimensions [47, 48]. In particular for elongated 3D condensates, a large family of vortical structures are admitted in the transverse plane, resembling the vibrational modes of a membrane, known as Chladni modes [49].

Furthermore, solitons exist also in multi-components systems, for example bright-bright-dark solitons in three-components systems [50, 51].

### Experimentally realized binary mixtures

The Gross-Pitaevskii description of a binary mixture just developed is valid for all values of the interaction constants between the components. Since the values of the interaction constants depends on the atomic species and internal states considered, different experimental systems are necessary to realize mixtures with different characteristics.

These experimental systems, however, must take into account several additional practical factors. First, not all combinations of atomic species and internal states form a stable mixture, due to atom losses caused by inelastic collisions. Second, for a given mixture, the coupling constants are fixed by the nature of the components, with the notable exception of mixtures with accessible Feshbach resonances. Third, not all mixtures can be simultaneously trapped, especially when the confining potential is created via a magnetic trap. Due to these limitations only a handful of binary mixtures have been experimentally realized. In the following I present some examples of binary mixtures that are relevant for this thesis.

Binary mixtures of  $^{87}\text{Rb}$  have been firstly realized in the states  $|1, -1\rangle$ - $|2, 1\rangle$  [27, 52] due to the possibility of simultaneous magnetic trapping. In particular, these states have the same Zeeman energy sensitivity at a field of 3.2 G [53], consequently they experience an identical trapping potential to an excellent approximation. The s-wave scattering lengths  $a_{m_F, m'_F}$  of these states are [54]

$$a_{-1, -1} = 100.4a_0 \quad a_{+1, +1} = 95.44(7)a_0 \quad a_{+1, -1} = 98.006(16)a_0. \quad (1.23)$$

Therefore, the mixture they form is immiscible and phase-separates.

A mixture of  $^{87}\text{Rb}$  offering tunable interactions via a Feshbach resonance is  $|1, 1\rangle$ - $|2, -1\rangle$ . Tuning the inter-component interaction, this mixture can be miscible or immiscible [55]. Even in the miscible condition, however, the intra-component interactions between the components are different and the mixture is subject to buoyancy.

The last example is the case of  $^{23}\text{Na}$ . Mixtures of these atom in the two different hyperfine states ( $F = 1$  and  $F = 2$ ) have been found to decay rapidly [56] (with the exception of the states  $|1, \pm 1\rangle$ - $|2, \pm 2\rangle$ ) via hyperfine-relaxation collisions, while all mixtures of states in the  $F = 1$  manifold are stable. In particular, the states  $|1, \pm 1\rangle$  have scattering lengths [57]

$$a_{+1, +1} = a_{-1, -1} = 54.54(20)a_0 \quad a_{+1, -1} = 50.78(40)a_0. \quad (1.24)$$

consequently they form a miscible mixture. Moreover, this mixture is not subject to buoyancy since the intra-component interaction constants are exactly equal. Since the intra- and inter-component coupling constants are similar ( $\delta g \approx 0.07g$ ), the mixture is near the threshold between miscibility and immiscibility. In this condition the spin excitations are less energetic than the corresponding density ones, as their energy is proportional to  $\delta g \ll g$ , and vanishes at the miscible-immiscible transition, when  $\delta g \rightarrow 0$ . A direct effect of this condition is the strongly increased static polarizability of collective spin modes [43]. The energetic difference between the two modes is also evident in the characteristic velocity and size of the excitations. Due to their different dependence on the coupling constants, in fact, the spin-sound velocity is  $\approx 5$  times smaller than the sound velocity and the spin-healing length is also correspondingly  $\approx 5$  times larger than the healing-length. The state  $|1, 0\rangle$  instead is immiscible with any of the  $m_F = \pm 1$  states [31].

### 1.2.2 Coherently-coupled mixtures

The coupled GPEs introduced in the previous Section describe quantum mixtures where no interconversion process between the component takes place, conserving the number of particles in each component. For mixtures of the same atomic species in different internal states, however, the components can be coherently coupled via radiofrequency or optical fields. Therefore, only the total atom number of the system is conserved, as the coupling allows for conversion from one component to the other.

This coherent interconversion process can be inserted in Eqs. (1.11-1.12) giving [2, Chap. 21]:

$$i\hbar \frac{\partial}{\partial t} \Psi_1 = \left( -\frac{\hbar^2}{2m} \nabla^2 + V_{1,ext} + g_{11}|\Psi_1|^2 + g_{12}|\Psi_2|^2 \right) \Psi_1 - \frac{\hbar\Omega(t)}{2} e^{i\omega_{rf}t} \Psi_2 \quad (1.25)$$

$$i\hbar \frac{\partial}{\partial t} \Psi_2 = \left( -\frac{\hbar^2}{2m} \nabla^2 + V_{2,ext} + g_{22}|\Psi_2|^2 + g_{12}|\Psi_1|^2 \right) \Psi_2 - \frac{\hbar\Omega^*(t)}{2} e^{-i\omega_{rf}t} \Psi_1 \quad (1.26)$$

where, in the rotating wave approximation,  $\omega_{rf}$  and  $\Omega$  are, respectively, the frequency and the Rabi frequency of the coupling field. The energy difference between the components has been absorbed into the definition of  $V_{ext}$ . The phase of the coupling is assumed such that  $\Omega$  is real and positive. The frequency of the coupling is set near the resonant condition  $\omega_{rf} = \omega_0 + \delta$  where  $\delta$  is the *detuning* from the resonance and  $\omega_0$  the *transition frequency* between the components ( $V_{2,ext} - V_{1,ext} \equiv \hbar\omega_0$ ). In the case of equal trapping potentials, the transition frequency is simply given by the energy difference between the internal states, for example the hyperfine splitting between Zeeman levels, and by the mean-field energy shift due to the chemical potential. Under this conditions one can experimentally observe the time evolution of the order parameter  $\Psi(t) \sim e^{-i\mu t} \Psi(0)$  [52].

Under a stationary coherent coupling, Eqs. (1.25-1.26) can be recast in the frame rotating with the coupling field, transforming  $\Psi_1 \rightarrow \Psi_1 e^{-i\omega_{rf}t/2}$  and  $\Psi_2 \rightarrow \Psi_2 e^{i\omega_{rf}t/2}$ . In this frame the GPEs become time-independent and equivalent to Eq. (1.11-1.12) with additional terms  $-\frac{\hbar\Omega}{2} \Psi_{1,2}$ . These terms introduce the energy cost:

$$E_{rf} = -\frac{\hbar\Omega}{2} \int d\mathbf{r} (\Psi_1^* \Psi_2 + \Psi_2^* \Psi_1) = -\hbar\Omega \int d\mathbf{r} |\Psi_2| |\Psi_1| \cos(\phi_2 - \phi_1) \quad (1.27)$$

dependent on the phase difference between the order parameters  $\phi_2 - \phi_1$ .

#### Miscibility condition

The coherent coupling introduces modifications to the ground state and elementary excitations of the system, as the two phases  $\phi_{1,2}$ , before independent, are now correlated by the additional energy cost. A detailed discussion of the properties of the system for a homogeneous potential is given in [58] and in the following I will report only their main results. When the external potential felt by the components is the same, the transfer of particles between the components lead to equal chemical potentials  $\mu \equiv \mu_1 = \mu_2$ . The configuration of minimum energy has  $\cos(\phi_2 - \phi_1) = 1$ , hence the phases of the order parameters are locked together.

In the case of symmetric coupling constants  $g_{11} = g_{22} = g$ , the ground state satisfies the condition:

$$\left(g - g_{12} + \frac{\hbar\Omega}{2\sqrt{n_1 n_2}}\right)(n_1 - n_2) = 0 \quad (1.28)$$

admitting the solutions

$$n_1 - n_2 = 0 \quad (1.29)$$

$$n_1 - n_2 = \pm n \sqrt{1 - \left(\frac{\hbar\Omega}{(g - g_{12})n}\right)^2}. \quad (1.30)$$

These two solutions correspond to an unpolarized and polarized ground state, with the first having lower energy if  $g_{12} < g + \hbar\Omega/n$ . This condition is analogous to the miscibility condition Eq. (1.13), with the unpolarized and polarized solution corresponding, respectively, to a miscible and immiscible mixture. The coupling term favours the (unpolarized) miscible condition. In the polarized ground state the particle interconversion is suppressed by non-linear interaction due to the self-trapping of the Josephson effect.

In the case of a miscible mixture, as in  $^{23}\text{Na}$   $|1, \pm 1\rangle$ , the new ground state has equal densities  $n_1 = n_2$  and equal phases  $\phi_2 = \phi_1$  everywhere and for any coupling strength, independent of the shape of the external potential. When the coupling constants differ, instead, the ground state is always polarized in a uniform system.

For an immiscible mixture, the ground state is not trivial as the phase separation (due to immiscibility) and mixing (due to coherent coupling) compete. For experimental investigation of the ground state of a trapped sample in the case of  $^{87}\text{Rb}$  in  $|1, -1\rangle$ - $|2, +1\rangle$ , see [59]. Mixtures of  $^{87}\text{Rb}$  in  $|1, 1\rangle$ - $|2, -1\rangle$  offers tunable interaction constant  $g_{12}$  via Feshbach resonances [60], allowing for the study of Josephson effects at various values of the mean-field interaction.

### Dispersion relations

The excitation spectrum of the coherently coupled system differs from the uncoupled case. For symmetric interaction constants and in the unpolarized ground state, the density excitations, corresponding to excitations in the global phase  $\phi_1 + \phi_2$  are unchanged, while an energy gap appear in the low-momentum dispersion relation of the spin excitations [58]. The gap,

$$\hbar\omega_J = \sqrt{\hbar\Omega[(g - g_{12})n + \hbar\Omega]}, \quad (1.31)$$

corresponds to the Josephson plasma frequency. The appearance of the gap can be interpreted as the predominance of the internal dynamics over the kinetic energy term for long-wavelength spin excitations. A complete Bogoliubov analysis of the coherently-coupled mixture can be found in [61].

### 1.3 Landau-Lifshitz model in two-component BECs

The evolution of a two-level atom in an (classical) oscillating electric field is well described, in the Rotating Wave Approximation, by the Bloch equations. The state of the atom can be represented by a three-dimensional unit vector (the Bloch vector), such that the  $z$ -component of the vector is equal to the difference in occupation probability of the two states. The internal dynamics of the atoms is then described by the precession of the Bloch vector around a coupling vector. In this description, the coupling vector depends only on the Rabi frequency and detuning of the external coupling field.

The above equation also governs the motion of a magnetic moment in a magnetic field. In real magnetic materials, however, many magnetic momenta are present and they influence each other. Similarly, when many atoms evolve coherently together, they will collectively experience state-dependent energy shifts due to their mutual mean-field interaction, and their internal dynamics can be described by the Josephson equations. Furthermore, if the atoms are not fixed in space, the orbital degrees of freedom of the spin must be considered in addition to the internal dynamics. With suitable approximations, the dynamics of the atoms can be described by a non-dissipative Landau-Lifshitz equation (LLE), the equation governing the magnetization in magnetic materials [62, 63].

In this Section, I introduce the Josephson equation and its dynamical regimes, and discuss how the coupled GPEs Eqs.(1.25-1.26) can be reduced to the Landau-Lifshitz equation. This reduction is the foundation of the experimental work of Chap. 4.

#### 1.3.1 Josephson equation

The Josephson equations [64] describe the tunnelling dynamics between two macroscopically-occupied quantum states. Originally developed for thin junctions between superconductors, commonly known as superconducting Josephson junctions (SJJ), the Josephson equation has been discussed for quantum and for semi-classical systems [65, 66]. The field of SJJs has seen great developments in the last years and is now mature, especially towards the realization of quantum computing devices. The Josephson model, however, can be realized with cold gases of bosons (bosonic Josephson junctions, BJJ), allowing for the exploration of dynamical regimes that are not accessible in the SJJ, such as macroscopic quantum self-trapping and  $\pi$ -oscillations. In the following, I recall the dynamical regimes of the Josephson model as they are useful to describe the calibrations performed in Section 4.1.

The Josephson equations for a Bose gas can be expressed in terms of the spin-density  $\mathbf{s} = (s_x, s_y, s_z)$ . The spin-density describes an ensemble of atoms in the same internal state, hence for a Bose gas its modulus equals the total atomic density  $n$ , and  $s_z = n_1 - n_2$  is the *magnetization* of the system. The equation of motion of a spin in a magnetic field is

$$\dot{\mathbf{s}} = \mathbf{H}(\mathbf{s}) \times \mathbf{s}, \quad (1.32)$$

and the physical characteristics of the system are contained in the definition of the

magnetic field  $\mathbf{H}(\mathbf{s})$ . For a single two-level atom, the coupling vector  $\mathbf{H} = (\Omega, 0, -\delta)$  depends only on the Rabi frequency  $\Omega$  and the detuning  $\delta$  of the external driving field.

Let us consider a homogeneous atomic sample with all atoms in the state 1. The mean-field energy shift of each atom, due to the intra-component interaction, is then equal to  $g_{11}n_1$ . In this sample, if one atom is flitted to the state 2, it will interact with the system through the inter-component interaction constant, and experience an energy shift of  $g_{12}n_1$ . Consequently, if the intra- and inter-component coupling energy are different, the energy of each state will depend on the atomic densities  $n_1$  and  $n_2$ , introducing in the system a detuning term proportional to the (relative) population of the states. Due to the nonlinear detuning, the dynamics of the system is now described by the Josephson model. The non-linear detuning depends on the difference between inter- and intra-component coupling constants and is proportional, in the symmetric case of  $g_{11} = g_{22} = g$ , to  $(g - g_{12})/\hbar = \delta g/\hbar$  [2, Chap. 21]. The coupling vector then becomes

$$\mathbf{H}(\mathbf{s}) = (\Omega, 0, -\delta - \frac{\delta g}{\hbar}s_z), \quad (1.33)$$

and the spin Hamiltonian

$$\mathcal{H} = -\frac{\hbar\Omega}{2}s_x + \frac{\hbar\delta}{2}s_z + \frac{\delta g}{4}s_z^2. \quad (1.34)$$

The Josephson equations are commonly written in terms of two conjugate variables: the fractional population imbalance  $Z$  and the relative phase  $\phi$ . The system can be recast to these variables by the simple transformation:

$$Z = \frac{s_z}{|\mathbf{s}|} \quad (1.35)$$

$$\phi = \tan^{-1}(s_y/s_x), \quad (1.36)$$

or, equivalently,

$$\mathbf{s} = n(\sqrt{1 - Z^2} \cos \phi, \sqrt{1 - Z^2} \sin \phi, Z). \quad (1.37)$$

The dynamics then depends on two dimensionless parameters

$$\Delta E = \frac{\delta}{\Omega} \quad (1.38)$$

$$\Lambda = \frac{\delta g |\mathbf{s}|}{\hbar \Omega}. \quad (1.39)$$

In the new variables, the Hamiltonian reduces to the Josephson Hamiltonian

$$\mathcal{H} = \frac{\Lambda}{2}Z^2 - \sqrt{1 - Z^2} \cos \phi + \Delta E Z, \quad (1.40)$$

where the time is expressed in units of the Rabi period  $1/\Omega$ . In terms of the new variables, the dynamical equations (*Josephson equations*) read

$$\dot{Z}(t) = -\sqrt{1 - Z(t)^2} \sin(\phi(t)) \quad (1.41)$$

$$\dot{\phi}(t) = \Delta E + \Lambda Z(t) + \frac{Z(t)}{\sqrt{1 - Z^2(t)}} \cos(\phi(t)). \quad (1.42)$$

The same equations describe the motion of a nonrigid pendulum with tilt angle  $\phi$ , angular momentum  $Z$  and length proportional to  $\sqrt{1 - Z^2}$  [67]. The two dimensionless parameters  $\Delta E$  and  $\Lambda$ , determine the characteristics of the system and its dynamical regimes.

### 1.3.2 Josephson dynamical regimes

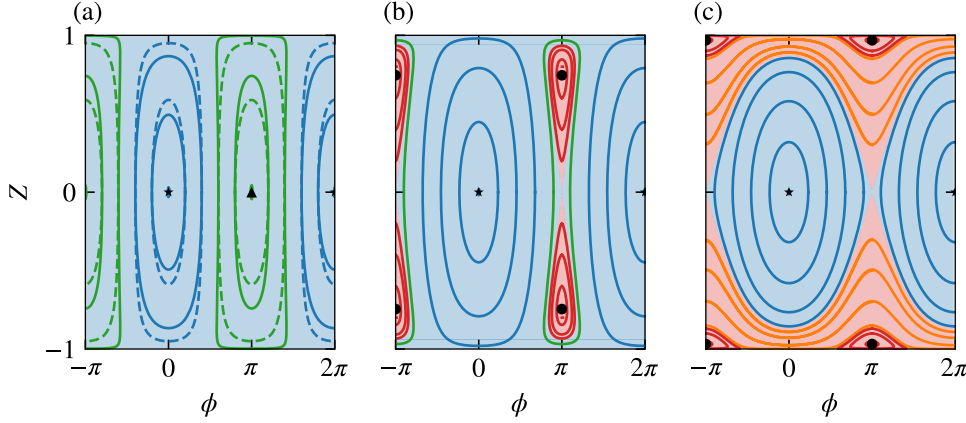


Figure 1.2: Phase portraits of the Josephson equation for different values of  $\Lambda$ . Each line is a trajectory for different initial conditions, while different dynamical regimes are identified by a different background color.

(a) For  $\Lambda < 1$ , the dynamics is Rabi-like, with oscillations with  $\langle \phi \rangle = 0$  (plasma-oscillations, blue) and  $\langle \phi \rangle = \pi$  ( $\pi$ -oscillations, green). All the orbits have  $\langle Z \rangle = 0$ . Two fixed points  $Z = 0$ ,  $\phi = 0, \pi$  exist (star and triangle, respectively). For  $\Lambda \ll 1$ , the system evolves with Rabi dynamics (blue and green dashed lines).

(b) For  $1 < \Lambda < 2$ , two self-trapped regions appear at finite  $Z$  and  $\phi = \pi$ . The self-trapped orbits (red) have  $\langle Z \rangle \neq 0$  and  $\langle \phi \rangle = \pi$ . Plasma and  $\pi$ -oscillations persist outside of the self-trapped region. Three fixed points exist:  $Z = 0$ ,  $\phi = 0$  (star) and  $Z = \pm \sqrt{1 - 1/\Lambda^2}$ ,  $\phi = \pi$  (dot).

(c) For  $\Lambda > 2$ , running-phase self-trapped orbits appear (orange), having  $\langle Z \rangle \neq 0$  and monotonously increasing  $\phi$ .

The Josephson equation has different dynamical regimes depending on the values of the adimensional parameters. For simplicity, I will discuss the dynamical regimes assuming  $\Delta E = 0$ , as the presence of the detuning does not qualitatively affect the phase portrait of the system. For  $\Lambda \ll 1$ , the non-linear effects can be neglected and one recovers the Rabi two-level system, where all the orbits have period  $2\pi/\Omega$  (Fig. 1.2(a), dashed lines) and two fixed points ( $Z = 0$ ,  $\phi = 0, \pi$ ) exist, corresponding to the low- and high-energy eigenstates. Increasing  $\Lambda$ , the non-linear effects modify the orbits (Fig. 1.2(a), solid lines), both in shape and in period. All the orbits, however, retain the peculiar characteristics of the Rabi dynamics: they have mean magnetization  $\langle Z \rangle = 0$  and mean



phase  $\langle\phi\rangle = 0, \pi$ . Orbits near the  $(Z = 0, \phi = 0)$  and  $(Z = 0, \phi = \pi)$  point are known, respectively, as plasma-oscillations and  $\pi$ -oscillations. Their frequency depends on the non-linear interaction parameter as

$$\omega_p = \Omega\sqrt{1+\Lambda} \quad , \quad \omega_\pi = \Omega\sqrt{1-\Lambda}. \quad (1.43)$$

At  $\Lambda = 1$ , a new dynamical regime appears at  $\phi = \pi$ , called of macroscopic quantum self-trapping (Fig. 1.2(b)). In this regime the magnetization never changes sign and oscillates around a finite value, while the phase also oscillates close to  $\pi$ . Two additional equilibrium points  $(Z = \pm\sqrt{1-1/\Lambda^2}, \phi = \pi)$  exist inside the self-trapped region. Plasma and  $\pi$ -oscillations are still present, however  $\pi$ -oscillations are not close to the point  $(Z = 0, \phi = \pi)$ , that is now an unstable point, as they encircle the self-trapped region. Between the two dynamical regions lies a separatrix where the period of the orbits diverges. It should be noted that the condition of existence of the self-trapped region is equivalent to the condition for which the polarized solution of Eq. (1.28) has lower energy than the unpolarized one.

Further increasing the non-linear parameter, the phase portrait changes again for  $\Lambda > 2$ . At this value the self-trapped regions reach the magnetizations  $Z = \pm 1$  and  $\pi$ -oscillations disappear. A new kind of self-trapped orbits (running-phase) are present, where the magnetization still oscillates around a finite value, but the phase is continuously running rather than oscillating.

### 1.3.3 Landau-Lifshitz equation

The evolution of the magnetization  $\mathbf{M}$  in a broad range of ferromagnetic materials can be described as a damped precessional motion around an effective magnetic field, a phenomenon governed by the Landau-Lifshitz equation (LLE) [62, 63]. With the LLE one can describe, for example, the formation of magnetic domains separated by magnetic domain walls and the development of magnetic collective excitations (magnons). Today, frontier research on magnetic materials is investigating the manipulation of spins and spin-carrying currents, a field known as spintronics [68], in a similar fashion as electric charges are manipulated in electronic devices.

The key element of the LLE is the effective magnetic field  $\mathbf{H}$ , that contains the physical characteristics of the ferromagnetic material. This effective field must be calculated considering externally applied fields, the anisotropy of the material, the magnetization state and exchange terms due to the quantum nature of the spins. For a given effective field, the dynamics of  $\mathbf{M}$  is purely precessional, and its modulus remains constant and equal to the saturation magnetization of the ferromagnet, however the effective field can be a non-trivial function of the magnetization. In an extended system, the magnetization is a continuous function of space, allowing for the creation and propagation of spin patterns and spin waves.

For most real materials, however, the precession is damped by a viscous term (Gilbert damping) and  $\mathbf{M}$  aligns with the effective field, therefore stopping the dynamics. This damping is often an unwanted effect that limits the coherence of spintronic devices, and special materials (such as Permalloy) are required to reduce the damping term.



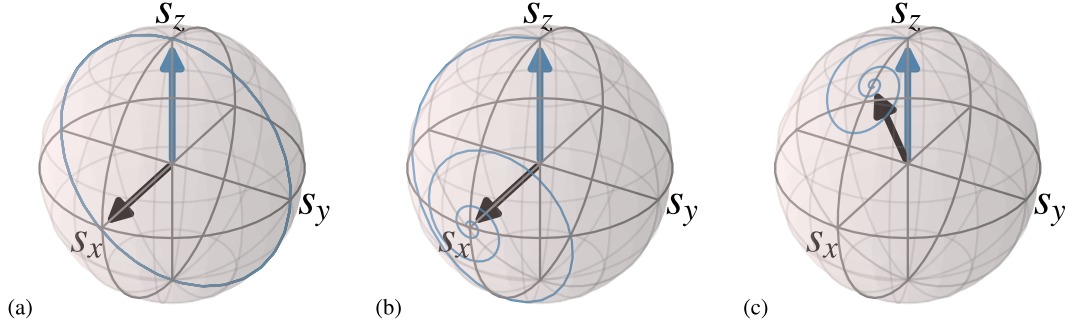


Figure 1.3: Trajectories (blue line) on the Bloch sphere for an initial magnetization  $\mathbf{M}$  (blue arrow) precessing around an effective field  $\mathbf{H}$  (black arrow) under the LLE for different parameters. Undamped (a) and damped (b) motion with constant  $\mathbf{H} = (1, 0, 0)$  along the  $x$ -axis. In the undamped case the motion is periodic, while in the latter the damping term leads to alignment of the magnetization vector to the effective field. (c) Damped motion with  $\mathbf{H} = (0.5, 0, M_z)$ , dependent on the direction of  $\mathbf{M}$ .

In the following, I will outline how a two-component BEC mixture system can model an undamped LLE under suitable approximations. This parallelism is at the basis of the experimental investigation on magnetic heterostructures reported in Chap. 4.

### 1.3.4 From GPE to LLE

The reduction of the two-component Gross-Pitaevskii description to the LLE is based on the separation between the density and the spin dynamics of the gas. Fixing the total density of the gas, the four real numbers constituting the two (complex) order parameters are reduced to the three components of  $\mathbf{M}$ . In the following a two-component one-dimensional system will be considered for simplicity. The same procedure can be applied in a 3D geometry at the expense of more complex vector expressions.

#### Density and spin dynamics

The two-component wavefunction of the condensate is analogous to a spin- $\frac{1}{2}$  and can be simply rewritten as the spinor

$$\Psi = (\psi_1, \psi_2)^T$$

where  $\psi_i = \sqrt{\tilde{n}_i} e^{i\phi_i}$  is the order parameters of the  $i$ -th components. The linear density  $\tilde{n}_i$  (with dimension  $[\text{m}^{-1}]$ ) and the phase  $\phi_i$  describe each component along the only dimension of the system ( $x$ ). From now on,  $\Psi$  indicates a (position-dependent) spinor wavefunction. To separate the density and spin dynamics, we introduce the total linear density  $\tilde{n} = |\psi_1|^2 + |\psi_2|^2$ , and the linear combinations  $\phi_{d,s} = \phi_1 \pm \phi_2$  of the phases. The density matrix  $\Psi^\dagger \otimes \Psi = \{\psi_i^* \psi_j\}_{i,j=1,2}$  of the spinor wavefunction can then be

decomposed for convenience in a scalar and a spin part

$$\Psi^\dagger \otimes \Psi = \frac{1}{2}(\tilde{n}\mathbb{I} + \sigma \cdot \mathbf{s})$$

where  $\sigma$  is the vector of Pauli matrices and  $\mathbf{s}$  is the (linear) spin density. For construction, the modulus of the spin density equals the total density. Each component of the spin density is given by

$$s_\alpha = \Psi^\dagger \sigma_\alpha \Psi.$$

As done in the single-component hydrodynamical formalism, we introduce a scalar current for the total density

$$j_t = -i\frac{\hbar}{2m}\text{Tr}(\Psi^\dagger \partial_x \Psi - \Psi \partial_x \Psi^\dagger) \quad (1.44)$$

and from the total number conservation, we derive the continuity equation for  $\tilde{n}$ :

$$\dot{\tilde{n}} + \partial_x j_t = 0. \quad (1.45)$$

One can express the total density current through the velocity

$$v = \frac{j_t}{\tilde{n}} = \frac{\hbar}{2m} \left( \partial_x \phi_d + \frac{s_z}{\tilde{n}} \partial_x \phi_s \right), \quad (1.46)$$

where we explicitly separated the total and difference phase contributions, respectively induced by density and magnetization excitations. The spin density evolution is also determined by an analogous expression for the spin current  $\mathbf{j}_s$ , where each component is  $\mathbf{j}_{s,\alpha} = i\frac{\hbar}{2m}\partial_x s_\alpha$ . The spin current can be rewritten as

$$\mathbf{j}_s = v\mathbf{s} + \frac{\hbar}{2m\tilde{n}}\partial_x \mathbf{s} \times \mathbf{s} \quad (1.47)$$

where the first term is the spin density transported by the bulk motion (advection) of the condensate and the second one is the *quantum torque* term. The quantum torque term is analogous to the exchange term of magnetic materials, as it originates from the kinetic energy cost of twisting the spin of the condensate. It is a term of pure quantum nature as it vanishes in the limit  $\hbar \rightarrow 0$ .

Differently from the total density, the spin is not conserved due to the action of the effective magnetic field  $\mathbf{H}$  and its continuity equation contains explicitly the precession term

$$\dot{\mathbf{s}} + \partial_x \mathbf{j}_s = \mathbf{H}(\mathbf{s}) \times \mathbf{s}, \quad (1.48)$$

where  $\mathbf{H}(\mathbf{s})$ , defined as function of the one-dimensional quantities, is

$$\mathbf{H}(\mathbf{s}) = (\Omega, 0, -\delta - \kappa s_z). \quad (1.49)$$

We express the nonlinear detuning via the *nonlinear coupling strength*

$$\kappa = (\tilde{g} - \tilde{g}_{12})/\hbar. \quad (1.50)$$

The non-linear coupling strength  $\kappa$  has dimensions  $[\text{ms}^{-1}]$ , so that  $\kappa s_z$  has the dimension of a frequency. It should be noted how the adimensional parameter  $\Lambda$  now becomes

$$\Lambda = \frac{\kappa \tilde{n}}{\Omega} = \frac{\kappa |\mathbf{s}|}{\Omega}. \quad (1.51)$$

### Constant-density approximation

So far, Eq. (1.45) and Eq. (1.48) are equivalent to a pair of coupled 1DGPE, rewritten in terms of the density and spin channels. This formalism however can be simplified in the case of mixtures near the miscible-immiscible phase transition ( $\tilde{g}_{12} \approx \tilde{g}$ ). I recall that, in this condition, the spin excitations have much lower energy than the corresponding density ones and they can be excited essentially without affecting the total density of the system [1, 69, 70]. We can therefore consider the total density of the sample as fixed and set Eq. (1.44) to zero, while the modulus of  $\mathbf{s}$  is now a (position dependent) constant. The dynamics of the system is then described only by Eq. (1.48) and by the definition of  $j_s$  that now contains only the quantum torque term. Eq. (1.48) then becomes

$$\dot{\mathbf{s}} + \partial_x \left( \frac{\hbar}{2m\tilde{n}} \partial_x \mathbf{s} \times \mathbf{s} \right) = \mathbf{H}(\mathbf{s}) \times \mathbf{s}. \quad (1.52)$$

This equation is equivalent to the LLE in the absence of the damping term, so a two-component Bose gas can mimic a dissipationless magnetic material. It should be noted how the quantum-torque effect depends on the gradient of  $\mathbf{s}$  and becomes more important in the presence of sharp spin inhomogeneities. The relevant length scale on which the spin inhomogeneities become important is the spin-healing length of the condensate. In bulk ferromagnetic materials it is often difficult to engineer sharp material inhomogeneities, however magnetic interfaces can be created by placing side-by-side a ferromagnetic and a non-ferromagnetic material [71]. At the interface, the effective field is discontinuous, thus the spin can accumulate a very steep gradient.

In perspective, the Gilbert damping term can be inserted also in Bose gases introducing a thermal component. The mutual interaction between the condensate and the thermal component should lead to alignment of the two spins [72].

### Reduction of an elongated sample to 1D system

In the previous one-dimensional analogy with the LLE we implicitly assumed that the 3D coupled GPEs (1.25 - 1.26) are reduced to one dimension as in Section 1.1.1. This reduction, however, assumes that the radial density distribution of each component is constant, which is true only in the limit  $\hbar\omega_\perp \gg \mu_1, \mu_2$ , i.e. when the radial density distribution is equal to the ground state of the radial harmonic oscillator and the radial size of the sample is smaller than the healing length. This is a challenging condition to realize in experimental systems, due to the very tight radial confinement required.

However, Eq. (1.52) is valid as long as the system is one-dimensional for spin excitations, which is a less strict requirement since spin excitations have size of the order of  $\xi_s > \xi$ . When the radial size of the system  $R_\rho$  satisfies  $\xi < R_\rho < \xi_s$ , the system is effectively one-dimensional for spin excitations, while remaining three dimensional for density ones. In this condition one cannot, in general, assume a fixed radial density profile for both components to calculate the interaction constants. However in Eq. (1.52) the only contribution of the radial density distribution is in the value of the non-linear coupling strength  $\kappa$ , that depends on the total density distribution. In the constant-density

approximation, we can then assume a fixed radial distribution of the total density and calculate the non-linear coupling strength.

In Section 1.1.1, the rescaled coupling constants are derived rewriting the order parameter in cylindrical coordinates as  $\Psi(\mathbf{r}) = \psi(x)\Psi_\rho(\rho)$ . We assume  $|\psi(x)|^2 = \tilde{n}$  is constant, as the  $x$ -dependence of the linear density can be considered separately, applying the local-density approximation along the  $x$  axis. Along the radial directions, the transverse density profile is an inverted parabola (Thomas-Fermi limit) and

$$\Psi_\rho(\rho, \theta) = \sqrt{\frac{2}{\pi R_\rho^2}} \left(1 - \frac{\rho^2}{R_\rho^2}\right)^{1/2}. \quad (1.53)$$

Its Thomas-Fermi radius  $R_\rho = 2\sqrt{\frac{\hbar}{m\omega_\perp}}(a\tilde{n})^{1/4}$ , where  $a = a_{11} = a_{22}$ , depends on the total linear density  $\tilde{n}$ . The rescaled interaction constants then are

$$\tilde{g}_{ij} = \frac{4\pi\hbar^2 a_{ij}}{m} \int |\Psi_\rho|^4 \rho d\rho d\theta = \frac{4\pi\hbar^2 a_{ij}}{m} \frac{4}{3\pi R_\rho^2} = \frac{4}{3}(a\tilde{n})^{-1/2} \hbar\omega_\perp a_{ij} \quad (1.54)$$

and  $\kappa$  can be calculated from Eq. (1.50). From the above equation, however, one can also express the non-linear coupling strength in terms of the 3D coupling constants  $g_{ij}$  and the 3D density on the  $x$  axis of the sample (at  $\rho = 0$ )  $n^{3D}$ , obtaining

$$\kappa\tilde{n} = \frac{2}{3\hbar}(g - g_{12})n^{3D}. \quad (1.55)$$

This result is a consequence of the dependence on  $R_\rho$  of the 1D coupling constant ( $\approx 1/R_\rho^2$ ) and of the linear density ( $n = \pi/2R_\rho^2 n^{3D}$ ). In this formulation it is evident how the non-linear coupling strength has a Thomas-Fermi profile for an elongated sample with harmonic trapping along the axis.

### 1.3.5 Josephson model with cold gases

The discussion so far has been focussed on the realization of the Josephson model by coherently coupling different hyperfine states. The principal advantage of bosonic over superconducting Josephson systems is the ability to produce large population imbalances with ease and, when the coherent coupling between the states is provided by radiofrequency fields, by the large amount of control that is possible on the coupling field. In the two-mode approximation it was first experimentally realized [60] using mixtures of  $^{87}\text{Rb}$  in  $|1, 1\rangle$ - $|2, -1\rangle$ , thanks to the tunable inter-species interaction constant, where all the Josephson dynamical regimes have been observed. Using the same mixture but in an elongated system, the mixture miscibility can be controlled with the coherent coupling strength. Both the ground state at the crossover and the dynamics following a quench between the miscible and immiscible regimes have been studied [59, 73].

The Josephson model can be also realized in cold gases by spatially separated condensates, i.e. a single Josephson junction has been realized in a double-well trap [74, 75, 76], in addition realization of 1D array of junctions [77] and elongated systems [78, 79,

[80] have also been reported. In this system, the condensates are spatially separated in the two wells and, by bringing the wells close one to the other, their wavefunctions are slightly overlapped. The overlap is sufficiently small that the wavefunctions of the condensates are not modified, and a linear tunnelling between the wells is established. The dimensionless parameters can then be computed from the overlaps of the wavefunctions [81], assuming that these are independent of  $Z(t)$ . By tuning the barrier height between the wells different dynamical regimes can be accessed, in particular it is possible to engineer very high values of  $\Lambda$  by increasing the barrier. Moreover, systems with negative values of  $\Lambda$  can be realized if the interaction between the atoms is attractive [76]. On the other side, for low barrier heights (low  $\Lambda$ ), the two-mode approximation starts to break down in these systems, hence not all the parameters regimes can be easily explored. An experimental analogous to the (dissipative) LLE with spatially separated condensates has been recently reported in [79, 82].



# Chapter 2

## Experimental apparatus and magnetic shield characterization

### Motivation for new experimental apparatus

As described in Chap. 1, it is possible to realize a multi-component coherently-coupled quantum mixture using atoms in different hyperfine states. The time-independent coupled GPEs description of Eq.s 1.25-1.26 has been derived assuming constant values of the coupling field strength  $\Omega$  and detuning  $\delta$ . This assumption, however, is always an approximation for experimental systems, where both these parameters can be influenced by uncontrollable factors. The experimental realization of coherently coupled mixtures of the states  $|1, \pm 1\rangle$  of  $^{23}\text{Na}$  and the investigation of spin dynamics, in particular, pose some stringent requirements to the experimental apparatus, particularly to the stability of the magnetic field and its homogeneity across the sample.

In  $^{23}\text{Na}$  atoms, as in all alkali atoms, the splitting in hyperfine states originates from the coupling between the total nuclear angular momentum and the total electron angular momentum. I recall, for notation purposes, that the quantum numbers of interest to describe the hyperfine levels at low magnetic fields are the total atomic angular momentum ( $\mathbf{F}$ ) and its projection along the quantization axis ( $m_F$ , the magnetic quantum number). The ground state  $3^2S_{1/2}$  of  $^{23}\text{Na}$  is then split in two manifolds ( $\mathbf{F} = 1, 2$ ). Each manifold is composed of energy-degenerate substates with different  $m_F$ , whose degeneracy is lifted in the presence of an external magnetic field  $B_z$  due to Zeeman effect. The energy of each states can be calculated from the well known Breit-Rabi formula [83] and, in the limit of small  $B_z$ , the energy shift of the state  $|F, m_F\rangle$  is linear in the magnetic field as

$$\Delta E_{|F, m_F\rangle} = \mu_B g_F m_F B_z \approx g_F m_F \times h 0.711 \text{ MHz/G} \times B_z, \quad (2.1)$$

where  $\mu_B$  is the Bohr magneton,  $g_F$  the Landé g-factor and  $h$  the Planck constant. For the states  $|1, \pm 1\rangle$  this energy difference is of the order of 1.4 MHz/G. To apply a coherent coupling with a known detuning, then, the frequency of the coupling field must closely

match the energetic difference due to the Zeeman effect, with this condition being more strict for lower  $\Omega$ , since the relevant parameter is the ratio  $\delta/\Omega$ .

The investigations we aim to perform with this experimental apparatus are in the Josephson regimes, therefore the strength of the coherent coupling must be comparable with the Josephson energy of the sample  $(g - g_{12})n$  (Section 1.3). For a typical BEC of  $^{23}\text{Na}$ , the condensate has density of about  $10^{20}$  atoms/m<sup>3</sup>, leading to a mean-field energy of  $(g - g_{12})n \approx h100$  Hz. Given the sensitivity of the energy of states to the magnetic field, the values of the latter should fluctuate much less than 100  $\mu\text{G}$ .

### Structure of the Chapter

As part of my PhD work I developed a new experimental apparatus to realize coherently-coupled BECs of sodium in a very low noise magnetic environment. This new apparatus stems from the previous works of our laboratory of designing a multi-layer magnetic shield [84] and realizing a BEC of  $^{23}\text{Na}$  in a hybrid trap [85].

In this Chapter I present the characterization of the realized magnetic shield, as well as the design, realization and characterization of a new experimental apparatus that allows to produce a coherently-coupled Bose-condensed sample in a uniform magnetic field with fluctuations less than 10  $\mu\text{G}$ . In the first Section, I characterize the passive magnetic shield prior to installation. In the second Section, I review the design choices and give a technical description of the apparatus in its current status. In the third Section, I report the measurements of the resulting properties of the magnetic field.

## 2.1 Magnetic shield characterization

Magnetic noise in a laboratory environment is usually on the order of a few mG in a wide spectrum of frequencies from DC to hundreds of kHz. This noise is usually not problematic for BEC experiments using magnetic traps, since it does not interfere with radiofrequency-induced evaporative cooling. In our laboratory, for example, we observed magnetic field fluctuations of several mG, mainly from electric line noise and moving magnetized objects. When higher magnetic field stability is required, a magnetic field stabilization system must be realized.

Magnetic field stabilization has been used in a variety of experiments with cold atoms, such as cold-atom lasers [86], cold-atom experiments in microgravity [87, 88], atom interferometry [89] and atomic magnetometers [90]. Outside the cold-atom community, elimination of stray magnetic fields is desired, for example, in electron microscopy [91], nuclear magnetic resonance [92] and precision magnetometry [93]. These experiments adopted either active cancellation or passive shielding to suppress environmental magnetic noise.

Active stabilization of the magnetic field consists in placing a magnetometer inside the region where the field stability is required, and enclosing the region with electromagnets. The current in the electromagnets is then controlled by a negative-feedback loop to stabilize the reading of the magnetometer. Commercial solutions [94] report a reduction



of external noise by a factor of 100, but the performance of these systems diminishes with distance from the magnetic sensor. Since the vacuum apparatus of an ultra-cold atoms experiment makes it impossible to place the magnetic sensor at the position of the sample, carefully constructed apparatuses using multiple sensors are necessary [95] to reach good performances. Moreover, canceling also magnetic field gradients requires multiple sensors and complicated electronic controls [96].

Passive magnetic shielding, instead, does not require any active stabilization mechanism. The external magnetic noise is suppressed by enclosing the region of interest by high-magnetic-permeability or high-conductivity materials [97]. The former are based on field-shunting effects and are effective on low-frequency (DC-100 Hz) fields, while the latter uses Eddy currents to cancel high-frequency fields (1 kHz and above). Passive shielding has the advantage of canceling fields inside large volumes without any sensor or control electronics required, and for this reason “Zero-Gauss chambers” made of very-high-magnetic permeability materials are often used, reaching attenuation factors of  $\approx 100$  for a single layer, fully closed chamber. This shields however can not have arbitrarily large size because the magnetic field inside the shielding material grows with the enclosed volume and can become too high for the material to sustain.

Apparatuses for ultra-cold atom experiment are usually too large to be enclosed fully in a magnetic shield, however it is possible to surround only the sample, leaving openings in the shield for optical access. While openings degrade the performances of the shield, it is still possible to reach high shielding factors using multiple-layer shields [87]. As a final remark, hybrid systems where active magnetic field cancellation and passive shielding are used in combination have been recently reported [98].

### 2.1.1 Review of magnetic shielding principle

To suppress the magnetic field fluctuations in our laboratory and reach a magnetic field stability of the order of a  $\mu\text{G}$ , a multi-layer magnetic shield was designed [84] and numerically simulated using COMSOL [99].

Passive magnetic shielding relies on the flux-shunting effect of high-magnetic permeability materials. From the Maxwell equations, in a linear and isotropic material, the magnetic field  $\vec{H}$  and the flux density  $\vec{B}$  are related by

$$\vec{B}(\vec{r}, t) = \mu_r \mu_0 \vec{H}(\vec{r}, t)$$

where  $\mu_r$  and  $\mu_0$  are the relative and vacuum magnetic permeability. In the absence of currents, the tangential component of  $\vec{H}$  and the normal component of  $\vec{B}$  are continuous across discontinuities of  $\mu_r$ , hence the magnetic field lines can change direction abruptly at the interface between different materials. Very high-magnetic-permeability alloys have  $\mu_r \approx 10^5$  and at their interface with materials of low  $\mu_r$ , such as air, they distort the magnetic field lines significantly. On the air side, the lines are nearly perpendicular to the interface, while they are nearly tangential inside the material to satisfy the continuity of the normal component of  $\vec{B}$ . Thanks to this effect it is possible to create a nearly field-free region by enclosing it with a layer of high-magnetic-permeability material (shield),

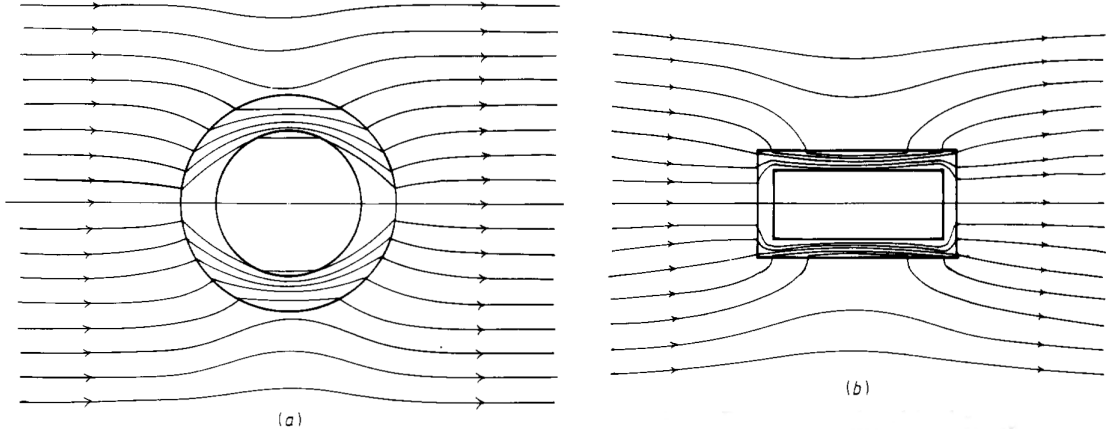


Figure 2.1: Magnetic field lines around a cylindrical magnetic shield, for an external transverse (a) and axial (b) field. The magnetic shield distorts the field lines concentrating them inside the high-permeability material and leading to a lower field in the region inside the shield. Adapted from [97]

since the magnetic field lines will be deviated inside the material and can not penetrate in the enclosed region (see Fig. 2.1).

Since the materials with very high magnetic permeability are all ferromagnetic, two other important characteristics of the material must be taken into account: saturation and residual magnetization. For a ferromagnetic material a more realistic description of the flux density is given by

$$\vec{B} = \mu_0 \mu_r(H) \left( \vec{H} + \mu_0 \vec{M} \right)$$

where the relative magnetic permeability is now dependent on the modulus of the magnetic field  $H$  and the residual magnetization  $\vec{M}$  is the magnetic field that remains in the material when the external field is zero. Generally,  $\mu_r$  has a constant value for low magnetic fields, well below the saturation field. When the saturation is reached, roughly speaking when all the magnetic domains are already aligned with the magnetic field, the value of  $\mu_r$  decreases approaching 1 and the shielding effect is reduced. The magnetization, instead, causes hysteresis in the response curve of the material and depends on the history of the applied magnetic field. The remnant field caused by magnetization effectively introduces an unwanted field that can fluctuate due to changes in the external magnetic field or temperature. Considered this, for the purpose of magnetic shielding, the saturation threshold should be as high as possible to have the maximum attenuation at any magnetic field and the magnetization should be as low as possible to reduce the remnant field inside the shield. Special metal alloys have been developed specifically for these characteristics.

The optimal geometry for a magnetic shield is spherical or an infinitely long cylinder, since any discontinuity in the material can lead to magnetic field leakages. However,

fabricating these shapes is impractical since the material usually is in the form of sheets, and also the shield must be built so that it is possible to assemble it. Hence the most practical shape in our case is a long cylinder, to be assembled around the existing vacuum apparatus. The attenuation of a field directed perpendicularly to the axis of a (thin and long) cylindrical magnetic shield are approximated by the formula [97]

$$A = \frac{\mu_r t}{2R}, \quad (2.2)$$

where  $t$  is the thickness of the cylinder and  $R$  its radius. A similar formula, where the length of the cylinder is used instead of the radius, holds for fields directed along the axis of the cylinder. The shielding performances can be increased using several layers of magnetic shielding, so that the environmental field is more and more attenuated as the layers are traversed. However, the total attenuation factor  $A_{tot}$  is not the product of the different attenuation factors  $A_i$ , as each layer is modifying the shielding performances of the nearby layers. A modified formulas must instead be used [97]

$$A_{tot} = A_n \prod_{i=1}^{n-1} A_i \left[ 1 - \frac{R_i^2}{R_{i+1}^2} \right],$$

where the index  $i$  relates to the  $i$ -th layer of the magnetic shield. A similar formula with weights  $(1 - \frac{L_i}{L_{i+1}})$  holds for axial fields.

These formulas are a useful starting point to grasp the order of magnitude of the performance of a magnetic shield, but do not capture the effect of the finite length of the cylinder and of apertures. To capture this, the magnetic shield has been simulated using the finite elements method (FEM) in COMSOL, to find the optimal geometry for our application and given our geometric constraints. The detailed description of this work can be found in [84] and here only the final results are presented.

Two different materials were chosen for the realization of the magnetic shield, in order to maximize the shielding performances while allowing to apply magnetic fields to the sample safely. The most common material for magnetic shielding is  $\mu$ -metal, an alloy with  $\mu_r = 4.7 \cdot 10^5$  and saturation at 0.75 T [100]. This material permits to reach high shielding efficiencies and has been used for the three outer layers of the shield. However, numerical simulations showed that the magnetic field in the innermost layer would have reached values close to the saturation of  $\mu$ -metal during the MOT phase. To operate the shield in safe conditions, the innermost layer was fabricated out of Supra-50, a different alloy with lower  $\mu_r$  ( $2 \cdot 10^5$ ) but higher saturation (1.5 T [100]). In this way, most of the applied fields are contained in the innermost layer and do not affect the outer layers. It must be noted that the magnetic permeability quoted by manufacturers are obtained for materials in ideal annealing and magnetization conditions, while for real-use scenarios the presence of magnetic hysteresis can lower the permeability even by an order of magnitude [97].

In its final realization the magnetic shield consists of four layers of shielding material. Each layer is composed of two half-cylinders cut perpendicularly to their axis, with the outer diameter of the top half equal to the inner diameter of the bottom one, so that the

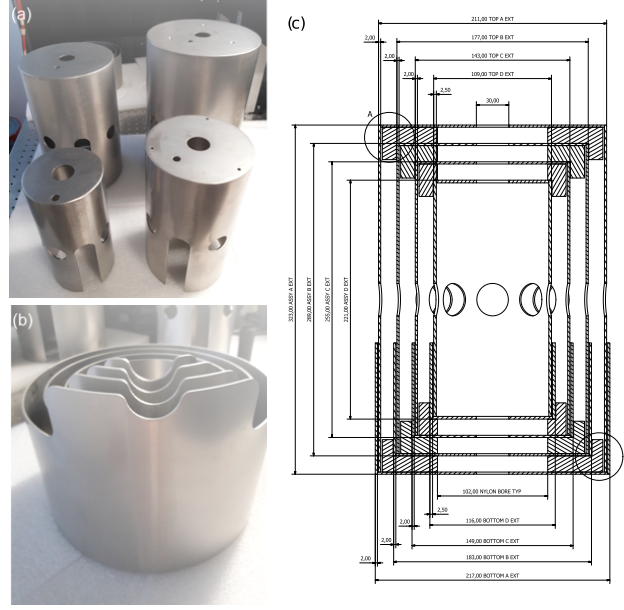


Figure 2.2: The finished four-layer magnetic shield. (a) The four upper pieces disassembled, (b) the four lower pieces assembled and (c) technical drawing of the shield with dimensions in mm.

two pieces can overlap. This overlap between the pieces is necessary to avoid magnetic field leakages. The innermost layer has an internal diameter of 102 mm, height of 221 mm and thickness of 2.5 mm. The outer layers are increased in diameter and in height by 34 mm, have a thickness of 2 mm and are made of  $\mu$ -metal. In each layer there are ten apertures with a diameter of 30 mm to allow optical access. Eight apertures are on the side of the layer, aligned on the central horizontal plane and two apertures are centered on the opposite faces of the cylinder. These apertures are large enough to accommodate standard 25 mm optics and their mountings. Two additional apertures with diameter of 10 mm are placed on the faces of the cylinder to allow for cable access.

The pieces of the shield are held in place by non-magnetic Nylon spacers. A technical drawing and photos of the realized magnetic shield are in Fig. 2.1.1.

### 2.1.2 Attenuation measurement

Before assembling of the magnetic shield on the experimental apparatus, we tested its performance with a direct measurement. This test was performed applying an external uniform magnetic field  $B_0$ , in which the shield was placed, and measuring the magnetic field  $B$  penetrating inside the shield with a magnetometer.

To generate controllable and rather uniform fields, a solenoid made of 0.8 mm copper wire was wound around a hollow, non-magnetic cardboard support. The solenoid has a rectangular cross section of 59 cm  $\times$  39 cm and is 1.5 m long. It is made of 138 windings of wire, at a mean distance of 10 mm, producing at its center a field of 1.18 G/A.

The inhomogeneity of the field inside the solenoid is below 6% in the central region of its volume and this region is large enough to completely enclose the shield. We placed the solenoid away from ferromagnetic materials during the measurement, to avoid distortions of the field. We apply a DC current of 0.5 A and, reversing its polarity, we perform differential measurements in order to subtract the contribution of environmental magnetic fields.

Measurements of magnetic field were performed using a 3-axis magnetic field sensor (Mag-13MCL100) from Bartington Instruments [101]. This sensor has a measuring range of 1 G and is sufficiently low-noise ( $<60 \text{ nG}/\sqrt{\text{Hz}}$ ) that the uncertainty in our measurement is limited by the readout of the sensor's output voltage. Each of the three components of the magnetic field measured by the sensor have independent outputs, that were measured using multi-meters. From the independent measurements of the three axis we compute the modulus of the magnetic field as it is the quantity of interest. We sampled  $|B|$  at different position inside the shield along the  $x$  and  $z$  axis.

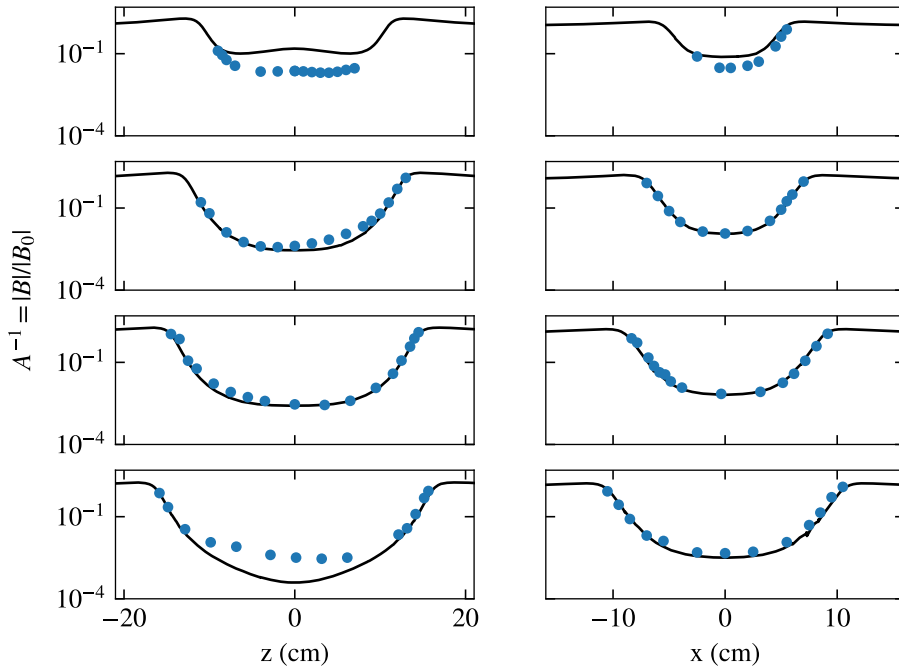


Figure 2.3: Field attenuation by each shield layer in the  $z$  axis and in the  $x$  axis. The experimental data (points) and the numerical simulation (line) show a reasonable agreement. The innermost layer is at the top, the outermost at the bottom.

For each layer of the shield, we measured  $|B|$  for an external field along the axis of the shield ( $z$  axis) and perpendicular to it ( $x$  axis) (Fig. 2.1.2) by placing the shield in the appropriate directions. However, the attenuation of fields along the  $z$  axis is of greater interest, since these will sum linearly to the bias field applied in the experiment, while radial fields will sum in quadrature to the vertical bias. We then compute the

attenuation factor  $A_{meas} = \frac{|B_0|}{|B|}$  to make a comparison with the analytical formula Eq. (2.2) ( $A_{theo}$ ) and the results of numerical simulations ( $A_{numerical}$ ). For large shields with small apertures, a reasonable agreement with the analytical formula is expected, however the history of the material can degrade the magnetic permeability even by an order of magnitude [97]. We measured the attenuation of an external field directed along  $x$  for each layer of the shield separately and calculated the attenuation factor for a conservative value of  $\mu_r$  of 1/10 of the manufacturer's value. From the results of Table 2.1.2 one can clearly see the large effect that the openings and the permeability degradation have on the performances of the shield. However, the numerical simulations are closer to the actual performance and we can *a posteriori* justify the choice made in [84] of using a much lower  $\mu_r$  than the value quoted by the manufacturer. This characterization confirms that running FEM simulations of this kind of apparatuses is a necessity during the design phase.

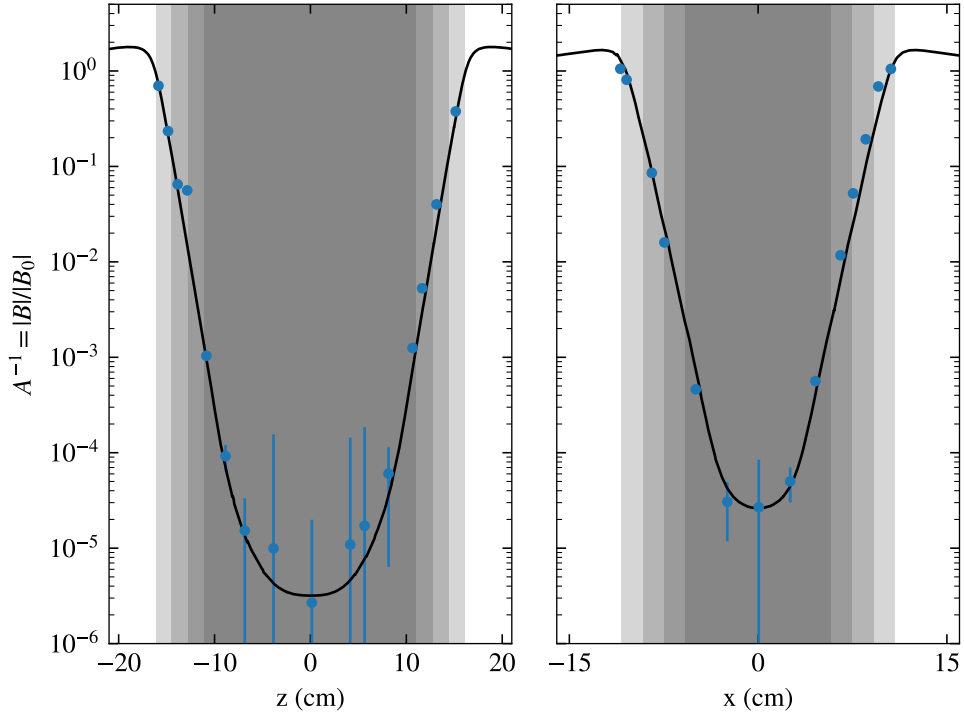


Figure 2.4: Attenuation factor of the assembled magnetic shield for an external field  $B_0$  directed along the  $z$  axis. The experimental measurements (points) and the numerical simulations (line) are in good agreement. The gray shades represent the four layers of the shield. Note that the attenuation right outside of the shield is larger than 1 because the external field is concentrated by the shield itself.

Finally, we characterize the complete shield assembly for a field directed along both axes. The results are reported in Fig. 2.4. We found a good agreement between the

Layer	$A_{meas}$	$A_{theo}$	$A_{numerical}$
1	33	431	13
2	85	630	87
3	141	514	153
4	215	433	316

Table 2.1: Measured versus calculated radial attenuation factors of the separate shield layers. The layers are numbered from the innermost to the outermost.

measured attenuation factor and the numerical simulations of [84], with an attenuation of the external field by five orders of magnitude. While the precise determination of the complete attenuation factor is impossible because of the limited sensitivity of our magnetometer, we can infer from the agreement between the single-layer performances and simulations that the expected performance will be reached by the complete assembly. During this calibration, a small residual magnetization of the innermost layer ( $<0.5$  mG at the center) was found. This magnetization was probably caused during transport or manipulation.

## 2.2 Experimental apparatus

At the beginning of my work the magnetic shield described in the previous Section was not installed in our laboratory, and BEC samples were produced using a preliminary experimental apparatus [85]. The apparatus however was not compatible with the magnetic shield, hence part of it was dismantled, redesigned and then realized. In this Section I describe the current status of the apparatus with the magnetic shield installed.

### 2.2.1 Experimental requirements

During the design process of the new apparatus I considered some key requirements, derived from the protocol developed in our laboratory to produce the BEC sample in a Hybrid Trap [85].

First, optical access with 589 nm laser beams to the sample, along three orthogonal directions, is necessary during the Magneto-Optical Trap (MOT) and the GrayMolasses phases. Additional optical access for Optical-Dipole Traps (ODT) at 1064 nm is required along two horizontal directions. For all beams, a diameter of 1" must be assumed. Optical access along the vertical direction must allow imaging of the sample with resolution of the order of a  $\mu\text{m}$ , in order to observe the features of interest, that have a size of the order of the spin-healing length.

Second, the production of the ultra-cold sample requires magnetic gradients of order 20 G/cm in the MOT and Hybrid Trap phases [102]. Further high-field conditions are expected for magnetic levitation of the sample. The magnetic shield and the MOT coils installed in the apparatus must be such that the shielding material is not permanently magnetized by the application of this field. Application of compensation fields ( $< 1$  G)

and gradients ( $< 1 \text{ G cm}^{-1}$ ) is also required. Moreover, a very stable magnetic field of the order of 100 mG is required to set the quantization axis and lift the degeneracy of the Zeeman sub-levels of the atoms. The stability of the field must permit coherent couplings with Rabi frequencies of the order of a Hz. This stability concerns both external magnetic noise and the stability of the bias field applied to the sample. This field must be stable both in the long timescale, namely the several hours that are usually required to perform an experimental run, and in the short timescale of the dynamics of the sample.

Third, realizing stable mixtures of atoms in different Zeeman sub-levels require a state-independent potential. This can be realized using Optical-Dipole Traps operated at detunings much greater than the fine splitting of  $^{23}\text{Na}$  atoms.

Fourth, a system to manipulate the internal state of the sample is required. Using radiofrequency or microwave fields, the transitions between Zeeman sublevels can be used to realize the coherent coupling between states, or imaging procedures of the sample. This system must have sufficient power and flexibility to realize sufficient coupling strengths and short field pulses.

### 2.2.2 Sources of magnetic noise

During the construction of the experimental apparatus, great care was taken to reduce environmental magnetic field noise as much as possible. Common sources of magnetic noise are magnetized objects and electric equipment.

Magnetized objects produce very low frequency magnetic noise because of temperature fluctuations or position changes. Local fluctuations of Earth's magnetic field are also present at very low frequencies. To reduce nearby magnetized objects, the whole experimental setup is built from non-magnetic materials (mainly austenitic A4 Type-316 steel and aluminium), at least on the optical table of the vacuum apparatus. The main sources of external magnetic fields on our apparatus are the vacuum pumps (NEX Torr D500-5 and D200-5), that contain strong permanent magnets for the ionic pump stage, however they have been equipped with  $\mu$ -metal shielding to suppress such a field outside it. We do not expect such fields to be a problem since they are non-moving with respect to the apparatus.

Electronics equipments in the laboratory produce disturbances from tens of Hertz (main frequency) to hundreds of kHz (e.g. switching power supplies). We chose to minimize noise from switching power supplies by placing them in a nearby room. To reject line noise at 50 Hz, the experimental sequence is phase-locked to the line, using a Schmitt-trigger circuit to produce a TTL signal with fixed phase from the line and then synchronizing the control electronics to this signal.

### 2.2.3 Vacuum chamber

The existing vacuum apparatus in our laboratory was not modified (see [85]) and consists of two chambers composed of stainless steel tubes. The first chamber (*HV*) acts as atomic source and during operation contains hot thermal atoms, while the second



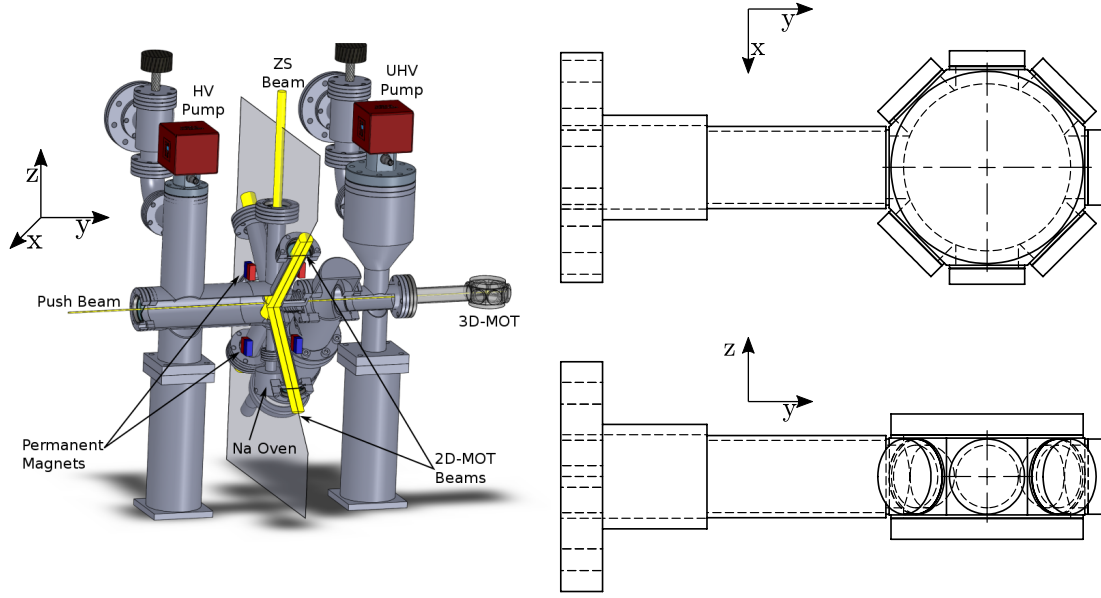


Figure 2.5: (left) Rendering of the vacuum apparatus. Laser beams for the HV chamber are shown as yellow rods. (right) Technical drawing of the octagonal quartz cell. The Cartesian axes represents the reference frame used thorough this thesis.

chamber (*UHV*) is used to prepare and experiment with the ultracold-atom sample. The HV chamber hosts an heated oven to evaporate  $^{23}\text{Na}$  atoms from liquid sodium and a combined non-evaporable getter and ion-pump (NEXTTorr D200-5) to keep the pressure inside the chamber below  $2 \cdot 10^{-10}$  mbar during operation. Glass windows with anti-reflection coating for 589 nm allow optical access and a gate-valve isolates the chamber from the environment. A differential pumping channels connects this chamber to the UHV chamber.

The UHV chamber is composed of a two gate-valves (one between the HV chamber and one to open to the environment), a combined vacuum pump (NEXTTorr D500-5) and an octagonal quartz cell (*science chamber*), at the center of which the cold-atom sample is prepared. A 65 mm long glass tube connects the cell to the rest of the chamber. Ample optical access to the sample in the cell is permitted by two 50.8 mm windows along the vertical directions and by seven 22.9 mm windows on the horizontal plane. All the surfaces of the windows are treated with a Random-Anti-Reflection coating, a nano-textured treatment that reduces reflections below 0.3% for all wavelengths between 1064 and 532 nm.

#### 2.2.4 Support structure

A support structure is required around the science chamber to hold magnetic coils, antennas and imaging lenses. All together, this elements fulfil some key requirements. First, the apparatus is fully contained in the magnetic shield. Second, a completely

non-magnetic structure is used inside the shield to reduce the magnetic hysteresis of the apparatus. Finally, the apparatus permits the assembly and disassembly of the shield with minimal disruptions and is enough future-proof to minimize the need for modifications.

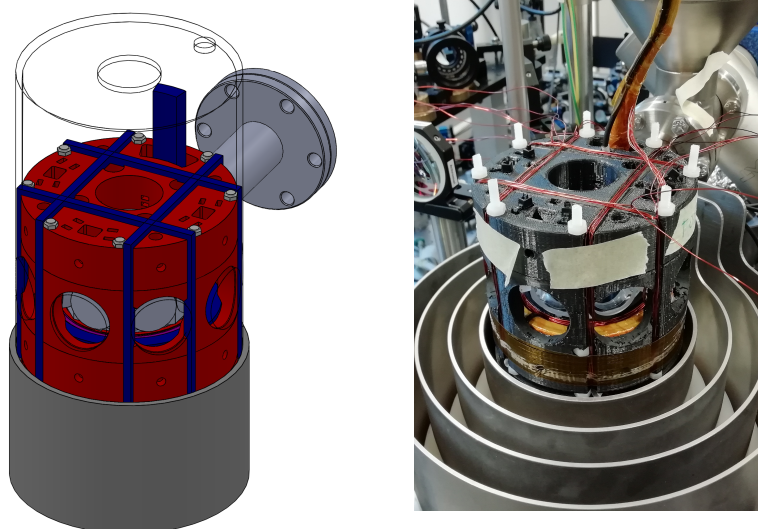


Figure 2.6: (left) CAD design of the apparatus. 3D-printed structure (red), magnetic coils (blue) and the science chamber (light gray, partially hidden) are contained in the innermost layer of the magnetic shield (dark gray). (right) The apparatus before assembly of the upper half of the magnetic shield. The 3D-printed structure is visible (black plastic). The vertical cables are routed through the shield. The MOT coils (orange) are visible, as well as other compensation coils.

Great care has been taken in designing the support structure. This structure holds firmly all the magnetic coils and antennas, allows full optical access to the glass cell, allows routing of the cables, is non-magnetic and can be assembled around the existing vacuum chamber without opening it. The resulting design of the support is rather complex and additive manufacturing using FDM (Fused Deposit Modeling) 3D-printing has been used to realize the object. In FDM 3D-printing, a thermoplastic material is heated and extruded by a small nozzle in form of fused filament of 0.2-1 mm diameter. The nozzle is mounted on a computer-controlled moving head to deposit the filament in layers, and the shape of each layer is changed to realize the 3D object. This technology allows fast and low-cost prototyping, great freedom of design, and the use of non-magnetic materials.

The weakest point of FDM 3D-printing is the available materials, that may be unsuited for realizing an apparatus that requires solidity and long-term stability. The most common material is PLA (PolyLActide), a non-toxic and low-melting-point thermoplas-

tic with great characteristics for 3D-printing. However, once printed it is a brittle material and highly hygroscopic, characteristics that make it unreliable for long-lasting components. The second most common material is ABS (Acrylonitrile Butadiene Styrene), that produces strong and reliable prints, at the cost of higher extruding temperatures (and toxic fumes). However, the high extrusion temperature and the subsequent high thermal contraction of the material make it difficult to realize large (10 cm) pieces because of the “warping” of the plastic induced by internal stresses. A material of recent availability is PET-G (PolyEthylene Terephthalate with Glycol addition), that offers superior mechanical properties than PLA and does not suffer from deformations as ABS, while also being easy to print. We chose this material to realize the internal support structure.

The support structure (Fig. 2.6) is made of four pieces: a pedestal that is glued to the bottom internal layer of the shield, two identical pieces (top and bottom) that hold antennas and magnetic coils and a central spacer to separate the latter. The structure has an octagonal symmetry as the science chamber. Stable alignment between the pieces is guaranteed by interlocking structures printed in the parts. Another weak point of FDM 3D-printing is the weak tensile strength of the object along the growth direction (delamination). We circumvented this problem by inserting 8 long Nylon threaded rods, glued to the pedestal and running across the structure. Nuts screwed on these rods compress all the pieces of the structure together, providing the tensile strength along the weakest axis. The support structure was realized in-house using a Makerbot Replicator 3D-printer. After realization, the dimensions of the piece are very close to the CAD design, with the maximum shrinking of the material found to be less than 1%.

Since this support structure is rigidly mounted to the bottom half of the magnetic shield, careful assembly was required to avoid damages to the science chamber. The bottom half of the shield is held on 1” stainless-steel poles using adjustable mounts and has been aligned to center the apparatus around the science chamber. The upper half of the shield is assembled from above and “closed” on the finished apparatus. To lower/lift the upper half causing minimal disruption to the setup no components are attached to it.

### 2.2.5 Magnetic coils

To apply controllable magnetic fields on the sample, pairs of magnetic coils are placed inside the innermost layer of the magnetic shield. Each coil is composed of several turns of copper wire and designed to maximize field uniformity and to minimize interaction with the shield.

For a couple of thin circular loops of wire, the magnetic field produced by a circulating current  $I$  along their axis is  $B_z = \frac{\mu_0 \mu_r}{4\pi} \frac{2\pi R^2 I}{(z^2 + R^2)^{3/2}}$  and its curvature at the center is zero when the radius of the loops  $R$  is equal to their distance (Helmholtz configuration). For coils of finite size, not all the loops can be in the Helmholtz configuration at the same time, and the magnetic field produced by a loop can be analytically expressed [103] in

cylindrical coordinates  $(\rho, z)$  as

$$B_\rho = \frac{Cz}{2\alpha^2\beta\rho} [(R^2 + \rho^2 + z^2)E(k^2) - \alpha^2K(k^2)]$$

$$B_z = \frac{C}{2\alpha^2\beta} [(R^2 - \rho^2 - z^2)E(k^2) + \alpha^2K(k^2)]$$

where  $R$  is the radius of the loop,  $E$  and  $K$  are the complete elliptic integrals of first and second kind, and the constants are defined as

$$\alpha^2 = R^2 + \rho^2 + z^2 - 2R\rho$$

$$\beta^2 = R^2 + \rho^2 + z^2 + 2R\rho$$

$$k^2 = 1 - \alpha^2/\beta^2$$

$$C = \mu_0 I / \pi$$

To design the magnetic coils, we evaluated this equation and optimized the distance between the coils for minimal curvature of the field using numerical optimization. However, the presence of the shield modifies the magnetic field produced by the coils. To minimize this effect, we placed the most critical coils as close as possible to the science chamber, far from the magnetic shield walls.

A pair of circular coils produce the MOT and levitation magnetic field. They are realized with 6 turns of square copper tubing (3x3 mm in size), firmly attached to the support structure. The copper tubing is wrapped in fiberglass for insulation, shaped and glued with epoxy resin for stability. Cooling water is circulated in the tube to dissipate the heat due to the high MOT and magnetic-trap current (up to 50 A). No heating of the coils is observed even during continuous operation. The tube exits the shield from two small-diameter holes in the top and bottom, to be connected to the hydraulic and electric apparatus. These coils are designed to produce a magnetic gradient along  $z$  of  $0.433 \text{ G cm}^{-1} \text{ A}^{-1}$ .

Another pair of coils (BCompZ.fine) generates the high-stability vertical field. Since this field is the most critical for field inhomogeneities, the coils are placed very close to the glass cell, precisely in the Helmholtz configuration, and tightly glued to the support structure. Numerical simulations of the effect of the shield show that these coils are not strongly affected because they are sufficiently far away from the magnetic shield. The field generated by these coils was measured (Fig. 2.7a) with the shield assembled and found it to be within 2% of the expected value in the center. A similar geometry is used to realized two pairs of coils (BCompZ.coarse) for bias field and gradient along the  $z$ -axis.

Compensation of fields and gradients along the  $x$ - and  $y$ -axis is performed with two pairs of square coils that are wound outside the support structure. We evaluated the field of the square coils by appropriate numerical integration. These coils are much larger and closer to the shield than the previous and we found their field to be significantly distorted (Fig. 2.7b), however they are meant to generate very weak compensation fields and their homogeneity is not critical. All of the compensation coils are realized using

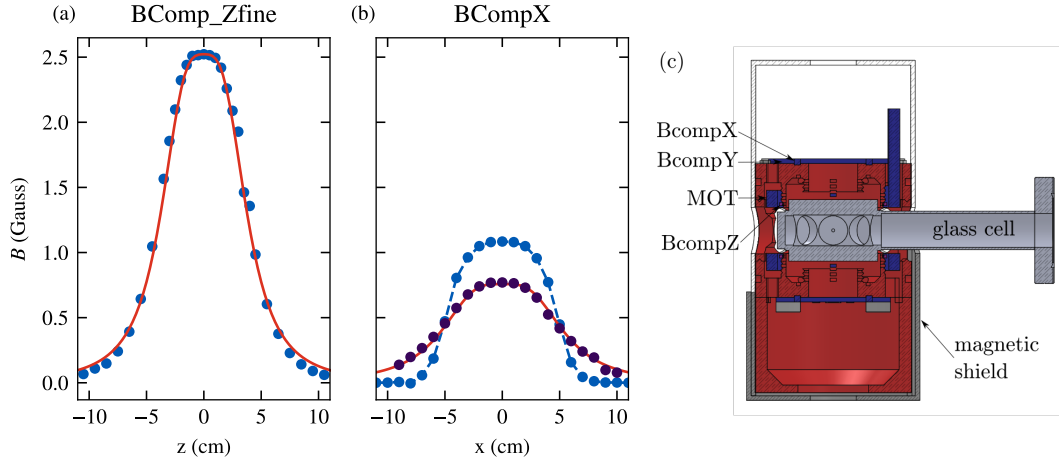


Figure 2.7: (a) Field produced by the coils with a current of 1 A for the highly-stable magnetic field. The field was measured with the shield mounted (blue points) and is in agreement with Eq. 2.2.5 (red line) in the absence of the shield. (b) Field produced by the compensation coils along the  $x$ -axis with a current of 1 A. In the absence of the magnetic shield (purple points) the field agrees with the calculations based on the coils geometry (red line). The presence of the shield (blue points) strongly affects the field distribution. (c)  $y - z$  section of the apparatus.

solid copper enameled wire, being non-magnetic and providing insulation at the same time.

### 2.2.6 Antennas and microwave system

To drive transitions between different Zeeman states of the sample, we require a system to generate microwave fields at 1.7 GHz. As general requirements, the system must be capable of fast ( $< 1 \mu\text{s}$ ) switching on and off of the microwave fields, possibility of generating at least two different frequencies with high relative frequency stability and controllable phase jumps between the two and, lastly, sufficient power to drive two-photon Raman transitions in the atoms. The realized microwave system is schematically described in Fig. 2.8.

To generate two tones with known relative frequency and phase, a direct digital synthesis device (DDS) is used to produce two  $\approx 100$  MHz signals ( $f_1$  and  $f_2$ ) that are then up-converted in the microwave range by the high-frequency mixer. The DDS is based on the Analog Devices AD9958 chip, and offers two output channels with 0.1 Hz frequency resolution and  $2\pi \cdot 2^{-14}$  rad phase resolution. Running on the same clock, the two channels are phase coherent. This DDS allows for changes in the frequency, amplitude and phase of each channel with 100 ns time resolution and maximum update rate of 30 kHz, allowing to perform fast manipulations of the internal states. The two outputs are combined together and a controllable attenuator (Minicircuits ZMAS-3)

name	direction	$ B $ (G)	$\frac{\partial B}{\partial i}$ (G/cm)	N	M	$d$ (mm)	$r$ (mm)
MOT	$z$	1.34	0.433	3	2	30	36
BcompZ_coarse	$z$	1.05	0.373	2	2	32	33
BcompZ_fine	$z$	<b>2.606</b>	0.898	3	3	32	32
BgradZ	$z$	0.50	0.186	2	1	32	32
BcompX	$x$	<b>1.08</b>	0.19	2	2	47	86
BcompY	$y$	<b>1.08</b>	0.19	2	2	47	86
BgradX	$x$	<b>1.08</b>	0.19	2	2	47	86
BgradY	$y$	<b>1.08</b>	0.19	2	2	47	86

Table 2.2: Coils mounted in the experimental apparatus. The values for  $|B|$  are computed at the atoms position for the Helmholtz configurations driving the coils with a current  $I = 1$  A. Given  $i$  the axial direction of each coil,  $\frac{\partial B}{\partial i}$  is the gradient along  $i$ , computed at the atoms position for a current of  $I = 1$  A in the coils. Values in boldface were measured, while the others have been calculated from the coils geometry.

allows smooth ramping of the signal amplitude using an analog voltage control. The two-tone signal is then up-converted by mixing it with a carrier.

To generate fast and time-accurate switching of the fields a 1.670 GHz carrier is produced using a microwave synthesizer (Marconi Instruments 2024) that can be switched on/off in 20 ns, with negligible jitter, using a TTL signal. This carrier acts as local oscillator in a high-frequency mixer (Minicircuits ZEM-4300+) that converts the two-tones signal from the DDS to the desired 1.77 GHz. For better frequency stability, a 10 MHz external reference is fed to the DDS and to the microwave synthesizer.

The mixer for up-conversion produces a higher sideband around 1.771 GHz, a lower sideband around 1.571 GHz and the carrier leak. Since only the higher sideband will be resonant with the atomic transition, we suppress the other components to reduce the amount of power lost by non-linearities in the final amplification stage. A lumped-elements bandpass filter (Minicircuits VHF-1760+ high-pass filter and VLF-1500+ low-pass filter) suppress the carrier and the lower sideband. We find that after filtering the higher sideband has amplitude 20 dB higher than the other two components, however a pre-amplification of the signal is necessary before the following stage. We monitor the signal at this stage with a coupler.

Finally, the signal is amplified using a high-power amplifier (Minicircuits ZHL-100W-272+) to reach the necessary power to drive two-photon transitions. At the output of the amplifier, a multi-stub tuner (Maury Microwave Triple-stub 1819A) is placed to impedance-match the antenna. Since substantial power losses ( $2 \text{ dB m}^{-1}$ ) are introduced by the RG-174 connection cable to the antenna, we kept the cable length at minimum by mounting the amplifier as close as possible to the apparatus.

The antennas installed in the apparatus radiate the field to the sample, and are fed by RG-174 coaxial cable that runs through the apertures in the magnetic shield. We realized antennas of several geometries and installed them in different positions inside the apparatus (Fig. 2.9).

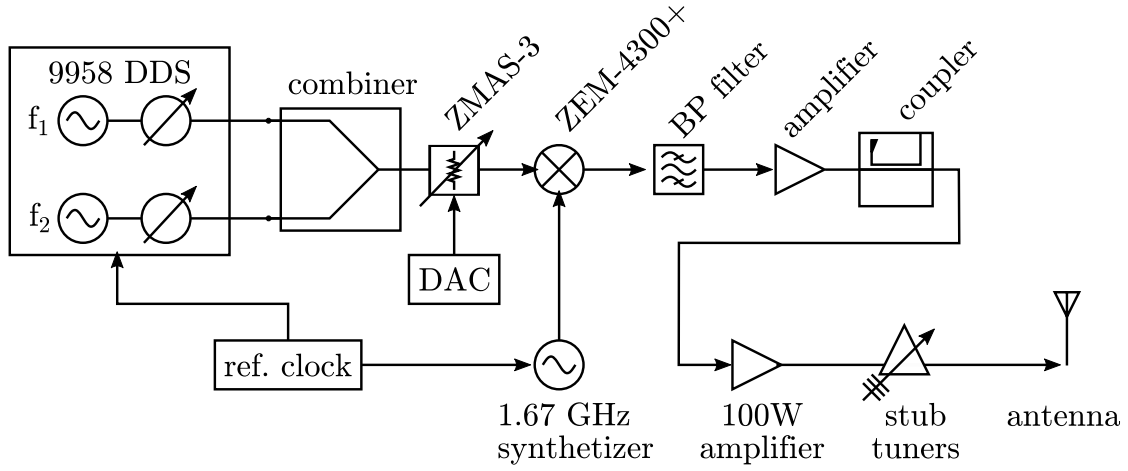


Figure 2.8: Schematic representation of the microwave circuit. From left to right, the two  $\approx 100$  MHz tones generated by the AD9958 board are combined, attenuated and finally up-converted to 1.7 GHz using a mixer. A band-pass filter removes the unnecessary frequency components, and two amplifiers raise the power before the the signal reaches the antenna near the sample.

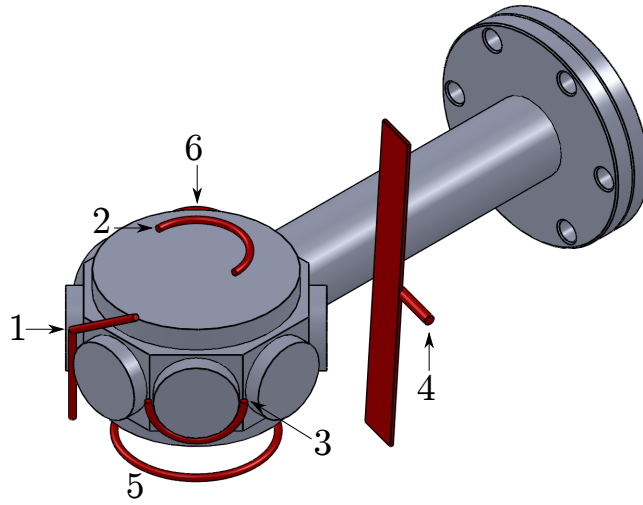


Figure 2.9: Antennas installed in the experimental apparatus. 1: “dipole-ant”, 2: “hook-vert”, 3: “hook-side”, 4: “GSM-ant”, 5: “MHz-loop”, 6: “kHz-loop” (in the back). The arrows indicate the feed point for the antennas.

A first kind of antennas we realized are “hook antennas”, where a piece of solid copper wire ( $\approx 1$  mm thick) is soldered at the end of a coaxial cable and bent in a semicircular shape. The antenna can be matched at the desired frequency by trimming the length of the copper wire. We placed two of these antennas (“hook-side” and “hook-vert”) with different position to have a different polarization of the field on the sample. The antennas were matched before installation at 1.77 GHz, away from the apparatus, by observing the reflected power using a directional coupler. However, further matching of the antennas is possible after installation using the stub-tuners at the output of the amplifier. After completion of the apparatus, we optimized the antennas emission with the stub-tuners, using another antenna to pickup the emitted field. After optimization we reached Rabi frequencies up to 10.3 kHz on the  $|1, -1\rangle \rightarrow |2, 0\rangle$  transition.

A commonly used geometry is the resonant dipole antenna, where two thin conductors of length  $\lambda/4$  (where  $\lambda$  is the wavelength at the frequency of interest) are placed end-to-end and fed at their center. The impedance of dipole antennas can be tuned by changing the angle between the conductors: when the angle is  $180^\circ$  the impedance is  $73\Omega$ , and decreases as the angle is reduced. We realized a dipole antenna (“dipole-ant”) by separating the inner conductor and the shielding of a RG-174 coaxial cable, cutting them to length ( $\approx 4.5$  cm) and adjusting their angle. We matched the antenna with the method described before, reaching similar performance than the hook antennas. After matching with the stub-tuners, this antenna has an emission bandwidth around 2 MHz.

Since the frequency band of 1.8 GHz is used for GSM cellular communication (DCS/GSM-1800), dipole antennas emitting at this frequency are commercially available. These devices have been properly engineered for optimal (far-field) transmission,  $50\Omega$  impedance and are available at low cost, hence we modified one of such antenna (part number 1052630002 from Molex, LLC) for RG-174 connection. Tests before installation of the magnetic shield showed that this antenna, compared to the home-built dipole antenna, reached 50% higher Rabi frequency if placed in the same position. In the realization of the apparatus with the magnetic shield, however, its large size made it impossible to install the antenna close to the sample. We found very poor performances of this antenna (“GSM-ant”) in the final apparatus, probably because of the bigger distance from the sample and the presence of conductive material near the antenna.

Finally, in our apparatus we anticipated the need of driving other RF transitions. We installed an antenna (“RF-loop”) for emission at 500 kHz: a 8-turn wire loop with diameter 32 mm and wire thickness 0.3 mm. Another antenna (“MHz-loop”) is aimed at 20 MHz emission: a single loop with diameter 61 mm made of 1.25 mm thick, solid-copper wire.

### 2.2.7 Optical traps

To achieve coherently-coupled spinor BECs, a spin-independent trapping potential is required to avoid separation of atoms in different Zeeman sub-states. Off-resonant light allows to apply potentials independently of its spin state, differently from magnetic trapping that is inherently sensitive to the sample spin state. In general the optical potential created by a laser beam is sensitive to the particular spin state of the sample,



depending on the polarization of the beam and the direction of the magnetic field that sets the quantization axis. In the particular case of linearly polarized beams orthogonal to the magnetic field however, the potential is spin-independent [104], hence all our beams use this configuration.

We realized differently shaped optical-dipole traps using 1064 nm laser beams. We use a continuous-wave fiber laser (Azur Light Systems ALS-1064-50-I-SF) to produce up to 40 W of infrared laser light, that is then distributed to three different beam paths. An AOM (Gooch & Housego 3110-197) along each path is used as fast optical switch, the zeroth order of the beam being blocked and the first order launched in a large-mode-area photonic crystal fiber (NKT Photonics LMA-PM-10) to be delivered to the sample. The RF amplitude driving each AOM is controlled by a PID controller (SRS SIM960) to stabilize the power out of the fiber and each AOM is driven at a different frequency to avoid standing-wave effects when multiple traps are used contemporaneously. Each fiber output is placed close to the sample, the output power is sampled with a beam-sampler (BS, Thorlabs BSF10-C) and a photodiode (Thorlabs DET36A2) for the stabilization circuit. Each trapping beam has different optics to reach the sample, of which a schematic representation is given in Fig. 2.2.7.

The main trapping beam (*Cigar*) is used to capture thermal atoms after the Gray Molasses stage and to evaporate the cloud until condensation. The light from the optical fiber is collimated by a  $f = 60$  mm lens, then is transmitted through a Polarization Beam Splitter (Thorlabs PBS253) before being bounced by two pointing mirrors. A  $f = 200$  mm lens focuses the beam on the sample to a waist of  $18 \mu\text{m}$ . On the sample, the Cigar beam propagates along the  $x$  axis, approximately 1 mm below the center of the MOT magnetic field quadrupole and is polarized linearly along  $y$ . The tight focus and the high power of 7 W are necessary to achieve high trapping depth and capture the thermal atoms. The power is then gradually reduced during evaporative cooling.

A second beam (*Xaxis*) crosses the Cigar beam orthogonally and is used to increase the trapping frequency along the  $x$ -axis. A  $f = 50$  mm lens collimates the light from the optical fiber, then a PBS is used to clean the beam polarization. The beam passes through two  $f = 100$  mm cylindrical lenses (Thorlabs LJ1567L1-B) forming a 1:1 telescope. By changing the distance between these lenses, one of which mounted on a micrometric stage, the astigmatism of the beam is changed to adjust the horizontal radius of the beam at the position of the sample. Its vertical waist of  $72 \mu\text{m}$  is placed at the position of the sample, while the horizontal radius can be increased up to several millimeters. A maximum power of 5 W is used and the beam is linearly polarized along  $z$ .

A third beam (*Ellipt*) is superimposed to the Cigar beam. The output of an optical fiber is collimated, the polarization cleaned by a PBS then the beam enlarged by a 1:3 telescope. The astigmatism of the beam can be adjusted with a cylindrical telescope like the Xaxis beam. A piezoelectric element tilts one of the mirrors along the beam path to finely align the beam along the vertical direction and ensure optimal superposition with the Cigar. A PBS then combines the Ellipt and Cigar beam before the last  $f = 200$  mm focusing lens. On the sample, this beam has vertical waist of  $30 \mu\text{m}$ , horizontal radius

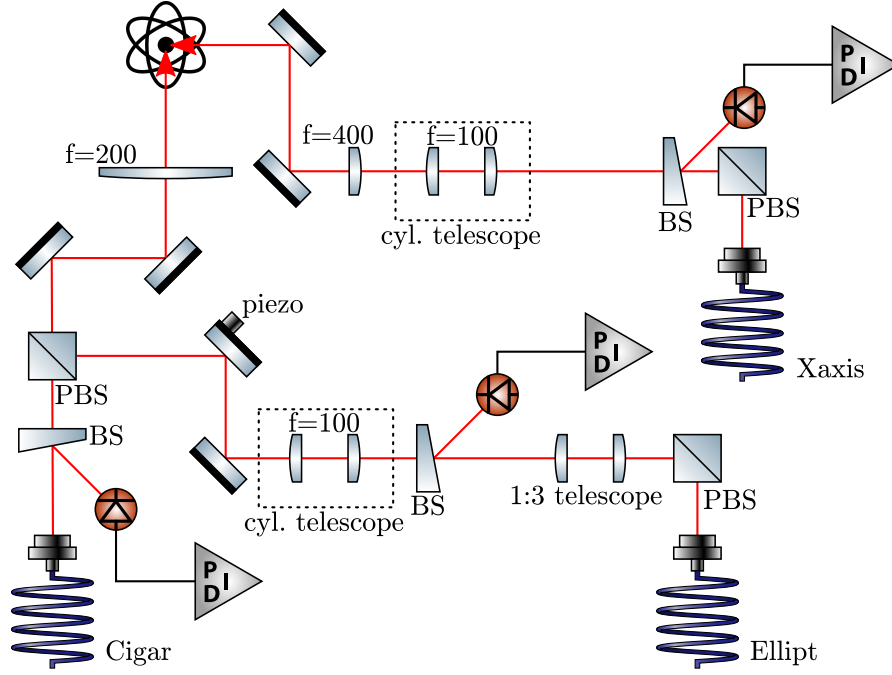


Figure 2.10: Optical elements of the optical dipole traps. Each beam is launched from an optical fiber, collimated with a suitable lens. A Polarizing Beam Splitter (PBS) is placed after the fiber when additional polarization stability is desired. Beam samplers (BS), photodiodes and PID controllers stabilize the power of each beam. Adjustable cylindrical telescopes allow to change the astigmatism of the Ellipt and Xaxis beam. Finally, a focusing lens and two pointing mirrors allow to place each beam on the sample. All focal lengths are in millimeters.

up to 2 mm and is polarized along  $z$ .

### 2.2.8 SRS current source

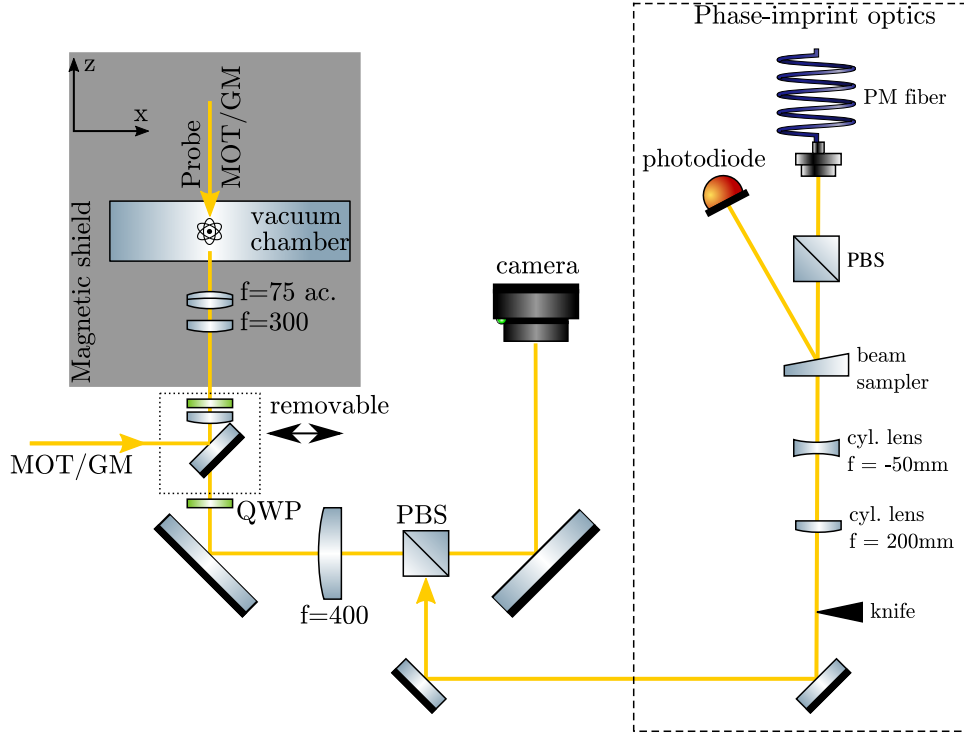
To generate an highly-stable magnetic field, we drive the BCompZ<sub>fine</sub> coils using a laser driver (SRS LDC501) as low-noise current source. The laser driver can supply up to 500 mA of current with a rms current noise of 1.5  $\mu$ A, maintaining a very low long-term drift of less than 5 ppm [105]. An analog modulation input allow for external control of the output current, that we use to generate in-shot ramps of magnetic field. The analog input is controlled by a floating DAC board to avoid the insertion of electronic noise due to ground-loops. The current from the laser driver is controlled by a battery-powered switching circuit to allow for fast turn on and off of the magnetic field using a TTL signal.

### 2.2.9 Imaging systems

Two imaging systems allow to observe the ultracold atom sample, one along the  $z$  axis and one along the  $x$  axis.

The principal imaging system is along the  $z$  axis as most of the observations of the sample are expected to happen along this direction. A circularly-polarized probe beam illuminates the atoms from above, resonant to the  $|F = 2\rangle \rightarrow |F' = 3\rangle$  transition. The light is then collected by two objective lenses, an achromat with  $f = 75$  mm (Thorlabs AC254-075-A) and a spherical one with  $f = 300$  mm (Thorlabs LA1484-A). These lenses are positioned 3 mm apart in a doublet configuration with an effective focal length of 60.8 mm and have numerical aperture 0.2. This doublet is mounted such that the atoms are on its imaging plane. Along this direction also the vertical MOT and GrayMolasses beams access the sample, hence a mirror, a  $f = 60$  mm lens and a quarter-wave plate are mounted on a movable contraption. The optics are placed in the imaging path during the MOT phase and then removed to allow for the imaging light to reach the camera. The image is formed on the camera using a  $f = 400$  mm 2" spherical lens (Thorlabs LB1862-A). A quarter-wave plate is placed before this lens to convert the probe light to linear polarization, and the light is then transmitted through a PBS. The PBS is necessary to superimpose the phase-imprint beam described in Section 3.3 on the imaging path. Finally, a fast CMOS camera (Hamamatsu Orca Flash 4.0) is placed in the imaging plane of the system. Overall, this imaging system has a (calculated) resolution of 1.8  $\mu$ m and a magnification of 6.5.

In the second imaging system, a probe beam is sent along the  $x$  axis and onto the sample. To image the atoms, a  $f = 50$  mm lens, with the atoms on the focal plane, is mounted inside the shield. A second identical lens is used to complete the imaging system. Along this direction also the high-power 1064 nm optical-dipole trap beam propagate, hence the imaging light is bounced off a dichroic mirror to separate it from the infrared beam, and an additional interferential filter removes the remaining infrared light. The dichroic mirror is mounted on a movable rail, to send the imaging light in two alternative paths. On the first path, the imaging light is sent directly onto a CCD

Figure 2.11: The imaging system along the  $z$  axis.

camera (Stingray F-201B), to realize an imaging system with magnification of 1. In the second path, an additional single  $f = 300$  mm lens relays the image to a second camera. In this case the atomic image is demagnified by a factor 3 and is used to image the sample size in the MOT.

### 2.2.10 Laser light source

To prepare and image the ultracold atoms sample we utilize laser light near the D2 line ( $3^2S_{1/2} \rightarrow 3^2P_{3/2}$ ) and near the D1 line ( $3^2S_{1/2} \rightarrow 3^2P_{1/2}$ ). Two independent systems produce laser light at 589 nm, each system being frequency-locked on the desired spectroscopic line using saturated-absorption spectroscopy. Each system allow the production and control of individual laser beams that are then distributed to the experimental apparatus using optical fibers. The optical setup used to produce, stabilize and control the laser light is described in [85].

The first laser system generates light on the  $|F = 2\rangle \rightarrow |F' = 3\rangle$  closed transition of the D2 line, that is our main transition for laser cooling and imaging (*cooling transition*). This system produces laser light for the Zeeman slower, 2DMOT, 3DMOT, DarkSpot repumper, push beam and imaging beams that are described in the next Section. From this transition, however, atom can populate the  $F = 1$  manifold of the ground states via off-resonant excitation of  $F' = 2$ , hence they are repumped to  $F = 2$  using the

$|F = 1\rangle \rightarrow |F' = 2\rangle$  transition of the D2 line (*repumper transition*). We generate the repumper light by phase-modulation (for Zeeman slower and 2DMOT stages) or by frequency-shift (for the DarkSpot repumper) of the cooling light.

The second laser system generates light on the  $|F = 2\rangle \rightarrow |F' = 2\rangle$  transition of the D1 line. We use this light for the GrayMolasses laser cooling stage, also described in the next Section, as this technique can not be used on the D2 line in  $^{23}\text{Na}$ .

## 2.3 Production of the condensed sample

To produce the condensed sample we use the magnetic-shield compatible procedure described in [85], optimized to the new experimental apparatus.

### 2.3.1 Atomic source

In the HV chamber, a stream of hot atoms is evaporated in the oven and slowed by a 12 cm long Zeeman-Slower (ZS). The ZS is formed with four permanent magnets and a 1" laser beam propagating against the direction of effusion of the evaporated atoms and linearly polarized orthogonal to the magnetic field. The laser beam has intensity  $160 \text{ mW/cm}^2$  and has three spectral components: 50% of the light power is red-detuned 330 MHz from the cooling transition to slow the atoms, 25% of the power is resonant with the repumper transition, while 25% is not resonant.

The slowed atoms enter the capture region of a 2-dimensional Magneto-Optical Trap (2DMOT) [106, 107]. The 2DMOT magnetic gradient is generated by the same permanent magnets of the ZS, while two orthogonal, circularly-polarized beams provide the optical cooling and trapping. The beams have intensity  $10 \text{ mW/cm}^2$  and have the same spectral composition as the ZS beam, apart from the cooling frequency that is red-detuned 13 MHz from the cooling transition. Each beam is retroreflected after passing through the chamber to provide the counter-propagating light necessary for MOT trapping. The 2DMOT confines the atoms along the  $z$  and  $x$  axis.

Along the  $y$  axis, a laser beam resonant to the cooling transition pushes the atoms in the 2DMOT trough the differential pumping channel and into the science chamber.

### 2.3.2 MOT

In the science chamber, a three-dimensional Dark-Spot MOT (DSMOT) captures the atoms coming from the HV chamber. In a Dark-Spot MOT, high atoms density is achieved by trapping most of the atoms in a dark state, and bringing only the atoms leaving the trapping region to the bright state [108].

Six beams propagating along three orthogonal directions provide the optical cooling and trapping. Each beam has an intensity of  $2.3 \text{ mW/cm}^2$  on the atoms, it is red-detuned 18 MHz from the cooling transition and it is circularly polarized. The MOT magnetic field gradient ( $7.5 \text{ G cm}^{-1}$  along  $z$ ) is generated by the MOT coils driven in anti-Helmholtz configuration. The atoms in the  $F = 1$  manifold are repumped to  $F = 2$  by an hollow-core beam of repumper light. The hollow-core beam is produced from a

gaussian beam using an Axicon and a circular obstacle. The obstacle is imaged on the atoms with a  $f = 150$  mm spherical lens. In the DSMOT, up to  $5 \times 10^9$  atoms are trapped with temperature  $\approx 300$   $\mu$ K in a 13 s loading time.

### 2.3.3 Gray Molasses

Gray Molasses (GM) is a sub-Doppler cooling technique similar to the optical molasses, with the key difference that coherent-population-trapping is used to trap the atoms of lowest velocity in a dark state. Once in the dark state, the atoms do not interact with the cooling light anymore, allowing for higher densities of the atomic cloud using lower intensity of the cooling light [109]. GM cooling of sodium was demonstrated in [110] using the  $|F = 2\rangle \rightarrow |F' = 2\rangle$  D1 transition and we utilize the same procedure with slight modifications.

After the MOT stage, the magnetic field is suddenly switched off. Right after, the GM light is turned on with intensity 150 mW/cm<sup>2</sup> and blue detuning 40 MHz for 0.5 ms. This light pulse cools the atoms in the DSMOT to  $\approx 25$   $\mu$ K, with nearly unity capture efficiency. The detuning is then suddenly increased to 100 MHz and the light intensity slowly ramped to 0 in 5 ms with a piecewise-linear ramp. This intensity ramp reduces the temperature of the atoms to  $\approx 13$   $\mu$ K.

### 2.3.4 Evaporative cooling

We produce a BEC in  $|1, -1\rangle$  using the protocol described in [102].

After the GM stage, a magnetic quadrupole field of  $\frac{\partial B}{\partial z} = 13$  G/cm generated by the MOT coils is turned on, and, at the same time, the Cigar trapping beam is turned with potential depth of 440  $\mu$ K. Depending on the experimental procedure, also the Xaxis trapping beam is turned on. The magnetic quadrupole is then adiabatically compressed to  $\frac{\partial B}{\partial z} = 22$  G/cm in 500 ms. The thermal cloud trapped by the magnetic quadrupole begins to accumulate in the optical trap, and up to  $30 \cdot 10^6$  atoms are collected after a loading time of 4 s. The magnetic quadrupole field is then ramped to  $\frac{\partial B}{\partial z} = 7.7$  G  $\perp$  cm, below the value to compensate for gravity, to release the atoms that have not been collected by the optical trap.

The sample is now held by a combination of optical and magnetic potentials (Hybrid Trap). A first evaporation cooling stage is performed by lowering the potential depth of the Cigar beam to 52  $\mu$ K in 2 s. We then transfer the atoms to a purely optical trap applying a vertical high-stability bias field and then adiabatically removing the magnetic quadrupole. By switching off all other magnetic fields, only the high stability bias field remains.

Finally, the power of the optical trap is ramped down for the final evaporative sequence. This final evaporation stage can vary, depending on the desired sample to produce. In a typical experiment, the Cigar power is lowered with a 1 s-long exponential ramp to a final trap depth of 3.5  $\mu$ K, producing a BEC of  $\approx 2 \cdot 10^6$  atom and negligible thermal component. The final trapping frequencies in this condition are  $\omega_x, \omega_y, \omega_z = [500, 500, 10]$  Hz.

## 2.4 Measurement of magnetic field stability

The high sensitivity of the sample to magnetic fields, that is the motivation for installation of the magnetic shield itself, can actually be used as a tool for the precision measurement of the shielding performance, using the sample itself as a magnetometer. Atomic magnetometers have been studied for more than a century now, both in hot vapors and in cold samples. These magnetometers are usually based on magneto-optical effects (for a review see [111]) and can reach accuracy of the order  $100 \text{ pG}/\sqrt{\text{Hz}}$ . In our case, however, the quantity of interest is the magnetic field stability after the creation of the Bose-condensed sample, hence we performed the measurement using the BEC itself. To determine the magnetic field at the sample location we used spectroscopic measurements, determining the resonant frequency of transitions between Zeeman sub-levels.

In a condensed sample, however, effects such as atom-atom collisions and mean-field frequency shifts are much more prevalent than in low density thermal clouds. For example, substantial atom loss happens in less than 1 ms for our sample in  $|1, -1\rangle$ , if one of the state of  $|2, m_F\rangle$  is also populated (with the exception of the state  $|2, -2\rangle$ ) because of two-body spin-relaxation collisions [56]. However, these effects can be made small by suitable choice of the Zeeman states used for the measurement.

### 2.4.1 Spectroscopic measurement of magnetic field

Transitions between two Zeeman sublevels interacting with monochromatic near-resonant radiation can be described as a two-level system, with populations evolving under the Bloch equations. We define the Rabi frequency  $\Omega = \frac{\langle 2|\vec{\mu}\cdot\vec{B}|1\rangle}{2}$  induced by the magnetic field  $\vec{B}$  of the radiation, where  $\vec{\mu}$  is the magnetic dipole operator, and the detuning  $\delta = \omega_{rf} - \omega_0$  between the transition frequency  $\omega_0$  and the frequency of the radiation  $\omega_{rf}$ . In the case of magnetic dipole transitions between sub-levels of the electronic ground state the spontaneous emission rate is negligible and the evolution is always coherent.

This two-level system treatment allows to measure the modulus of magnetic field at the position of the sample with high precision, by determining the transition frequency  $\omega_0$  between Zeeman sub-levels, as long as they have different  $m_F$ . From the Bloch equation, the population transfer from the initial state  $|1\rangle$  to  $|2\rangle$  in time  $t$  is given by the simple formula

$$\rho_{22} = \frac{\Omega^2}{\Omega^2 + \delta^2} \sin^2 \left( \frac{\sqrt{\Omega^2 + \delta^2}}{2} t \right), \quad (2.3)$$

where the excitation probability  $\rho_{22}$  can be simply measured from the populations ( $N_{1,2}$ ) of the states. For consistency, we will express the population transfer via the fractional population imbalance  $Z = (N_2 - N_1)/(N_1 + N_2) = 2\rho_{22} - 1$ . Equation 2.3 gives the usual sinc-shaped spectroscopy curve when a pulse of length  $\pi/\Omega$  ( $\pi$ -pulse) is applied for different detunings (Fig. 2.12). One can then determine the resonant frequency of the transition applying a  $\pi$ -pulse of microwave coupling with known Rabi frequency  $\Omega$  at different value of  $\omega_{rf}$ , measure  $Z$ , and finally fit Eq. (2.3) with  $\omega_0$  as free parameter.

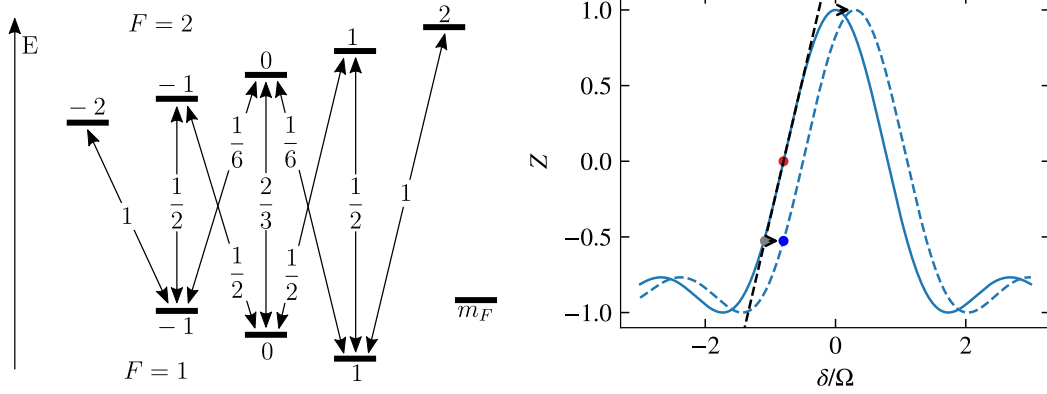


Figure 2.12: (left) Transitions between Zeeman states of the ground state of  $^{23}\text{Na}$ . The vertical direction represents the energy of the level in a finite magnetic field. Each double-arrow represents a single-photon transition, with its squared Clebsch–Gordan coefficient indicated on the arrow. (right) Schematic representation of the “side-of-fringe” technique. The solid line is the spectroscopic curve for the resonant frequency  $\omega_0$ . At detuning  $\Delta_1$  the population in the states is equal (red dot). If the resonant frequency changes to  $\omega'_0$ , the spectroscopic curve becomes the dashed line and the measured population changes (blue dot).

To perform magnetometry measurements, however, a single-shot measurement of  $\omega_0$  is preferable. We use a “side of fringe” technique to achieve, in a limited range of magnetic fields, a linear relationship between the magnetic field and the measured  $Z$ . In the neighbourhood of the two  $Z = 0$  crossings, corresponding to a detuning of  $\delta_1 = 0.7987\Omega$ , the sinc-like spectroscopy curve is linear. To determine the resonant frequency from the measured  $Z$  it is then sufficient to Taylor-expand Eq. (2.3) around  $\delta_1$  to get  $\rho_{22} \approx \rho'_{22}(\delta - \delta_1) + \rho_{22}(\delta_1)$  where  $\rho'_{22}$  is the first derivative in  $\delta$  given by

$$\rho'_{22} = -\frac{2\delta\rho_{22}}{\Omega^2 + \delta^2} + \frac{\Omega^2\delta t}{(\Omega^2 + \delta^2)^{3/2}} \sin\left(\frac{\sqrt{\Omega^2 + \delta^2}}{2}t\right) \cos\left(\frac{\sqrt{\Omega^2 + \delta^2}}{2}t\right).$$

This measurement requires only the accurate measurement of the Rabi frequency to calculate a conversion between  $Z$  and  $\omega_0$ .

This procedure to measure fluctuations in the resonant frequency is schematized in Fig. 2.12. The blue solid curve is  $Z$  as function of  $\delta$  after a  $\pi$ -pulse, with (initial) resonant frequency  $\omega_0$ . After determining  $\omega_0$  and  $\Omega$ , the frequency of the oscillator is set to have a detuning  $\pm\delta_1$  (red point). The frequency of the oscillator is now fixed and the procedure of detuned  $\pi$ -pulses repeated. If the value of the resonant frequency changes to  $\omega'_0$  (blue dashed line), the measured  $Z$  changes accordingly (blue point) and we can estimate the new resonant frequency using the linear approximation (black dashed line). In this way a simple linear relation between the measured populations and the detuning can be used to measure the magnetic field stability.



### Two-photon coupling for magnetometry

The magnetometry method described above requires that the system is well approximated by the two-level system description. However, we are interested in characterizing the magnetic shield in the presence of a bias field of  $\approx 100$  mG, hence we are in the low-magnetic-field limit where the quadratic Zeeman effect is negligible. In this limit, radio-frequency transitions between two states in the same manifold cannot be excited separately because their energy differences are all equal and all the levels will participate to the dynamics. The possibility of using a three-level system is ruled out by the interaction constants between  $|1, \pm 1\rangle$  and  $|1, 0\rangle$ , that are such that the system will phase-separate, reducing the coherence time if all these states are populated. This reasons makes unfavorable the use of radio-frequency transitions in the  $F = 1$  manifold.

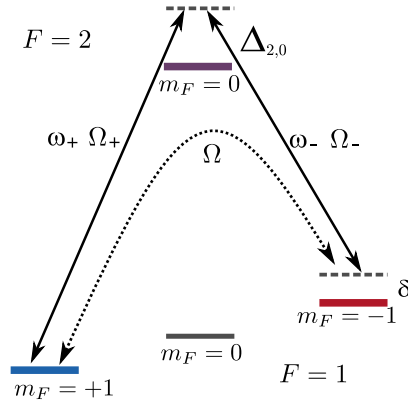


Figure 2.13: Zeeman levels used in the two-photon coherent coupling. The single-photon transitions are driven with Rabi frequencies  $\Omega_{\pm}$  and detuning  $\Delta_{2,0} \pm \delta/2$ . An effective two-photon coupling is realized with Rabi frequency  $\Omega$  and detuning  $\delta$ .

To overcome this problem we used two-photon coupling (Fig. 2.13), to excite the transition  $|1, -1\rangle \rightarrow |1, +1\rangle$  without populating  $|1, 0\rangle$ . To realize the two-photon transition, two microwave fields (with frequencies  $\omega_+$ ,  $\omega_-$ ) drive the single-photon transitions  $|1, \pm 1\rangle \rightarrow |2, 0\rangle$  off-resonance, with detuning  $\Delta_{2,0} \pm \delta/2$ . The microwave frequencies are such that  $\hbar(\omega_+ - \omega_- + \delta)$  equals the difference in energy between the levels  $E_{|1,-1\rangle} - E_{|1,+1\rangle}$ . The single-photon transitions have Rabi frequencies  $\Omega_+$  and  $\Omega_-$ , respectively. In the limit  $\delta \ll \Omega_{\pm} \ll \Delta_{2,0}$  the system is well described by the two-level picture. The transition  $|1, -1\rangle \rightarrow |1, +1\rangle$ , is coupled with effective Rabi frequency

$$\Omega = \frac{\Omega_+ \Omega_-}{2\Delta_{2,0}}$$

and detuning  $\delta$ .

Using a two-photon transition has some key advantages for this measurement. First, the atom loss from the virtual state can be made arbitrary small by increasing  $\Delta_{2,0}$ . Second, the inter- and intra-component interaction constants of the states  $|1, \pm 1\rangle$  are

similar so no phase-separation occurs and the density-dependent frequency shift is reduced. The third advantage comes from the limited frequency stability of our microwave chain (Section 2.2.6). Since it is not possible to distinguish changes in the resonant frequency of the transition from changes in frequency of the driving field, the latter should be negligible to measure accurately the former. For transitions between the two hyperfine manifolds (that could be singularly addressed even without the two-photon coupling scheme) the expected frequency fluctuations in our microwave system are of the order 1 kHz, strongly limiting the precision of the measurement. However, due to the construction of the microwave system, these frequency changes are common-mode when a two-photon coupling is used. Since the two-photon transition is at twice the linear Zeeman splitting ( $\approx 140$  kHz for our working bias field) changes in the reference frequency translate to shifts in the mHz range, and are not limiting the precision of the measurement.

### 2.4.2 Long term magnetic field stability

We performed several long experimental runs to characterize the different noise sources of the apparatus. In each of these runs, we measured accurately the Rabi frequency of the two-photon coupling and performed identical experimental cycles to measure fluctuations in resonant frequency, using the procedure explained in the previous Sections.

However different in details, these experimental sequences consists of preparing the sample in  $|1, -1\rangle$ , apply the two-photon coupling to  $|1, 1\rangle$  for a given time and measure the population in the two states. The populations are measured applying a Stern-Gerlach procedure, in which the sample is released from the trap and a vertical magnetic gradient of 8 G/cm is applied for 15 ms to spatially separate the sample in its  $m_F$  components. After a short repumper light pulse to bring the atoms to the  $F = 2$  manifold, the sample is imaged using absorption imaging. The populations  $N_{\pm 1}$  of the states  $|1, \pm 1\rangle$  are then measured integrating their optical density.

#### Environmental noise

To measure the magnetic noise in the environment we performed the spectroscopic measurement described in the previous Section without the magnetic shield installed. We conducted several tests trying to isolate the main sources of magnetic noise. During these tests, however, we required rather strong two-photon couplings (of the order of 1 kHz) to overcome the fluctuations in the magnetic field, hence we could not use very high detunings from the virtual state ( $\Delta_{2,0} = 10$  kHz). Despite our system not being exactly two-level, the population in the intermediate state is always below 10% and for these preliminary results can be neglected.

The atomic population measured in one of these experimental runs is reported in Fig. 2.14a. In this run, a 1 ms long two photon microwave pulse with Rabi frequency  $\approx 250$  Hz transfers nearly half of the population to  $|1, +1\rangle$ . The transfer is quite stable over a 40 minutes period, suggesting a shot-to-shot fluctuation of the order 0.7 mG. After 40 minutes however, the transferred population changes abruptly, indicating a sudden

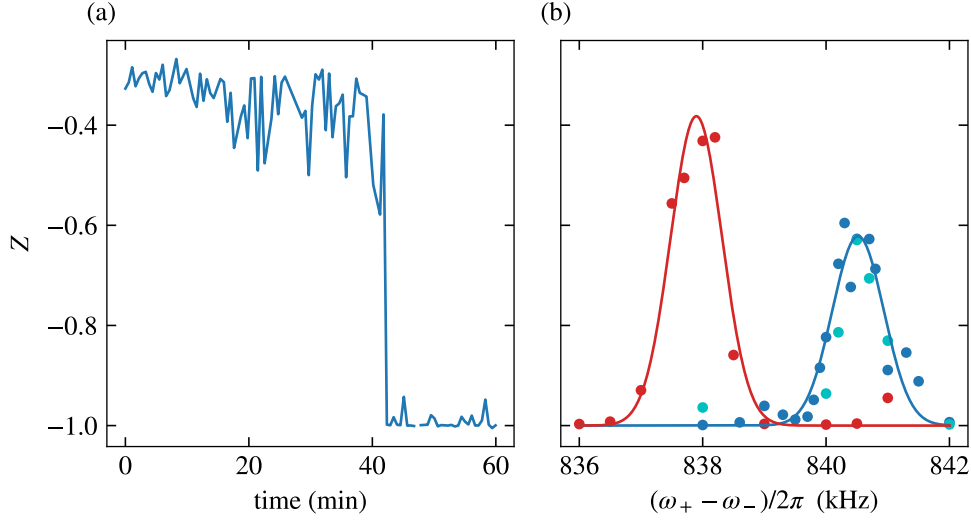


Figure 2.14: (a) Transferred population after 1 ms of Rabi coupling between the  $|1, -1\rangle$  and  $|1, +1\rangle$ , without the shield installed. Fluctuations in the populations are caused by change in the background magnetic field. A sudden jump in the field happens around 40 minutes. (b) Shift in the resonant frequency, without the shield installed, caused by a car parked close to the laboratory. We measure the resonant frequency by scanning the frequency difference between the microwave fields and measuring the population transferred to  $|1, +1\rangle$ . The starting peak (blue) is shifted when the car is placed (red) by 2.6 kHz, corresponding to a change in the background field of  $\approx 1.8$  mG. When the car is removed, the resonant frequency returns to the previous value (cyan). Continuous lines are gaussian fits to the data.

change in the magnetic field. We found several causes for uncontrollable shifts in the magnetic field: the operation of a high-current magnetic trap in a nearby laboratory for example was producing repeatable field shifts of the order of a few mG. A somewhat curious example of uncontrolled field jump is reported in Fig. 2.14b, where we found 2 mG shift in the background magnetic field depending on the presence of cars in the parking spot right outside the laboratory. In this case, we were able to identify the problem by placing and removing the same car and observing the background field jumping between two different values in a reproducible way.

We characterized the magnetic noise created by the electric equipment at the frequency of 50 Hz by repeating spectroscopic measurements at different phases with respect to the AC current of the electric line and found a shift of the order of 2 mG. However, since our experiment is phase-locked to the electric line, this noise is not present in the long-term measurements presented so far.

From this characterization we were able to place an upper bound on fast magnetic noise and understood that our main source of magnetic noise are uncontrolled field shifts and the electric line. The amplitude of this noise lies, as expected, in the mG range and

the magnetic shield can attenuate it sufficiently to reach the target stability.

### Long-term stability with the magnetic shield

After installation of the magnetic shield, we performed a similar characterization of the magnetic field stability.

For this measurements, we set a bias field of 264 mG and each single-photon transitions has Rabi frequency 4.5 kHz and is blue-detuned by  $\Delta_{2,0} = 60$  kHz. For these parameters the population in the virtual state is negligible and the system is effectively a two-level system with Rabi frequency  $\Omega/2\pi = 162.1 \pm 0.1$  Hz, that is independently measured by performing a Rabi flop for up to 12 ms (Fig. 2.15a). We release the sample from the trap, apply the microwave coupling for a time  $t = \pi/\Omega = 3.08$  ms, separate the populations with the Stern-Gerlach procedure and measure the populations. The atoms number in the BEC has been set to  $0.8 \times 10^6$  atoms. The time to perform an experimental cycle is 16 s.

This experimental sequence is repeated continuously, alternating between red and blue detuning of the resonance ( $\Delta = \pm\Delta_1$ ). This procedure allows to remove systematic errors like change in Rabi frequency or in the imaging procedure. The resulting variation of polarization of the sample during a 4-hour long experimental run is reported in Fig. 2.15b. The populations of the red and blue detuned extraction are initially set equal by scanning the frequency of the microwave coupling, and then the experiment is left running steadily. It is evident that a continuous slow drift in the magnetic field brings the polarizations of the two extractions to slowly diverge. The shift in the resonant frequency has been also confirmed by two spectroscopic measurements at the start and at the end of this experimental run, that have been found different by 20  $\mu$ G.

For each experimental repetition, the magnetic field value is calculated using the technique described in the previous Section. In Fig. 2.16a, the magnetic field change over a 4-hour run is reported. The two series of red- and blue-detuned extractions are considered separately as independent measures, since they are taken in separate experimental cycles, hence for every series we measure the field every 32 s. We observe a substantial agreement of the two series on the measured magnetic field, meaning that fluctuations in the Rabi frequency are negligible. A systematic difference in the calculated field remains, caused either by a wrong calibration or by the presence of some additional effects that have not been taken into account (presumably mean-field effects or AC Stark shift). When the mean values of each series are removed, however, the two series overlap and we can extract the field fluctuations separately. These fluctuations are well below 10  $\mu$ G over an hour, with a slow drift over longer timescales.

To further examine the characteristic of the fluctuations, the Allan deviation of the two series is shown in Fig. 2.16b. We observe that the magnetic field fluctuation has mainly a white noise and a drift component. The white noise has  $\sigma \approx 3$   $\mu$ G and an Allan deviation proportional to  $\tau^{-1/2}$ , so is dominant at integration times up to 15 minutes. This noise is the variation of the field from one experimental cycle to another and can plausibly be caused by current noise in the magnetic coils, fast magnetic noise from the environment, or random remnant magnetization in the apparatus. The drift component

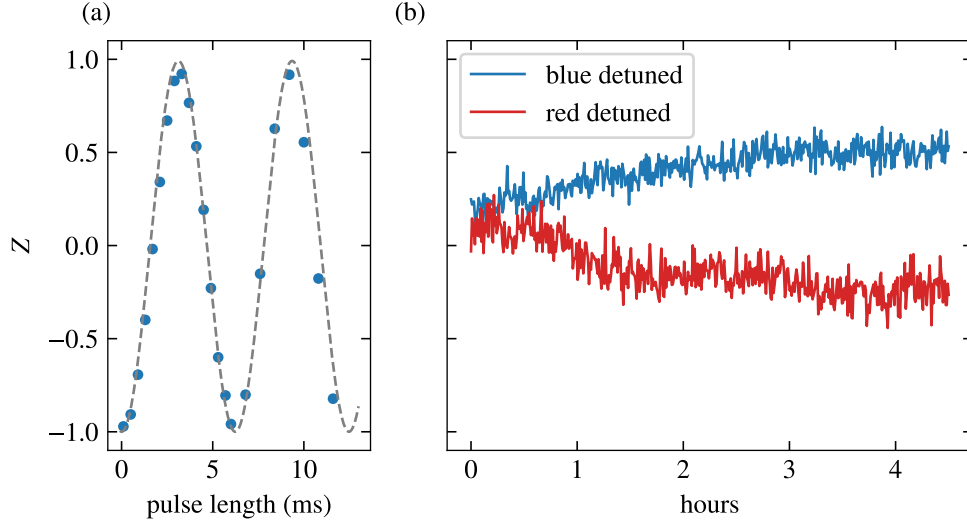


Figure 2.15: (a) Calibration of the Rabi frequency performing a Rabi flop on an expanded BEC. Points are the observed  $Z$  as function of the length of the microwave pulse. The dashed line is the fitted sinusoidal function to extract the Rabi frequency. (b) Observed fluctuations of the population after a detuned  $\pi$ -pulse. The two data series are initial red detuned (red color) and blue detuned (blue color) from the resonant frequency by  $\delta_1$ . The experiment is run continuously and the transferred population drifts from the initial value following the magnetic field change.

has a very long timescale and it is connected to the long-term stability of our apparatus. For this data-set it appears as divergent with longer integration times (a linear drift has an Allan deviation proportional to  $\tau$ ). However, we have not observed a monotonous drift of the field from day to day operation, hence this drift is more probably a very low-frequency noise caused by slow effects like temperature fluctuations, that appears as a drift for this measurement run. Between the two regimes, we observe a minimum magnetic noise of  $1.2\mu\text{G}$  for integration times of 15 minutes. In the future, the slow drift could be corrected with a feedback loop implemented in the software control of the experiment, possibly extending the minimum noise up to indefinitely long time intervals.

### 2.4.3 Field inhomogeneities

In the discussion reported so far, the spatial extent of the sample has been neglected. In an extended sample, however, the magnetic field and the strength of the coupling can be inhomogeneous in space. These inhomogeneities can prevent the realization of extended samples with uniform properties, hence we characterized both quantities along the weak axis of the Cigar optical trap ( $x$ -axis).

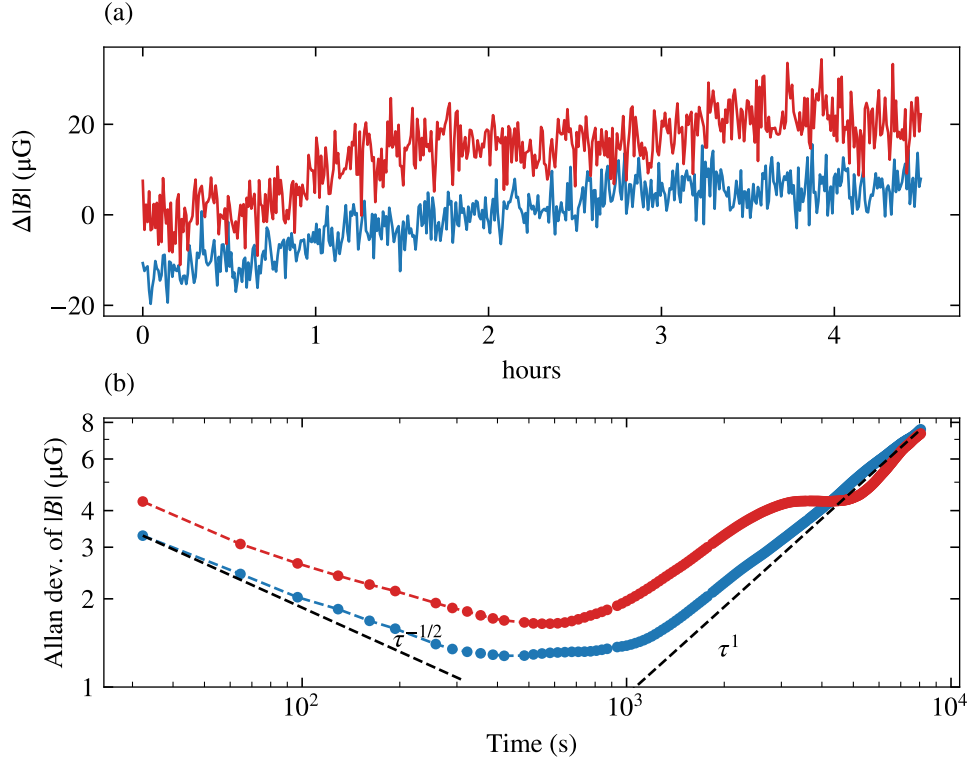


Figure 2.16: (a) Magnetic field calculated from the observed atomic polarization. The two series corresponds to red- (red line) and blue-detuned (blue line)  $\pi$ -pulses. The field is expressed as fluctuation respect to the average value of 260.571 mG. (b) Allan deviation of the field fluctuation. The two series qualitatively agree and the magnetic noise is below 2  $\mu\text{G}$  for integration time of 15 minutes. White noise and linear drift limits are shown as black dashed lines with slopes  $-1/2$  and  $1$ , respectively.

### Magnetic field inhomogeneity

The effect of an inhomogeneous modulus of the magnetic field is to make the resonant condition  $\omega_0 - \omega_L$  dependent on space. To increase the magnitude of magnetic field inhomogeneities, we set a higher magnetic field of 1.3 G by driving the maximum current (500 mA) in the coils. We measured the field homogeneity by measuring the resonant frequency of the two-photon transition in a very dilute thermal cloud, to suppress mean-field shifts of the resonant frequency. The cloud is held in the Cigar optical trap, hence it extends over the  $x$  axis. Starting from a polarized sample in  $|1, -1\rangle$ , we apply a  $\pi$ -pulse to  $|1, +1\rangle$  and immediately after image the populations in the two states, resolving the spatial direction  $x$  (the imaging protocol is presented in Section 3.2). For each position, we obtain the populations  $N_{1,2}$  by integration of the optical density, thus we are able to measure the resonant frequency at each position with the usual spectroscopic

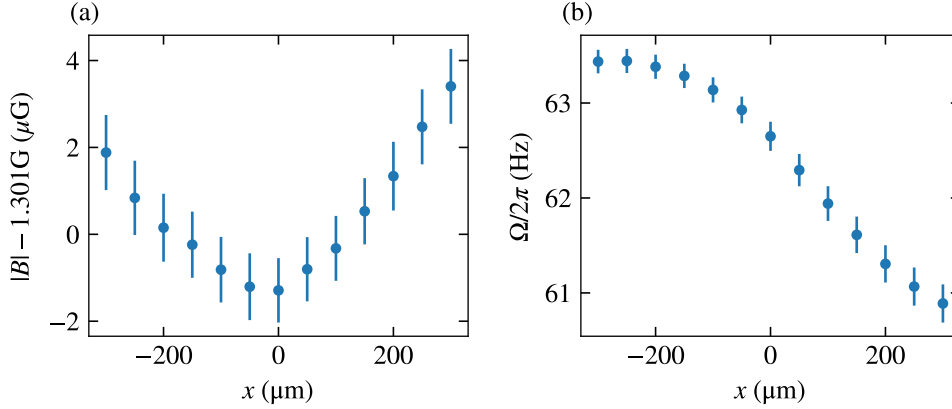


Figure 2.17: (a) Change in the magnetic field for different positions in the optical trap. The magnetic field is measured with spectroscopy of the two-photon transition on a very dilute thermal cloud. (b) Rabi frequency of the two-photon coupling at different positions in the optical trap. The Rabi frequency is measured driving Rabi oscillations on a very dilute thermal cloud. The center of the optical trap is at  $x = 0$ . Errors corresponds to 68% confidence intervals from the fitting routine.

procedure. From the resonant frequency, we then obtain the magnetic field at each position (see Fig. 2.17a). The measured field inhomogeneity is below 4  $\mu\text{G}$  on the typical dimensions of our sample. This measurement sets an upper bound on the magnetic field inhomogeneities, due to possible residual mean-field frequency shifts.

### Coupling inhomogeneities

An inhomogeneous amplitude of the microwave field driving the two-photon coupling translates to different Rabi frequency  $\Omega$  at different positions. Starting from a polarized sample, we drive resonant Rabi oscillations in a very dilute thermal cloud for different evolution time up to 200 ms. With the same protocol previously described we measure the populations at different positions  $x$  as a function of time. We then extract the frequency of the Rabi oscillations fitting a sinusoid and observe a position dependent change of the Rabi frequency Fig. 2.17b of the order of 2%.

#### 2.4.4 Coherence time

As a final characterization measurement, we are interested in the coherence time of our sample. The full description of the decoherence mechanisms requires separate addressing of the different homogeneous and inhomogeneous dephasing terms, and a full characterization is outside the scope of this work. However, since we will be interested in the coherence time in the presence of a stationary coupling, we measure its order-of-magnitude by driving Rabi oscillations on a thermal cloud.

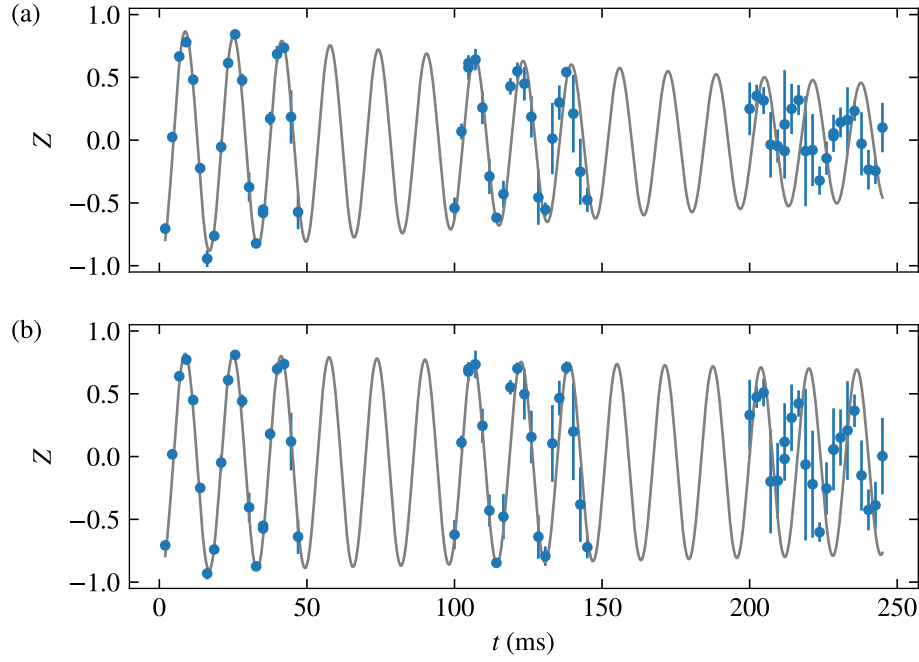


Figure 2.18: Measurement of the coherence time with Rabi oscillations of thermal cloud initially with  $Z = -1$ . In (a), we measure the magnetization integrating over the full cloud, in (b) the integration is limited to a 20  $\mu\text{m}$ -wide region in the center of the cloud. Points and errorbars are mean and standard deviation over 5 experimental repetitions. Gray line is an exponentially decaying sinusoid fitted to the data. The decay times extracted from the fits are  $370^{+140}_{-80}$  ms for (a) and  $1500^{+1100}_{-400}$  ms for (b).



Starting from a very dilute thermal cloud in  $|1, -1\rangle$ , we turn on the coupling on resonance with Rabi frequency of 61 Hz, starting a Rabi oscillation. With the protocol described in the previous Sections, we then measure the populations at different positions. In Fig. 2.18a we show the magnetization integrating on the full extension of the cloud. On this magnetization, we fit an exponentially decaying sinusoid, and extract a damping time of  $370^{+140}_{-80}$  ms. This value, however, is affected by the spatially inhomogeneous Rabi coupling, hence we restrict the integrating region to a 20  $\mu\text{m}$ -wide region in the center of the cloud (Fig. 2.18b). In this case, the fitted damping time is  $1500^{+1100}_{-400}$  ms. With this characterization we confirm that the coherence time of the sample is sufficiently high to observe spin-dynamics for as long as hundreds of ms, as required in the designing phase of the experimental apparatus.



# Chapter 3

## Observation of Magnetic Solitons

Solitonic waves are a widespread phenomenon in many fields of physics. An overlook on solitonic waves in single- and two-component BECs has been given in Chap. 1, while in this Chapter I will focus on a particular kind of solitonic waves in two-component BECs, the *Magnetic Soliton* (MS). MSs exist in two-component BECs with repulsive intra- and inter-component interaction constants, if the former are equal and only slightly larger than the latter. This is the case of mixture of  $|1, \pm 1\rangle$  of  $^{23}\text{Na}$ . MSs are localized spin excitations on a homogeneous and non-polarized background. The condition of similar interaction constants causes the total density of the system to remain constant, and an explicit analytical solution can be obtained for the spin excitations.

In this Chapter I will present the experimental production and observation of MSs in  $^{23}\text{Na}$  condensates. During my PhD I developed a protocol to deterministically produce MSs using phase-engineering of the condensate, together with a multiple-imaging procedure to reconstruct all the relevant quantities of the MS. With this protocol I investigated the dispersion-less in-trap dynamics of MSs. Moreover, I studied the robustness of MSs by producing multiple MSs that then collide with each other.

In the first Section I will introduce the theoretical background on MSs developed in [1] and present some numerical simulations of their dynamics. In the second Section, I present the procedure used to measure the density and relative-phase profile of the sample. In the third Section, I present the production of MSs using a phase-engineering technique, its characterization and the observation and identification of MSs in the sample. In the fourth and fifth Sections are reported further experimental investigations of the in-trap dynamics and evolution of the MSs. In the last Section, collisions between solitons of same- and opposite-magnetization are studied.

### 3.1 Theoretical background on Magnetic solitons

The analytical expression of a MS can be obtained starting from two coupled 1DGPEs for a two-component BECs in a uniform potential [1]. The reduction of the GPE to 1DGPE follows Section 1.1.1. The result can then be extended to a trapped gas using

the local-density approximation. I recall that in the case of mixtures of  $|1, \pm 1\rangle$  of  $^{23}\text{Na}$ , since  $g_{11} = g_{22} = g$  and  $g - g_{12} = \delta g \ll g$  (see Section 1.2.1), the energy of spin excitations is much smaller than the energy of density excitations, the former can be excited leaving the latter in the ground state.

It is then convenient to separate the (total) density dynamics from the spin dynamics. By defining the total density  $n = n_1 + n_2$  and the *magnetization*  $Z = \cos(\theta) = \frac{n_1 - n_2}{n}$  the pseudo-spin order parameter can be rewritten as

$$(\Psi_1, \Psi_2) = \sqrt{n}(\cos(\theta/2)e^{i\phi_1}, \sin(\theta/2)e^{i\phi_2}). \quad (3.1)$$

Moreover, one can introduce the total phase  $\phi_b = \phi_1 + \phi_2$  and the relative phase  $\phi_a = \phi_1 - \phi_2$ . The characteristic length and velocity of the spin modes are the previously introduced spin-healing length  $\xi_s$  and the spin-sound velocity  $c_s$ . Since solitonic solutions are moving at a constant velocity  $V$ , it is convenient to express them in term of the moving spatial variable  $\zeta = (x - Vt)/\xi_s$ . By rewriting the GPEs in the new variables and imposing equal densities at infinity, one can obtain the analytical result for the densities and phases profiles in the presence of a MS moving at dimensionless velocity  $U = V/c_s$  as

$$\begin{aligned} n_{1,2} &= \frac{n}{2} \left[ 1 \pm \frac{\sqrt{1 - U^2}}{\cosh\left(\zeta\sqrt{1 - U^2}\right)} \right] \\ \cot \phi_a &= -\sinh\left(\zeta\sqrt{1 - U^2}\right) / U \\ \tan \phi_b &= -\sqrt{1 - U^2} \tanh\left(\zeta\sqrt{1 - U^2}\right) / U \end{aligned} \quad (3.2)$$

From these equations, one observe that the MSs have a dimension of the order of  $\xi_s$  and propagate at a velocity less than the spin-sound velocity ( $|U| \leq 1$ ). Their magnetization at the centre has value  $Z_0 = \sqrt{1 - U^2}$ , it is maximum for stationary solitons and vanishes as they approach the spin-sound velocity. Their width, instead, increases with velocity and the total magnetization is constant and equal to  $\pi\xi_s$ . Across the soliton, the relative phase  $\phi_a$  exhibits a finite jump of  $\pi$  and this value does not depend on the soliton velocity. A finite jump is present also in the total phase, however its value depends on  $U$ . Fig. 3.1 illustrates the density and phase profiles of MSs for different values of  $U$ .

Taking the difference in grand-canonical energies of the gas in the presence and in the absence of the soliton, we obtain the energy of a MS

$$\epsilon = n\hbar c_s \sqrt{1 - U^2}, \quad (3.3)$$

showing how this energy decreases for higher velocities of the soliton. The dispersion-less dynamics of solitons resembles the one of particles, however a peculiar consequence of Eq. (3.3) is that MSs behave as particles with negative effective mass. Since solitons of negative effective mass are not stable against snake fluctuations in higher dimensions [112, 47], it is crucial to their observation that the sample is effectively one-dimensional.

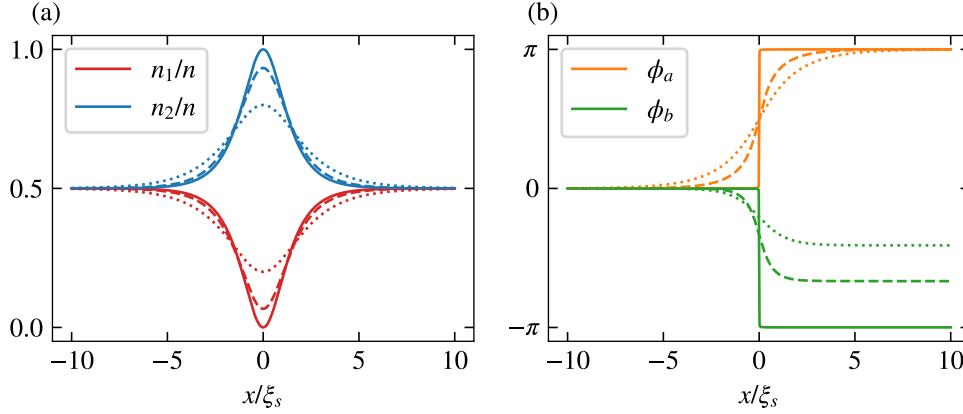


Figure 3.1: Density (a) and phase (b) profiles for a MS with  $U = 0$  (solid lines),  $U = 0.5$  (dashed) and  $U = 0.8$  (dotted). As the velocity is increased, the density profiles of the soliton gets smaller but wider, and the phase jumps are spread on a correspondingly wider region. The jump in relative phase is always  $\pi$ , while the jump in total phase is smaller for higher velocities.

The behaviour of MSs in a trapped gas can be understood considering the local density approximation along the  $x$ -axis, i.e. the analytical solution just found in an inhomogeneous total density profile  $n(x)$  such as a Thomas-Fermi density profile  $n(x) = n_0(1 - x^2/R_x^2)$ . During the motion of the soliton its energy is conserved, hence it follows from Eq. (3.3) that a reduction of density  $n$  is tied to a decrement of velocity  $U$ . Then, a MS moving towards the low-density edges of the sample gradually slows until it stops, reverse its motion and accelerates towards the centre of the sample again, starting an oscillatory motion in the trap. For a soliton starting at the centre of the trapped sample with velocity  $U_0$ , the amplitude  $L$  and period  $T$  of the motion are given by

$$L/R_x = \sqrt{1 - (1 - U_0^2)^{1/3}} \quad (3.4)$$

$$T/T_x = \frac{4}{\pi} \sqrt{\frac{g}{\delta g}} \int_0^L \frac{1 - (x/R_x)^2}{R_x \sqrt{[1 - (x/R_x)^2]^3 - 1 + U_0^2}} dx. \quad (3.5)$$

### 3.1.1 Simulations

We simulated the in-trap dynamics of MS and collisions between MSs by numerical integration of the 1D coupled GPEs for the parameters of our experiment. The simulations have been performed using a high-performance simulation package [113].

#### In-trap dynamics

We simulated a condensate of  $1 \cdot 10^6$  atoms, equally distributed in the two components, in a harmonic trap with axial trapping frequency 9.5 Hz and radial trapping frequency

530 Hz. After obtaining the ground state of the system via imaginary-time evolution, the analytic phase and density profile of a MS is imprinted on the components, for different initial velocities  $U$ , and real-time evolution performed. The MS is imprinted at the centre and, in time, move towards the edge of the condensate with approximatively constant velocity. As it moves towards the lower-density edge, the MS slows down due to energy conservation, until it stops and reverse its motion. Together with the MS, sound waves are excited with the imprint procedure. One can observe how the sound waves, travelling at  $c_s$ , are faster than the MS, but reach the edge of the condensate and disperse. The MS, instead, oscillates in the trap unaltered.

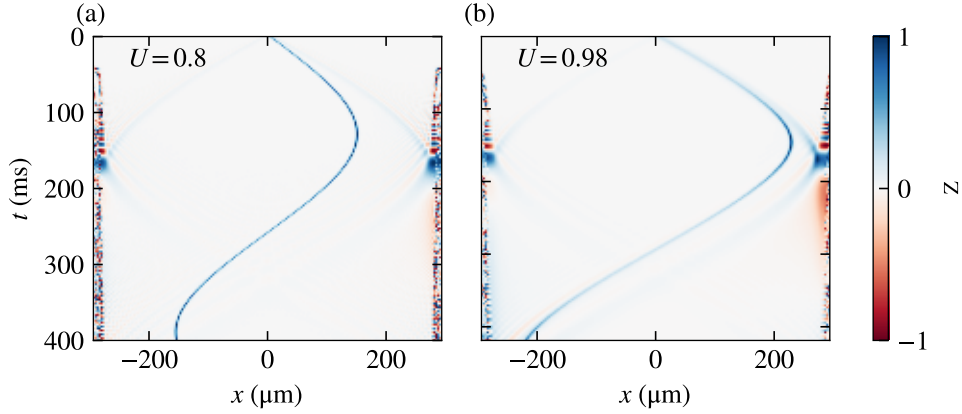


Figure 3.2: Magnetization of a MS oscillating in a harmonic trap. A MS is imprinted at the centre with initial velocity  $U = 0.8$  (a) and  $U = 0.98$  (b). The soliton of higher velocity travels further toward the edge of the condensate before stopping and returning towards the centre of the trap. Sound waves are produced together with the soliton, travel to the edge of the condensate and then disperse.

### Collisions

Solitons can be robust to excitations of their shape and recover the solitonic profile by releasing the excitation energy, however this robustness is not guaranteed for significant changes in the shape of the soliton. In particular, the interaction between solitons, both being sharp and energetic features, makes their behaviour non-trivial. For example, bright solitons in optical media acquire a time and phase shift during a collision, but recover their shape fully [5]. Magnetic solitons in spin-1 Bose gas, instead, can have elastic and inelastic collisions [114] and are also expected to annihilate under certain conditions [115]. Moreover, most of the studies on solitons have been performed in the field of non-linear optics where there is no limitation in the amplitude of the electromagnetic field. This is in stark contrast with our system, where the maximum amplitude of the spin excitation can not exceed the density of the sample, without producing density excitations.

To study the robustness of the soliton, we simulated collisions between MSs of different magnetization and velocity. Since the MS is an analytical solution only for a homogeneous background, when it interacts with other excitations is not guaranteed that the soliton will survive the collision.

We simulated a condensate of  $1 \cdot 10^5$  atoms, equally distributed in the two components, in a  $100 \mu\text{m}$  wide box. The 1D interaction constants are calculated with radial trapping frequency of 500 Hz and the atom number is such that the chemical potential  $\mu = 2.9 \text{ kHz}$ ,  $\xi_s = 1.05 \mu\text{m}$  and  $c_s = 1.3 \text{ mm s}^{-1}$  are close to the experimental values.

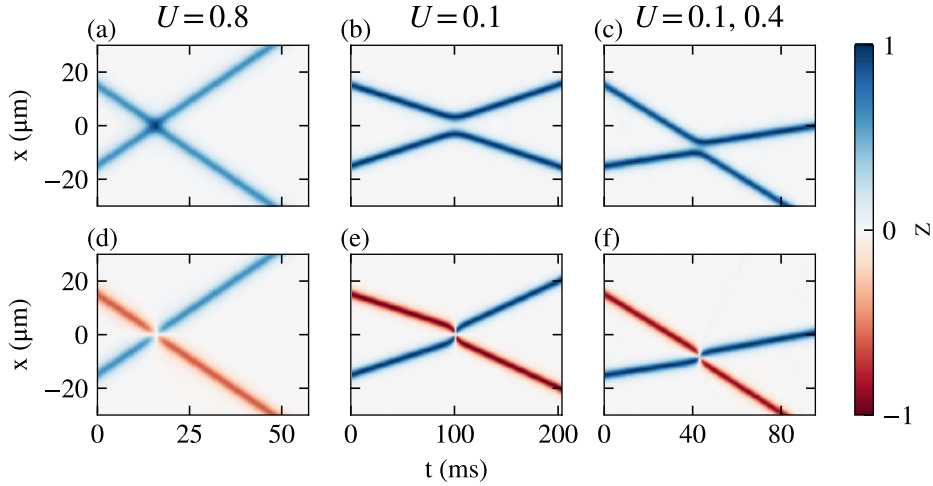


Figure 3.3: Magnetization during collisions of solitons with equal (a-c) and opposite (d-f) magnetization. The solitons are launched  $30 \mu\text{m}$  apart with opposite velocities and collide. Low-magnetization solitons do not interact (a, d), while high-magnetization solitons interact briefly (b, e). (c, f) Collision of solitons of different velocities. Note that different horizontal scales are used in each column.

First, we study collision between solitons of equal magnetization in Fig. 3.3a-c. When fast, low-magnetization solitons collide in Fig. 3.3a, they cross each other without interaction. In fact, fast solitons are close to linear spin waves as the effect of nonlinearities becomes vanishingly small. Slow, high-magnetization solitons in Fig. 3.3b show a different behaviour instead, as they appear not to merge during the collision but to bounce one against the other. This can be intuitively explained by the fact that these two solitons cannot be superimposed without creating a density excitation in the system, as their total peak magnetization would exceed 1. Hence, as the solitons get closer, the energy cost of the density excitation pushes them apart, until they reverse their motion. It is remarkable that, even in the instant of minimum distance, the magnetization between the solitons is lower than their peaks, hence the solitons never completely merge. This “identification” of the solitons with the peak value of the magnetization can be misleading, however, as it is evident in the case of collisions with different velocities in Fig. 3.3c. While no complete overlap between the solitons happens,

during the collision the solitons “exchange” velocity. This fact, necessary to conserve the momentum of each component, *de facto* exchanges the identity of the solitons, that appear to have crossed each other if only their exit trajectory is considered.

Secondly, we study collision of solitons of opposite magnetization. Similarly, fast and low-magnetization solitons in Fig. 3.3d appear to cross each-other without interaction. When slow, high-magnetization solitons collide in Fig. 3.3e, instead, the large excitation in the densities causes an interaction, as can be observed by the shifted trajectory before and after the collision. Their interaction resembles an attractive potential and the solitons emerge from the collision with an advanced position. This interaction happens also when solitons of different velocities collide (Fig. 3.3f). In every case, the solitons are not annihilated by the collision, even if during the collision the magnetization is null everywhere.

These simulations show that solitons are robust against collisions with other solitons, both of equal and opposite magnetization.

## 3.2 Full state reconstruction

In order to reconstruct fully the magnetization profile and relative-phase jump of the MS we take multiple semi-concurrent in-situ absorption images of the BEC, effectively observing all three relevant components of the pseudospin wavefunction (neglecting an irrelevant global phase). The densities of both components of the mixture are imaged using Partial Transfer Absorption Imaging (PTAI) [116] while information on the relative-phase is acquired using an interferometric technique that we developed.

### 3.2.1 Magnetization imaging and MS identification

In PTAI a small fraction of the atoms of the sample are transferred to an auxiliary state that is then used for readout [117]. By using imaging light that is resonant with the auxiliary state but not with the original sample, it's possible to take quasi-non-destructive in-situ imaging of the sample. Using PTAI we are able to control the OD of the sample allowing also the imaging of very dense samples [118], by transferring a limited amount of atoms to the auxiliary state. Moreover, when the extracted fraction is much less than 1, the sample is not significantly disturbed by the imaging and the procedure can be used for taking subsequent images of the same sample.

We use PTAI to image *in-situ* the atoms in  $|1, +1\rangle$  by transferring  $\approx 10\%$  of them to  $|2, 0\rangle$  using a resonant  $11\ \mu\text{s}$  microwave pulse of Rabi frequency  $4.79(4)\ \text{kHz}$ . The transferred atoms are then imaged along the  $z$  axis by a  $5\ \mu\text{s}$  imaging pulse on the  $F = 2 \rightarrow F' = 3$  transition. The atoms in  $|1, -1\rangle$  are similarly imaged by transferring  $\approx 13\%$  of them to  $|2, 0\rangle$  using a resonant  $7\ \mu\text{s}$  microwave pulse of Rabi frequency  $8.60(1)\ \text{kHz}$ . From these two images, and a probe and background images, we measure the optical densities of each state.

The in-situ imaging of the BEC is realized along the  $z$ -axis (see Section 2.2.9), using a CMOS camera capable of acquiring a  $64 \times 1024$  pixel image every  $1.5\ \text{ms}$ , with an exposure



time of 1 ms and a readout and transfer time of  $\approx 0.5$  ms. This camera is connected to a data-acquisition computer over USB 3.0 connection, where the images are collected for analysis. Since we are interested in acquiring both optical densities with the shortest delay possible, the imaging light is pulsed at the end of one exposure of the camera and then at the beginning of the next exposure, allowing us to minimize the time between the two captures ( $\approx 600 \mu\text{s}$ ). For a MS moving at half the spin-sound velocity in a typical sample (2 mm/s), the displacement of the soliton during this time is below our imaging resolution, and we can consider the two images as effectively concurrent.

### 3.2.2 Relative phase imaging

The phase profile of a MS complements the information extracted from the magnetization thanks to the characteristic  $\pi$  jump of the relative phase across the soliton. Imaging of the relative phase of two-component condensate was achieved in  $^{87}\text{Rb}$  [52] and successively used, for example, to observe the phase profile of a vortex [119]. This technique uses a coherent coupling  $\pi/2$ -pulse to interconvert the two components depending on their relative phase. Representing the two-level system as a spin-1/2 on the Bloch sphere, this process is equivalent to rotating the spin such that one of the equatorial components is aligned with the quantization axis.

In our case, however, we aim for simultaneous readout of the populations and of the relative phase. The previous technique completely modifies the populations of the system and, moreover, requires a successive transfer to the imaging state. To obtain the readout of the relative phase and simultaneous transfer to the imaging state, we developed a technique for relative-phase-selective transfer from the  $F = 1$  manifold to the  $F = 2$  manifold via microwave radiation. The  $F = 2$  manifold then becomes the readout state when the atoms are imaged, 3.2 ms after the second PTAI image. Our technique can be equivalently modelled as an interferometer or as a projection on the dark and bright states of a coupled three level system.

### Interferometer description

In the interferometer description, the relative-phase imaging procedure can be explained as follows. We start with a sample in  $|1, -1\rangle$  and then we coherently transfer it to an equally populated mixture (using either a  $\pi/2$  pulse or an Adiabatic Rapid Passage, this does not change the validity of the discussion). This puts each atom in a superposition of  $|1, \pm 1\rangle$  and corresponds to the first beam splitter of the interferometer. Since we are interested only in localized jumps in the relative phase  $\phi(x)$  between the two components, we do not require any knowledge of the global (homogeneous) phase that the two states accumulate with respect to the external microwave oscillator, being this uniform on the whole sample. One can consider, without loss of generality, that all the phases are acting on one of the two states while the other acts as a local oscillator. The following evolution of the system, for example the relative-phase jump of a MS, changes the relative phase in a space-dependent way that carries the information of interest.

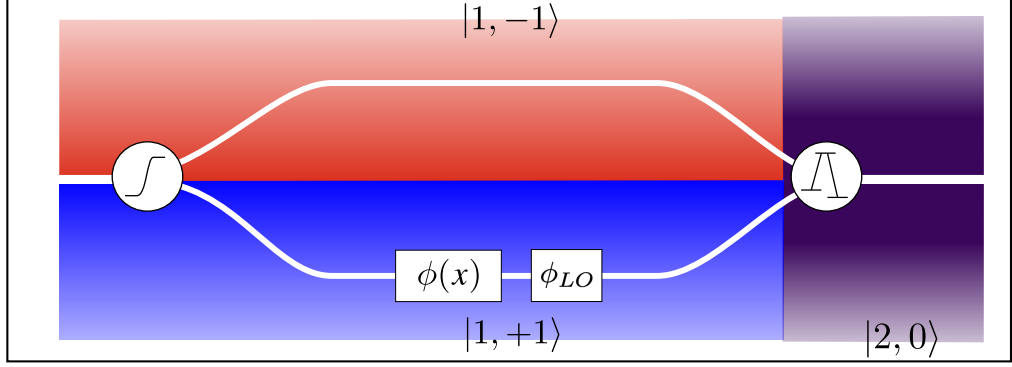


Figure 3.4: Schematic representation of the interferometric measurement technique. From left to right: the mixture of  $|1, \pm 1\rangle$  is created with fixed relative-phase using Adiabatic Rapid Passage. All the phases that are accumulated by the states are represented by the spatial-dependent phase  $\phi(x)$  and the global and spatially uniform phase  $\phi_{LO}$ . A two-tone resonant microwave pulse then projects the two states on the  $|2, 0\rangle$ , where they interfere. The population in this state can then be readout with absorption imaging.

We set the unknown global phase such that the  $|1, +1\rangle$  state carries all the relative phase, then the state of the BEC before the readout can be written as  $|1, -1\rangle + \exp^{i\phi(x)} |1, +1\rangle$ . To perform the readout of the interferometer, we use a two-tone microwave pulse resonant with the  $|1, -1\rangle \rightarrow |2, 0\rangle$  and the  $|1, +1\rangle \rightarrow |2, 0\rangle$  transitions with complex Rabi frequencies  $\Omega_-$  and  $\Omega_+$ . The Rabi frequencies have equal modulus  $|\Omega|$  and differ by their phase:  $\Omega_- = e^{-i\phi_{LO}} \Omega_+$ . The phase of the local oscillator  $\phi_{LO}$  is externally set by changing the phase of one of the two microwave fields. When a short pulse is applied ( $t \ll 2\pi/|\Omega|$ ) we can consider the two transitions in the limit of low transfer [83, Chap. 7] so that each transition gives an independent contribution to the probability amplitude of  $|2, 0\rangle$ :

$$\begin{aligned} |1, -1\rangle &\rightarrow \frac{\Omega_- t}{2} |2, 0\rangle \\ |1, +1\rangle &\rightarrow \frac{\Omega_+ t}{2} |2, 0\rangle. \end{aligned}$$

Then, the probability amplitude of  $|2, 0\rangle$  after the interferometer pulse is

$$C_{2,0} = \frac{|\Omega|t}{2} (1 + e^{i(\phi_{LO} + \phi)}),$$

and the probability of transferring to the readout state is

$$P_{|2,0\rangle} = |C_{2,0}|^2 = \frac{|\Omega|^2 t^2}{2} [1 + \cos(\phi(x) + \phi_{LO})],$$

allowing to extract information about the relative phase by absorption imaging.

### Coherent-population trapping description

An equivalent description of the procedure is based on coherent population trapping (CPT) in a three-level system [120, Chap. 13]. This phenomenon has many applications in atomic physics and arises when two quantum states are coupled through a third state. A superposition of these two states (a dark state) becomes uncoupled to the third, hence it is “trapped”. We consider the state basis  $(|1, -1\rangle, |2, 0\rangle, |1, +1\rangle)^T$  where the two states  $|1, \pm 1\rangle$  are coupled through the state  $|2, 0\rangle$ . In the presence of two driving fields near resonant to the first (second) transition and with Rabi frequencies  $\Omega_1$  ( $\Omega_2$ ) and detuning  $\Delta_1$  ( $\Delta_2$ ), the Hamiltonian of the system in the Rotating Wave Approximation is

$$H = \frac{1}{2} \begin{pmatrix} 2\Delta_1 & \Omega_1^* & 0 \\ \Omega_1 & 0 & \Omega_2^* \\ 0 & \Omega_2 & 2\Delta_2 \end{pmatrix}. \quad (3.6)$$

In the resonant case  $\Delta_1 = \Delta_2 = 0$  the eigenvalues of the system can be readily calculated from the characteristic equation, yielding

$$z \left[ z^2 - \frac{1}{4} (\Omega_1^2 + \Omega_2^2) \right] = 0,$$

that has a solution  $z_0 = 0$  and two solutions  $z_{\pm} = \pm \frac{1}{2} \sqrt{\Omega_1^2 + \Omega_2^2} = \pm \frac{\bar{\Omega}}{2}$  coming from the quadratic expression inside the parentheses. The corresponding eigenvectors are

$$\Phi_0 = \frac{1}{\bar{\Omega}} (-\Omega_2^*, 0, \Omega_1) \quad (3.7)$$

$$\Phi_{\pm} = \frac{1}{\sqrt{2}\bar{\Omega}} (\Omega_1^*, \pm \bar{\Omega}, \Omega_2). \quad (3.8)$$

While the eigenvectors  $\Phi_{\pm}$  correspond to a Rabi oscillation where all three states participate,  $\Phi_0$  is a superposition only of  $|1, -1\rangle, |1, +1\rangle$  that is uncoupled from  $|2, 0\rangle$ . In this framework, our readout procedure reduces to the projection of the state of the BEC onto the basis  $(|\Phi_{-}\rangle, |\Phi_0\rangle, |\Phi_{+}\rangle)$ . The projection weights on this basis depends, at each point in space, on the relative phases between the states  $|1, \pm 1\rangle$  and on the phases of the complex Rabi frequencies  $\Omega_{1,2}$ , hence the basis can be rotated at will by changing the relative phase of the microwave driving fields. After the projection, the population in the readout state  $|2, 0\rangle$  can be imaged, allowing the extraction of information about the relative phase.

### 3.2.3 Interferometer calibration

Practically, several parameters have to be adjusted to obtain an interferometric image with good contrast, and several hardware constraints of our system have to be considered. Considering the microwave setup described in Section 2.2.6, we generate a two-tone signal setting the frequencies of both DDS channels to resonate with the  $|1, \pm 1\rangle \rightarrow |2, 0\rangle$  transitions and then apply a pulse of precise timing using the fast pulse-modulation of

the generator. We observed that significant spectral degradation of the two-tone signal occurs driving the high-power amplifier at its maximum power, with several sidebands produced due to the closeness in frequencies of the two tones. Due to the lack of quadratic Zeeman shift at our working field, these sidebands drive unwanted transitions between Zeeman states. While this is not a problem for the two-photon coherent coupling (the unwanted microwave frequencies are as detuned as the main ones but less powerful), it suddenly becomes problematic when the detuning is zero. We observed an immediate atom loss and uncontrolled population of many Zeeman states when we tested the interferometer at the maximum amplifier power. This problem was solved by reducing the amplitude of the two-tone signal before amplification to 1/10 of its original value.

A second key aspect to be considered is that an effective two-photon Rabi coupling works also for unequal single-photon Rabi frequencies, and is possible to recover full-contrast Rabi oscillations between the states by slightly detuning  $\delta$ . This reasoning does not apply in the interferometric measurement since an equal transfer from the states  $|1, \pm 1\rangle$  is required to achieve maximum contrast. It is then convenient to calibrate the interferometer frequencies and amplitude separately from the values used for the two-photon coupling.

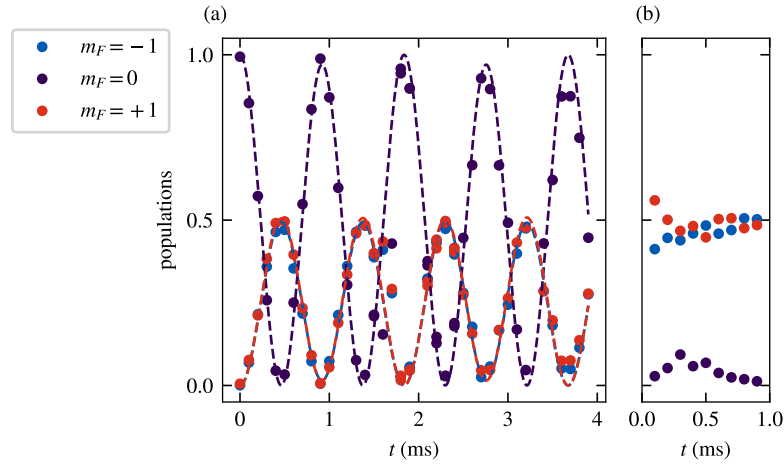


Figure 3.5: (a) Evolution of the three-level system with a two-tone microwave pulse of length  $t$  starting from the state  $|2, 0\rangle$ . Dashed lines are the time propagation of Eq. (3.6) fitted to the experimental points. (b) Evolution of the three-level system with a two-tone microwave pulse of length  $t$  starting from the state  $\frac{1}{\sqrt{2}}(|1, -1\rangle - |1, +1\rangle)$ .

We measure each single-photon Rabi frequency  $\Omega_1$  ( $\Omega_2$ ) and transition frequency  $f_1$  ( $f_2$ ) by driving separately the transitions  $|1, \pm 1\rangle \rightarrow |2, 0\rangle$  and measuring their Rabi oscillations. Since the state  $|2, 0\rangle$  suffers from very strong atom losses at a high density [56], that in our case induces decoherence in less than  $\approx 1$  ms, we performed the following measurements on a BEC that has been released from the optical trap. Starting the microwave pulse 2 ms after the release, we observe clean dynamics for the timescale

of interest. After applying the microwave pulses, a vertical magnetic gradient is turned ON for 15 ms to spatially separate the states (Stern-Gerlach) and the population in each state is counted. Since we are driving the amplifier at low power, the Rabi frequencies are the same if only one, or both tones, are present at the same time (while we observed, at full power, that the power in each tone depends on the presence of the other). By performing spectroscopies and Rabi flops, we set the frequencies and amplitudes of the DDS channels such that both transitions are (separately) on resonance with Rabi frequency of 0.76(1) kHz.

To check the validity of this calibration, we applied the two-tone pulse to different initial states  $\Psi_0$  and confronted the dynamics with the time evolution of a three-level system with Hamiltonian Eq. (3.6). Starting from  $\Psi_0 = (0, 1, 0)$  (the excited state fully populated), the time evolution is a Rabi flop between an equal population of the two ground states and the full population of the excited state (see Fig. 3.5a). We fit the experimentally observed evolution letting  $\Omega_1$ ,  $\Omega_2$ ,  $\Delta_1$  and  $\Delta_2$  as fitting parameters and obtain results consistent with the calibration above. When the initial state is  $\Psi_0 = (\frac{-1}{\sqrt{2}}, 0, \frac{1}{\sqrt{2}})$ , no population is transferred to the excited state when the two-tone microwave pulse is applied. In our experiment, we produce the mixture in the latter state using ARP, since the same microwave oscillator is used for the interferometric readout.

### 3.3 Production of MSs by phase-imprinting

Solitons in BECs can be generated by phase-imprinting a localized defect [10, 11, 45, 121, 122], or by creating inhomogeneous magnetization structures via phase-winding [123]. These solitons can also spontaneously form as a result of counter-flow instability of the superfluids [124, 125]. To deterministically create MSs, we imprinted a localized jump in the relative phase between the components of a two-component BEC. From the polarized BEC in  $|1, -1\rangle$ , produced using the protocol explained in Section 2.3, we create MSs with a two-step procedure. Typical starting conditions are a BEC of  $2 \times 10^6$  atoms, with negligible thermal component, held in a trapping potential with axial frequency 8.7(12) Hz and radial frequency 585(2) Hz, realized using the *Cigar* and the *Xaxis* beam. The Thomas-Fermi radii of the condensate are  $R_\rho = 3.7 \mu\text{m}$  and  $R_x = 250 \mu\text{m}$ , respectively along the radial and axial direction.

First, the polarized BEC must be transferred to a homogeneous non-polarized ( $Z = 0$ ) state. We achieve this with an adiabatic rapid passage (ARP) sequence, by turning on the two-photon coherent coupling with an effective Rabi frequency of 268(2) Hz at an initial detuning of  $\approx 4$  kHz. The detuning is then ramped to zero by changing the magnetic field with a half-gaussian ramp of 60 ms. At the final value of the field, the Larmor frequency is 182.3 kHz. At this magnetic field, spin-changing collisions populate the state  $|1, 0\rangle$ , destabilizing the mixture. We prevent this introducing an artificial quadratic Zeeman shift using a dressing microwave field of Rabi frequency 2.27(5) kHz, blue-detuned from the  $|1, 0\rangle \rightarrow |2, 0\rangle$  transition by 20 kHz. After the ARP sequence, the states are equally populated, the magnetization uniform and we do not observe any magnetization dynamics.

Secondly, a sharp magnetization excitation must be created without exciting the total density of the sample. We create this magnetization excitation by engineering the relative phase between the component with a vectorial optical dipole potential. In the following I will discuss the principle and calibration of this technique.

### 3.3.1 Vectorial optical dipole potential

In alkali atoms with two fine-structure transitions  $^2S_{1/2} \rightarrow ^2P_{1/2}, ^2P_{3/2}$  (D-line doublet) a monochromatic light with frequency  $\omega$  between the two transitions applies an optical potential sensitive to the magnetic quantum number  $m_F$  [104]. The potential

$$U_{dip} = \frac{\pi c^2 \Gamma}{2\omega_0^3} \left( \frac{2 + \mathcal{P} g_F m_F}{\Delta_{2,F}} + \frac{1 - \mathcal{P} g_F m_F}{\Delta_{1,F}} \right), \quad (3.9)$$

is composed of the independent contributions of the two transitions. The first (second) term in the above equation represent the contribution of the  $D_2$  ( $D_1$ ) transition, that depends on the detuning  $\Delta_{2,F}$  ( $\Delta_{1,F}$ ) of the laser from the transition itself, the spontaneous decay rate  $\Gamma$ , the (average) resonant frequency  $\omega_0$ , the Landé factor  $g_F$  and the laser polarization  $\mathcal{P}$  ( $\mathcal{P} = \pm 1$  for circular and  $\mathcal{P} = 0$  for linear polarization). From this equation it is clear that we can apply different potentials to the  $|1, \pm 1\rangle$  states thanks to their opposite  $m_F$ . Since the phase of the order parameter evolves as  $e^{-iEt/\hbar}$ , with  $E$  the energy of the component, if the potential is different at different points it causes the accumulation of a phase difference. This *phase imprinting* (PI) procedure can imprint an arbitrary phase on the condensate applying a spatially inhomogeneous optical potential.

To produce a MS, the imprinted (relative) phase profile must be a sharp jump of  $\pi$ . However, also the densities of both components should be changed according to Eq. (3.2), as was recently reported in [126]. We chose, instead, to imprint a total jump in relative phase of  $2\pi$ , corresponding to two opposite phase jumps of  $\pm\pi$  in the components and no change in total phase. This phase profile corresponds to two overlapped MSs with opposite magnetization and velocity, and their total magnetization is zero everywhere. In this way the total magnetization of the sample is conserved and a single phase-imprint produces a couple of opposite MSs. By setting the wavelength of a circularly polarized light such as  $\Delta_2 = 2\Delta_1$  the potential is purely vectorial, it has equal magnitude but opposite sign for the states  $|1, + - 1\rangle$ . For the D-line of  $^{23}\text{Na}$ , this condition is satisfied at wavelength of 589.557 nm.

Furthermore, we require the phase imprinting to be much shorter than the time of the spin dynamics of the sample, to avoid evolution of the condensate in an inhomogeneous spin potential. We estimate that the duration of the PI should be much smaller than  $\hbar/n\delta g \approx 2$  ms.

### Laser and optical system

We realized an ECDL laser at 1179.114 nm that is then amplified by a slave laser to produce 200 mW of light power. The infrared light is then frequency doubled using a PPLN waveguide chip (HC Photonics [127]) producing  $\approx 12$  mW of 598 nm light. The

light is deflected by a single-pass 80 MHz AOM acting as a fast optical switch, before being coupled in a polarization-maintaining optical fibre (Schäfter Kirchhoff PMC-630-4-2) to be transferred to the sample. At the output of the fibre we obtain 7 mW of usable power. In order to increase the light intensity and shorten the pulse time, the beam on the sample is elliptical, with a 4:1 ratio between the waists. We achieve this using a 4:1 telescope with cylindrical lenses of focal length  $-50$  mm (Thorlabs LK1662L1-A) and  $200$  mm (Thorlabs LJ1653L1-A). The collimated beam is then superimposed to our vertical imaging path using a PBS and relayed with a demagnification of 6 on the atoms by the imaging lenses (see Section 2.2.9). The beam waists on the atoms are  $\approx 170$   $\mu\text{m}$  and  $\approx 660$   $\mu\text{m}$ , with the larger waist along to the long axis of the BEC. This beam is then masked by a movable knife edge placed on the imaging plane of the imaging system, to obtain a sharp step-like intensity pattern on the sample, so that half of the BEC is not illuminated and the other half is approximatively uniformly illuminated. The sharpness of the transition from brightness to dark is equal to the imaging resolution on this axis, that is estimated by geometrical optics simulations to be  $\approx 1.8$   $\mu\text{m}$ .

### 3.3.2 Calibration of the phase imprint pulse

The amount of accumulated relative phase when the optical potential is applied depends both on the light intensity and on the pulse duration. We characterize the amount of imprinted phase by light pulses of various durations using our interferometric technique, as a routine calibration of our experiment. We create a mixture with uniform relative phase, apply the PI and at the shortest delay possible (2 ms) we take an interferometric picture. After this short time the evolution of relative phase is negligible, and we can measure the phase profile from which the evolution of the system starts.

By controllably applying a phase-shift on one of the arms of the interferometer (varying the phase of the microwave local oscillator  $\phi_{LO}$ ), we observe the output of the interferometer to oscillate sinusoidally with a contrast of  $\approx 90\%$ . We sample the total output of the interferometer in a region of  $10 \times 8$  px illuminated (not illuminated) by the phase-imprint light (see Fig. 3.6a), and fit a sinusoid to extract the global phase in Fig. 3.6b. The difference  $\Delta\phi$  between the two extracted phases is then a direct measure of the amount of relative phase that the PI has imprinted, and is linearly proportional to the pulse duration. The pulse duration necessary to imprint a jump of  $2\pi$  is then extracted with a linear fit (Fig. 3.6c). In our system, for the beam waists of  $\approx 170$   $\mu\text{m}$  and  $\approx 660$   $\mu\text{m}$  and total power of 5.2 mW, the time for a phase imprint of  $2\pi$  is 89.1  $\mu\text{s}$ , of the same order of the value expected from Eq. (3.9).

### Short-time MS dynamics

Using the reconstruction method described in the previous Sections, we fully characterize the MSs that are produced in the sample by the phase imprint technique.

We phase imprint a  $2\pi$  step in the relative phase and after a variable evolution time, we take an image of the density for each state and an interferometric readout of the relative phase. Examples of these images are shown in Fig. 3.7. We observe that after



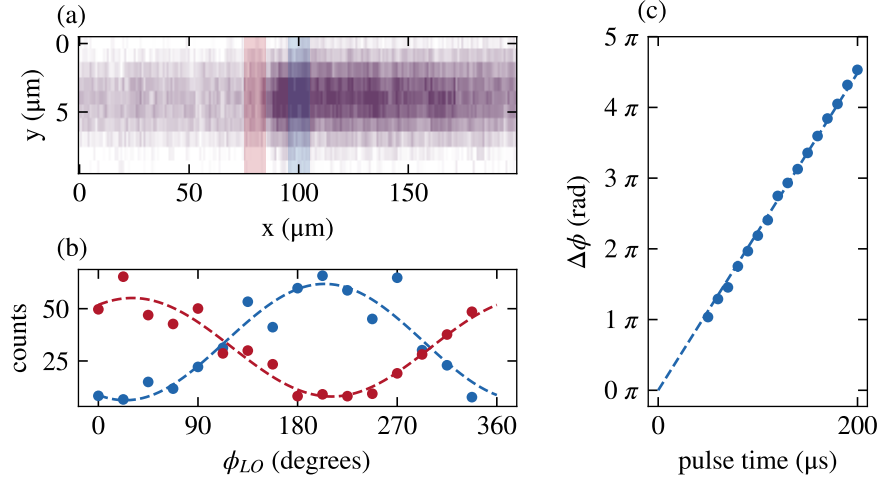


Figure 3.6: (a) Image from the interferometer right after the phase imprint pulse. Shaded areas show the regions used to extract the relative phase. (b) Scan of the phase of the local oscillator to measure the jump in relative phase between the dark (red) and illuminated (blue) halves of the BEC. (c) Measured phase jump as function of the duration of the light pulse. Multiples of  $2\pi$  have been added to the observed phase jump to make the data continuous. Error bars are smaller than points size.

phase imprint, two MSs are created, each one being a density bump in one component and a density dip in the other. The solitons can be more easily observed in the magnetization of the condensate, while the total density is only minimally excited. The produced MSs have opposite sign and travel in opposite directions. In correspondence of the MS, the interferometer readout shows a sharp jump, indicating that the excitation is connected to a change in relative phase.

### MS identification

In order to study the dynamics of the MSs, we required a method to identify their position from the acquired optical densities (Fig. 3.8a). The ODs are integrated along the  $y$ -axis to get a one-dimensional profile  $n_{\pm 1}(x)$  of the density of each component along the axis  $x$ . In the densities, MSs appear as sharp and narrow peaks or dips, see Fig. 3.8b. From these profiles we calculate the 1D magnetization of our sample  $Z(x) = \frac{n_{+1} - n_{-1}}{n_{+1} + n_{-1}}$ . In this way the inhomogeneous total density profile of the BEC is eliminated and the signal-to-noise ratio increased. However, we often observe the presence of long-wavelength magnetization excitations in the BEC, that are produced by unknown sources, presumably due to the low energy necessary for their excitation. We found convenient to apply a digital high-pass filter on the calculated 1D magnetization profile before prosecuting with the MSs identification, in order to remove excitations of wavelength  $>125 \mu\text{m}$ . The resulting magnetization profile is flat, with MSs appearing as



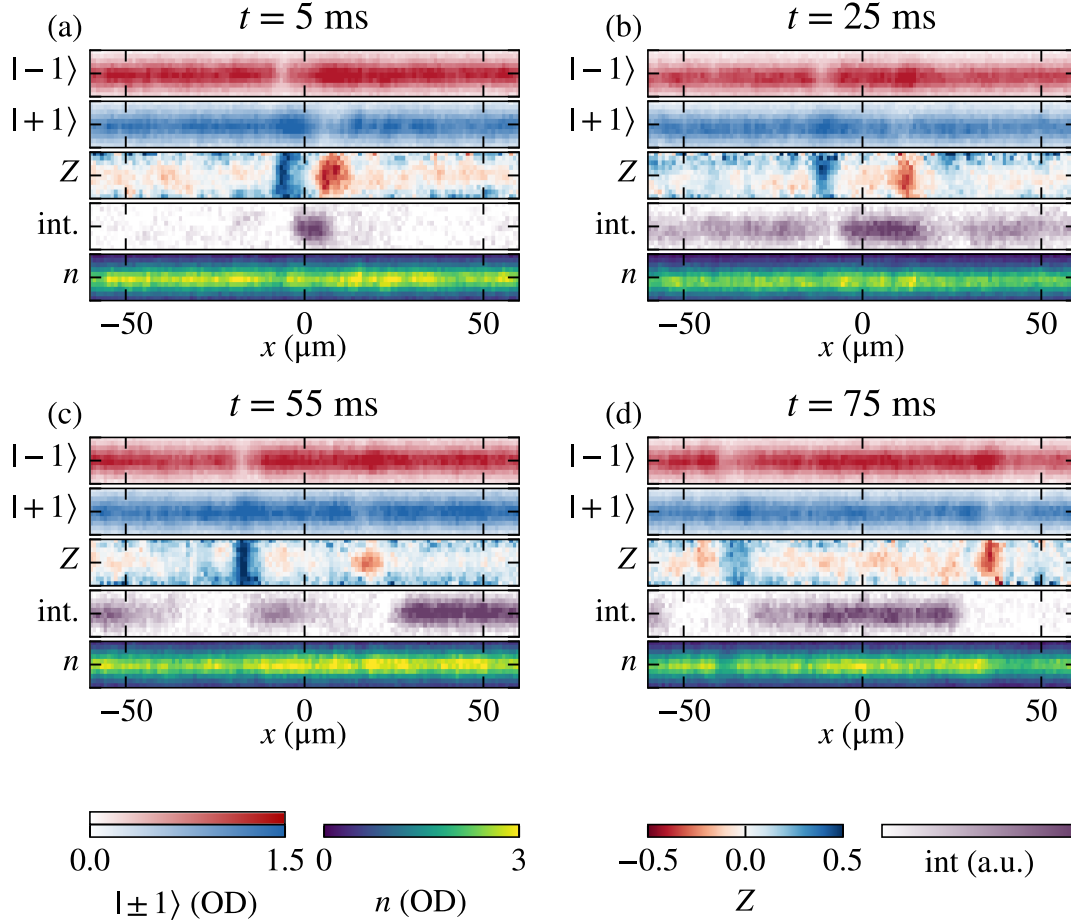


Figure 3.7: MSs at different time  $t$  after their creation. Each set of images has been acquired in a single experimental run. From top to bottom, each set is composed of the atomic densities in  $|1, -1\rangle$  and  $|1, +1\rangle$ , where MSs are visible as density bumps and dips. From these images we compute the magnetization  $Z$  of the sample. Then, the readout of the interferometer, showing changes in the relative phase corresponding to the position of MSs. The total density  $n$  of the sample, shows no excitation in correspondence of the MSs.

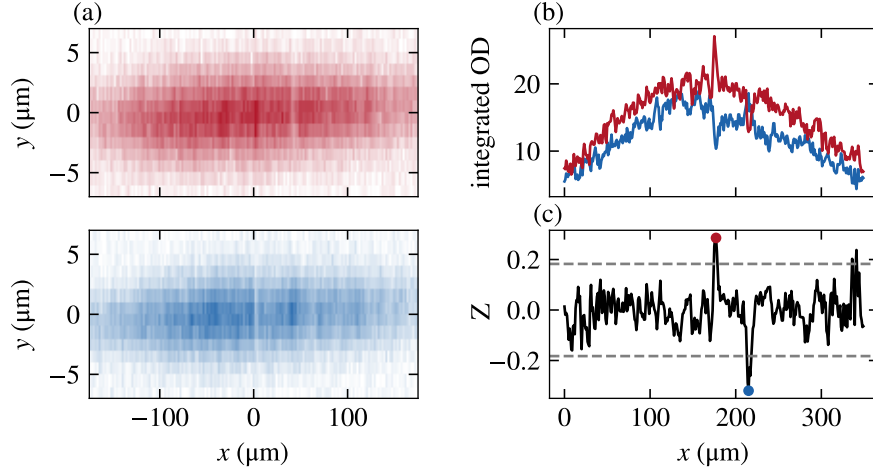


Figure 3.8: (a) OD of the states  $m_F = -1$  (top) and  $m_F = +1$  (bottom) obtained using PTAL. (b) integrated 1D density profiles for the two states. (c) filtered magnetization profile used for MSs identification, with the positions of the solitons indicated by dots. The horizontal dashed lines are the threshold used for MS identification.

small localized excitations (see Fig. 3.8c). The identification of the position of the MSs is performed with a peak-finding algorithm (available as `scipy.signal.find_peaks` in [128]). All the local maxima in the magnetization are found by comparison with the neighbouring points. Of these maxima, we select the ones that are higher (lower) from the mean value of the magnetization by a given threshold. The value of this threshold is empirically chosen to identify as many solitons as possible with the minimum amount of false positives. Once that the position of the solitons in the sample has been determined, we can study their dynamics.

A note has to be made on the fact that the magnetization that we reconstruct from these images does not correspond to the true magnetization of the soliton due to the limited resolution of the imaging system. In fact, the size of a soliton (of the order of  $\xi_s \approx 0.8 \mu\text{m}$ ) is larger than our imaging resolution of  $1.8 \mu\text{m}$ , and we expect the real magnetization to be higher than the observed one.

### Relative-phase jump measurement

To study the relative-phase profile of the MSs, we produce a couple of MSs and we leave the solitons evolve for 30 ms, such that they are spatially separated, then perform the full tomographic imaging. From the magnetization of the sample, we identify in each shot the position of the solitons and observe the OD of the readout state of the interferometer (see Fig. 3.9a). At the position of the MSs, the OD changes abruptly, with variable contrast from shot to shot. We impute this to random changes of the global phase, as it changes the visibility of the relative phase jump (confront with Fig. 3.6b at

$\phi_{LO} = 90^\circ$ ). Moreover, we observe that even in the absence of the phase-imprint pulse, non-uniform excitations of the relative phase develops after some tens of milliseconds. These excitations have much longer wavelength than the size of the solitons and are expected not to influence the dynamics of the solitons that is much more energetic. In the presence of these excitations, the jump of relative phase can be measured only locally in the regions nearby the soliton and not globally in the bulk of the condensate.

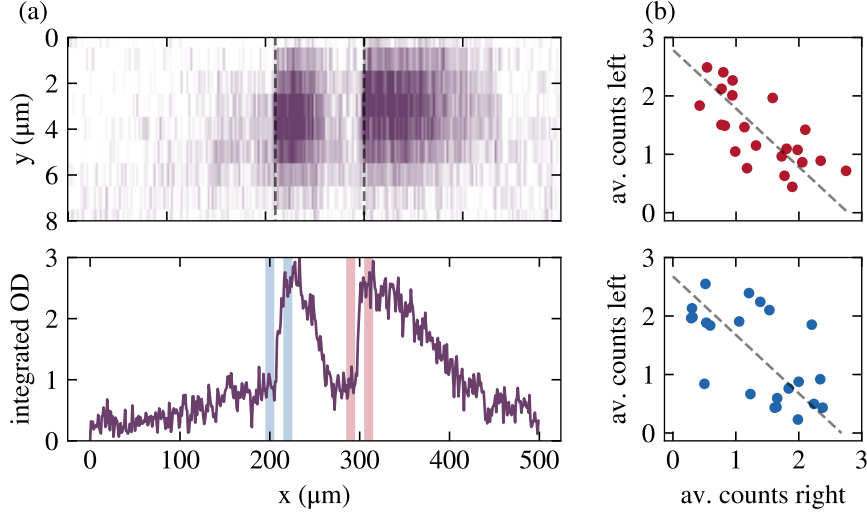


Figure 3.9: (a) Example OD in the readout state  $|2,0\rangle$ , with the MSs positions determined from the magnetization of the sample (dashed lines). (b) Integrated OD along the  $y$  axis, showing the sharp jump in relative phase at the position of the solitons. To measure the phase jump across the solitons, we compare the average counts in the shaded regions. (c) Average counts in the left versus right regions, for each MS. Each point is an experimental repetition. While the global phase changes from shot to shot, the counts in the two regions are anti-correlated, showing that a jump of  $\pi$  in the relative phase is happening across the soliton.

To measure the jump in relative phase, we restricted our analysis to two regions of the  $x$ -axis of  $10\text{ }\mu\text{m}$ , at a distance of  $\pm 10\text{ }\mu\text{m}$  from the centre of each soliton. In the lower panel of Fig. 3.9a, the regions used to probe the relative phase are highlighted as red and blue overlays for, respectively, the negative and positive magnetization solitons. Probing the relative phase on a small region rejects much of the noise coming from long-wavelength excitations.

Finally, we circumvent the random changes in global phase looking at the correlation of the interferometer readings on the two sides of the soliton. Assuming that the interferometer readings on one side of the soliton is  $\approx \cos(\phi)$ , a jump of relative phase equal to  $\pi$  means that the readings on the other sides will be  $\approx \cos(\phi + \pi) = -\cos(\phi)$ . Thus, a perfect anti-correlation between the two sides allows to infer that the relative phase jump across the soliton is indeed  $\pi$ . In order to increase the contrast of the anti-correlation we

scan the phase  $\phi_{LO}$ . In Fig. 3.9b, the counts in each region on the opposite sides of the soliton are plotted one versus the other. The counts are strongly anti-correlated (ideal anti-correlation is represented by the dashed line), compatibly with experimental noise, showing that the jump of relative phase is indeed  $\pi$  across the soliton.

### 3.4 In trap dynamics

In a trapped gas, the MSs are expected to oscillate in the sample following Eqs. 3.4 - 3.5). Here, we created couples of MSs by phase-imprint and, after different evolution times, we imaged them with the full tomographic imaging. Since the production of the soliton is deterministic, we therefore study the full dynamics of the soliton in the trap.

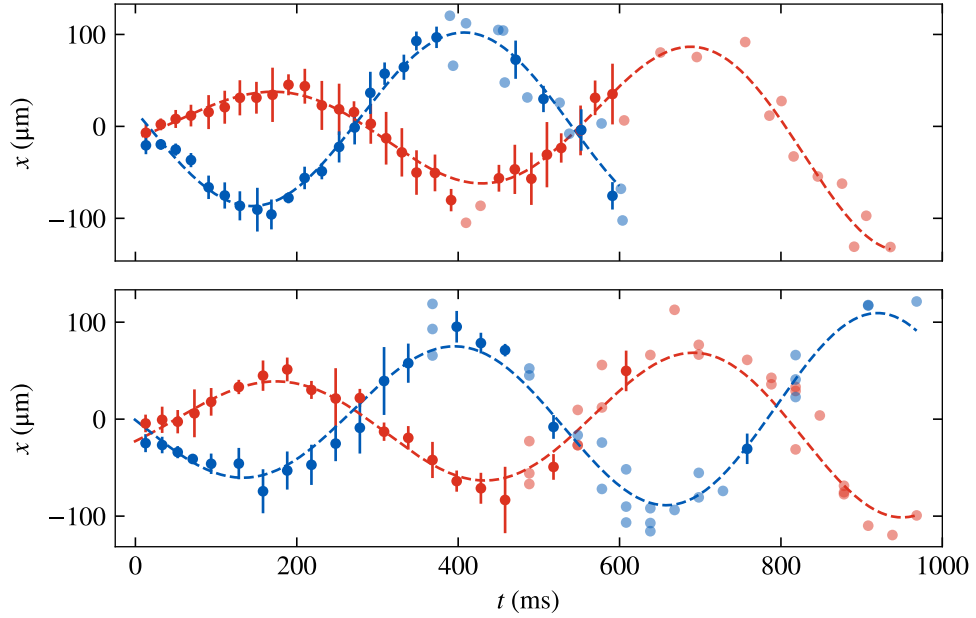


Figure 3.10: Position of the MSs after a time  $t$  after the phase-imprint pulse. Points and errorbars are, respectively, mean and standard deviation of at least 4 experimental realizations in time bins of 25 ms. Single experimental realizations are represented with lighter points. The two plots are different data runs taken on different days with 2.2 millions (top) and 1.1 millions (bottom) atoms in the sample. We extract the amplitude and period of the oscillation fitting Eq. (3.10) to the single points (dashed lines).

We observe a residual sloshing of the BEC  $x$  position of  $\pm 30 \mu\text{m}$ , that changes the position at which we imprint along the cloud. We measure the position of the cloud using *shadowgraph imaging* [129], i.e. taking an off-resonant image of the BEC,  $\approx 5$  ms before the phase-imprint pulse. The shots where the centre of the cloud and the phase-imprint position are displaced by more than  $10 \mu\text{m}$  have been discarded in post-processing. We

checked that the phase-imprint light does not move along  $\hat{x}$ . In the following, the position of the soliton is expressed with respect to the centre-of-mass of the BEC.

The dynamics of the solitons has been observed for an evolution time  $t$  as long as 1 s after their creation, before their height decays below the detection threshold. In Fig. 3.10 the dynamics of two pairs of solitons is represented, where each red (blue) point corresponds to the position  $x(t)$  of the negative (positive) magnetization soliton identified with the full-tomographic imaging. The dynamics of MSs in the trap is not a harmonic oscillation, with this effect more evident for solitons with velocity  $\approx c_s$ , however, the solitons we were able to produce never reached such high velocities. In the experiment, instead, we observe that the amplitude of the MS oscillation is slowly increasing in time. This effect is probably caused by particle loss in the soliton due to the finite temperature of the sample, lowering its magnetization and increasing the amplitude of the oscillation. We have not investigated this effect further, due to the lack of theoretical works to support the claim, and we empirically fit the motion of the solitons using a sinusoid with exponentially increasing amplitude

$$y(t) = Le^{t/\tau} \sin(2\pi t/T + \phi). \quad (3.10)$$

Since the spin-sound velocity  $c_s$  in the sample can be obtained from independent measurements of atom number and trapping frequencies, we can directly compare the dynamics of the solitons with the theoretical prediction. Varying the total atom number and the focusing of the phase-imprint blade we launched MSs with different initial velocities in samples of different densities. For each dataset, we measure the oscillation amplitude  $L$  and period  $T$ . In Fig. 3.11a we compare the observed period of the oscillation with Eq. (3.5). The observed oscillation period is in agreement, compatibly with experimental noise, with the theoretical prediction of  $\approx 4.5T_z$ . The large uncertainty in determining the period, however, does not permit to observe an increase of oscillation period for high initial velocities. This uncertainty is due to the limited number of oscillations that the solitons perform and the scattering in the position of the solitons. In Fig. 3.11b, the oscillation amplitude is plotted against initial velocity showing substantial agreement with the theoretical prediction.

## 3.5 Evolution and decay of the MS

### 3.5.1 MS width

The characteristic feature of solitonic waves is their propagation without dispersion, so that they retain a constant shape after any propagation time. In the specific case of MSs, the peak magnetization ( $Z_0$ ) and the width of the soliton are dependent on the soliton velocity, and so will vary during the oscillatory motion as the velocity is changing.

To further confirm that the observed excitations have solitonic nature, we measure the width of the soliton for different evolution times from the in-situ magnetization of the sample. Due to the low signal-to-noise ratio of the magnetization, we average the magnetization profile from many experimental realizations with the following procedure.

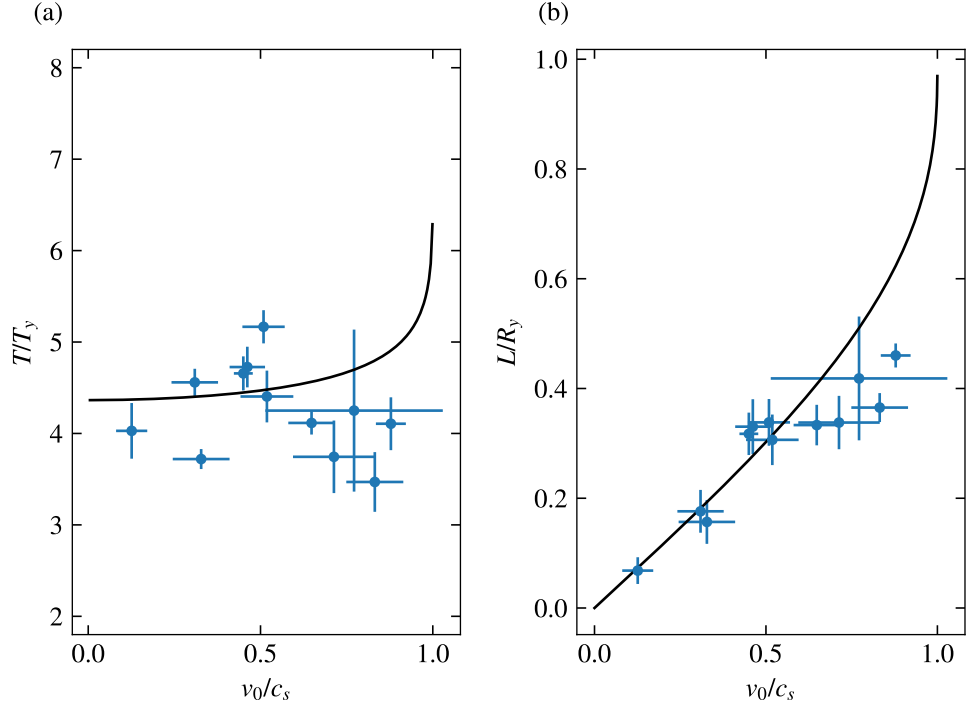


Figure 3.11: (a) Measured MS period (dots) and prediction (line) from Eq. 3.5. (b) Measured MS turning point (dots) and prediction from Eq. 3.4 (line). Theoretical predictions have no free parameters. Errorbars are 68% confidence intervals from the fitting routine.

After identifying the solitons, the magnetization of a 40 pixels-wide region, centred on the soliton, is extracted. The realizations are binned for similar values of  $t$  and averaged. In Fig. 3.12(a,c) we show the average magnetization profile (points) of solitons of positive (blue) and negative (red) magnetization. On this profile a Gaussian curve is fitted (black solid line) to extract the width and amplitude of the solitons. The expected magnetization profile calculated from the spin-healing length and the soliton velocity (dashed coloured line) is narrower and reaches a peak magnetization of  $\approx \pm 0.8$ . The discrepancy between the observed and expected magnetization profiles can mostly be explained taking into account the finite imaging resolution (black dashed line), hence we can only give an upper bound to the width of the solitons. We do not observe a change in the width and amplitude of the solitons during the dynamics, see Fig. 3.12(b, d). It must be noted that during this evolution time the solitons have crossed each-other twice, after 250 ms and after 500 ms and no change in width or amplitude after the crossing is observed. Soliton-soliton collisions will be better analysed in the following Sections.

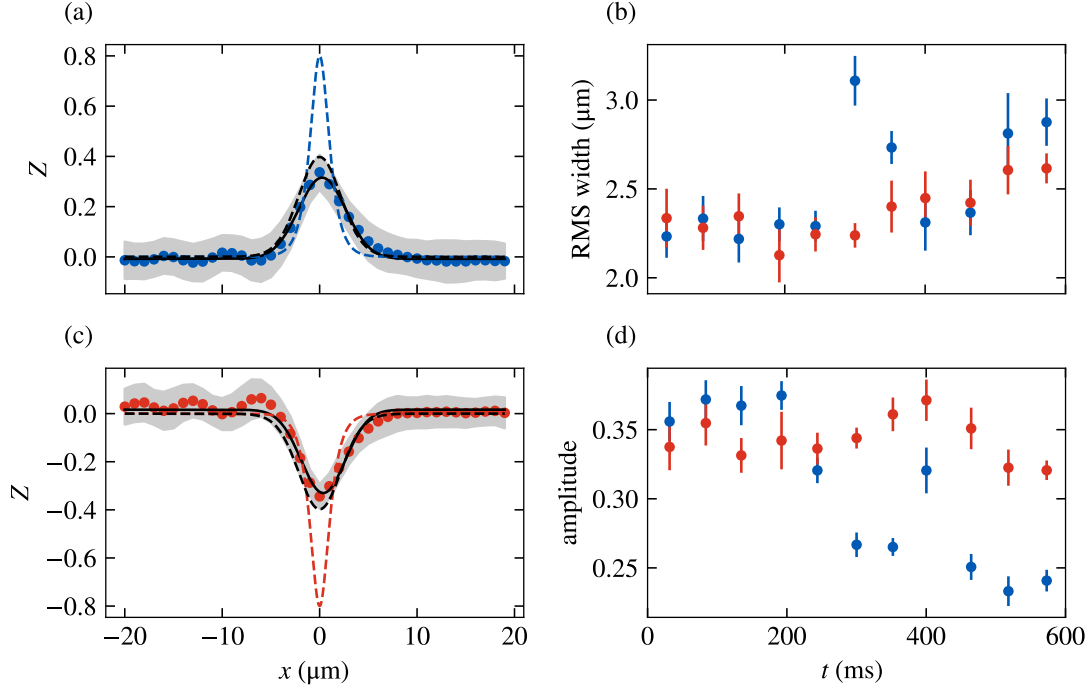


Figure 3.12: Average magnetization profile of a soliton of positive (a) and negative (c) magnetization, for evolution time of 150 ms. The experimentally observed profile (points) is fitted with a Gaussian function (black, solid). From the spin-healing length of the sample and the velocity of the solitons, we calculate the expected magnetization profile (coloured, dashed) and we simulate the blurring effect of the imaging resolution on such profile (black, dashed). Evolution of the observed RMS width (b) and amplitude (d) of the solitons as function of the evolution time.

### 3.5.2 MS decay

Solitons with negative effective mass are stable only in one-dimensional systems. In higher dimensions they decay due to “snake instability” [112, 47], due to the non-negligible transverse size that allows the growth of transverse excitations. Other excitations are produced in the decay, such as solitonic vortices and vortex rings [130, 131, 132, 133]. The parameter that determines the stability of solitons in an elongated system is the ratio between the radial size of the condensate  $R_\rho$  and the size of the soliton  $\xi_s$ . In our system, this ratio is approximatively 5.

To check that the excitations that we produce are indeed MS and do not decay into other excitations, we change from in-situ imaging to time-of-flight, leaving the sample to expand ballistically for 30 ms in a levitating magnetic gradient. Due to the different magnetic moment of the components, only the  $|1, -1\rangle$  is levitated. In Fig. 3.13 we show two example images taken after expansion. At short and long times after the creation of

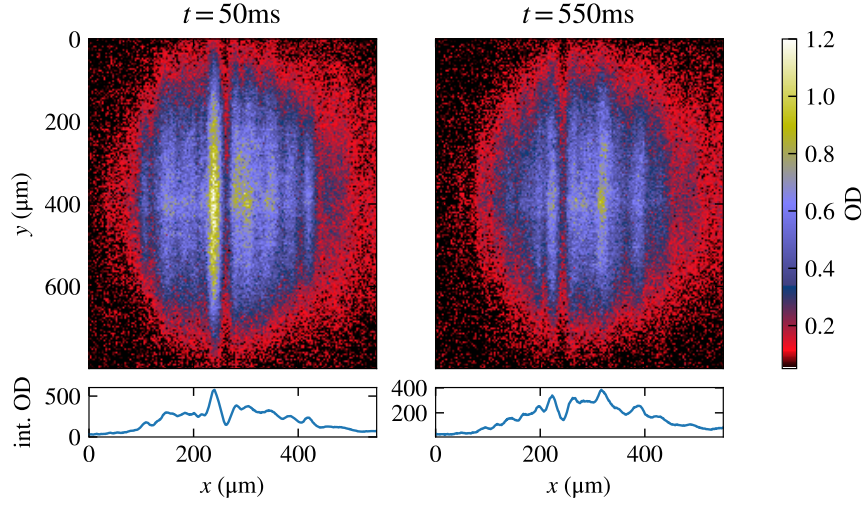


Figure 3.13: (left) OD of  $|1, -1\rangle$  after 30 ms of free expansion and evolution time of 50 ms. The density bump (dip) caused by a negative (positive) magnetization soliton is visible near the centre of the cloud, as a straight fringe. (right) At the longer evolution time of 550 ms, the solitons are less clearly visible, however we do not observe bending of the soliton. The bottom plots show the OD integrated along the  $y$  axis.

the solitons, they are visible even in a single component as density bumps and dips, that show a straight profile and no bending or tilting due to transverse excitations arising from snake instability. In particular, we do not observe the characteristic “S” figure of an expanding solitonic vortex [134].

## 3.6 Collisions

The propagation of solitons is rigorously dispersion-less only when a single soliton is propagating in a uniform background. In this Section, we experimentally investigate collisions between same- and opposite-magnetization solitons.

### 3.6.1 Opposite magnetization collisions

The collision of solitons of opposite magnetization happens naturally in our system since we produce couples of solitons moving in opposite directions. Each soliton performs then an oscillatory motion in the trap until it comes back to the centre and collides with its pair of opposite magnetization.

From the measurements of in-trap dynamics of Section 3.4 we already observed that the solitons survive multiple collisions with no apparent change. To better study this collision, we produced couples of MSs with initial velocity  $\pm 0.6c_s$  and concentrate on the first collision that happens approximately at  $t = 300$  ms. After performing half



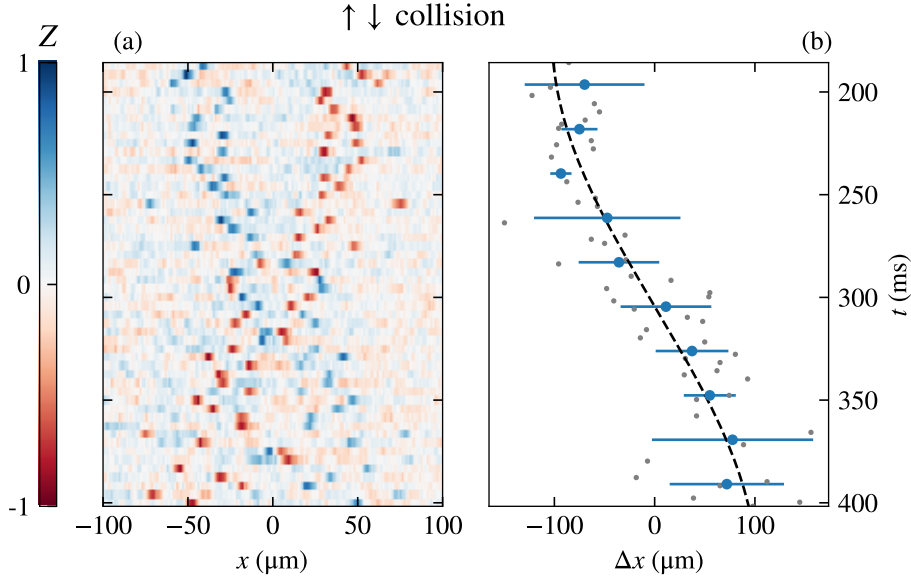


Figure 3.14: (a) Magnetization of the sample during the collision of solitons of opposite magnetization. Each row is an experimental realization. (b) Distance between colliding solitons (grey points). The same data is binned in intervals of 20 ms (blue points and errorbars). The solitons cross each other and their relative motion is compatible with in-trap oscillation without interaction (dashed line).

an oscillation, the two solitons cross each other at the centre of the trap, apparently unchanged (see Fig. 3.14a). To reduce the scatter in the position of the solitons, we shift their average position to the centre. For this data set, only the shots where two solitons have been clearly identified have been considered, to remove shots where one of the solitons did not survive and the collision is not happening.

In Fig. 3.14b, we extracted the distance between the solitons ( $\Delta x$ ). Since each soliton is moving of oscillatory motion the distance between the two solitons will describe, approximatively, a sinusoid, hence we fit an arc of sinusoid on the data, with fixed period according to the in-trap dynamics observed in Section 3.4. The large scatter in the positions of the solitons prevents to investigate precisely the collision process, and a more detailed investigation is required to experimentally highlight effect of interaction between solitons. However, since we do not observe a discontinuity at the collision the hypothesis of dissipation-less collision is compatible with the data.

### 3.6.2 Same magnetization collisions

To produce collisions between solitons of same magnetization, the phase-imprint beam has been modified changing the intensity mask to create a uniformly illuminated central region and dark lateral regions. The resulting imprinted phase profile consists of two

opposite steps in the relative phase, at a distance of  $\approx 100 \mu\text{m}$  and centred on the BEC. Each phase step will then generate a couple of MSs, with the solitons of positive (negative) magnetization travelling inward (outward). The solitons of positive magnetization thus collide at the centre of the trap, 50 ms after their creation (see Fig. 3.15a). This experimental condition has the advantage that the collision happens after a much shorter time from the phase imprint than in the previous Section, reducing the scatter in the position of the solitons. To further reduce the scatter, we set the average position of the colliding solitons to the centre.

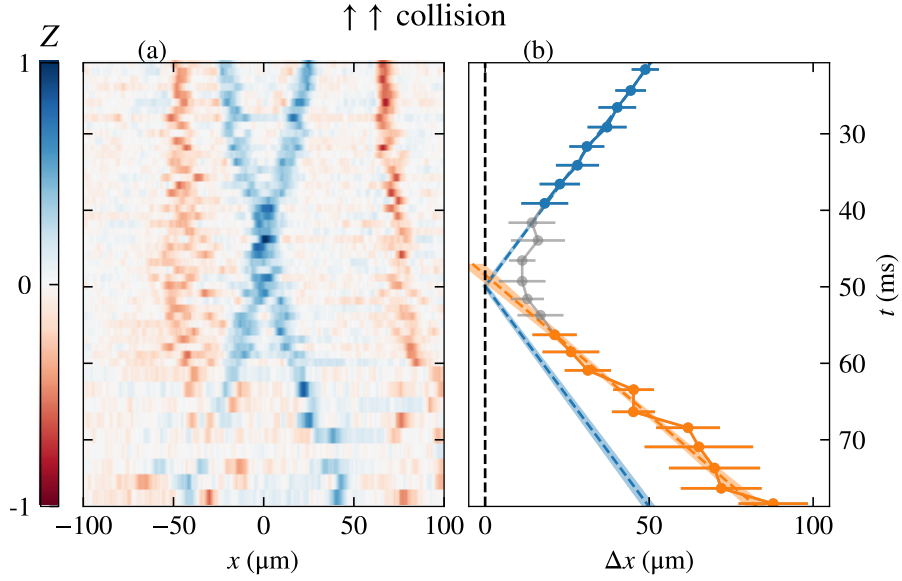


Figure 3.15: (a) Magnetization of the sample during the collision of solitons of equal magnetization. Each row is the average of up to five experimental realizations. (b) Distance  $\Delta x$  between colliding solitons. Their relative motion is linear before (blue) and after (orange) the collision, since the motion happens near the center of the trap. Between 40 and 55 ms the solitons can not be distinguished (gray). Dashed lines are linear fits to  $\Delta x$ , showing an increase of velocity after the collision. The motion before the collision is extended to compare with dissipation-less behaviour. Dashed regions are one-standard-deviation confidence intervals.

In Fig. 3.15b we plot the distance between the two solitons. Differently from the previous Section, we can not clearly identify the solitons due to the equal magnetization. Consequentially, between 40 and 55 ms the two solitons can not be distinguished as the scattering in their position exceeds their (mean) relative distance. For other times we can safely assume that the collision is already happened, or not happened yet. We measure the relative velocity of the solitons before and after the collision using linear fitting. We observed the two velocities to be statistically significant with values  $1.83(8) \text{ mm/s}$  before the collision and  $2.8(1) \text{ mm/s}$  after. Since the solitons are colliding near the centre of

the trap, their motion is linear to a good approximation, hence we can not explain the discontinuity in the velocity with the trajectory inside the trap.

We explain this dissipative behaviour, in contrast with the expected dissipationless nature of the solitons, considering that the total magnetization of the overlapped solitons would exceed unity, an unphysical condition. As the simulations of Section 3.1.1 show, during same-magnetization collisions the solitons do not cross, but rather rapidly interact one with the other. This interaction may introduce a dissipation effect, due to the strong perturbation that the solitons experience. This dissipation may be possibly caused by the three-dimensionality of the system, since this effect is not present in 1D simulations.



# Chapter 4

## Spin quantum torque in magnetic heterostructures in cold gases

Layered structures of materials with different magnetic properties, the so-called *magnetic heterostructures* [135], are of particular interest in the field of material science. New physical phenomena originate at the interface between these materials, such as exchange coupling, giant magneto-resistance and spin torque [136]. These effects found many technological applications even in common devices such as magnetic tape recorders and hard drives. In Section 1.3.4, I introduced how the Gross-Pitaevskii equations of a two-component Bose gas can be recast in the form of a dissipationless Landau-Lifshitz equation, the governing equation of the magnetization dynamics in materials. Ultracold Bose gases can therefore become a simulation platform for micro-magnetic phenomena due to the high degree of control available in such systems.

So far this parallelism has been studied in Bose gases neglecting the spatial degree of freedom, where the LLE reduces to the Josephson equation, both in double-well [74] and in internally-coupled systems [60]. To create analogues of magnetic heterostructures, however, the system must be extended in at least one spatial dimension. Elongated Josephson systems in Bose gases [78, 80, 79, 82] have been studied both theoretically and experimentally in double-well systems, however the realization of analogues to magnetic heterostructures is still missing.

In this Chapter, I present the experimental realization of a one-dimensional internal Josephson junction using a coherently-coupled two-component  $^{23}\text{Na}$  BEC with a large aspect ratio. In this system, the spatially-dependent atomic density naturally creates regions with different magnetic properties. At the interface of these regions a domain wall is formed, that then decays into magnetic excitations because of spin quantum-torque. The first Section is devoted to the characterization of the system dimensionality in relation to the spin dynamics, to the state preparation and to the measurement of the relevant quantities governing the dynamics of the sample. The second Section presents the experimental investigation of the creation and breaking of magnetic domain walls.

## 4.1 Manipulation of an elongated JJ

In Section 1.3.1, I introduced how the Josephson equation describes the evolution of the internal states of a Bose gas with its dependence on the atomic density and the Rabi frequency. In our experimental system, the Rabi frequency is (to a good approximation) uniform, while the density is inhomogeneous due to the harmonic trapping potential. For a system with non-uniform density, we can consider two extreme cases. In the first, the system is very large and the density changes so slowly in space that the atoms do not move significantly during a Rabi period. Consequently, each atom evolves with Josephson dynamics depending on the (local) value of the density and distant parts of the system do not influence each other. Then, since each part of the system has a different dynamics, the spin of the sample becomes inhomogeneous while the total density remains constant. In the second case the system is very small and, due to atomic motion, its spin averages much faster than a Rabi period in every part of the system. Consequently, the spin dynamics of the system is homogeneous and evolves following the Josephson equation, with an “average” atomic density. In other words, the first example shows a purely local Josephson dynamics while the second is a single (spatial) mode approximation of the system. In between the two limits, the local Josephson dynamics and the movement of the spins will influence each other.

In a strongly elongated system, whose size along one direction is much larger than along the other two, the first limit might hold along the long direction, while the second limit holds along the other two. In this system, the spin dynamics is purely one-dimensional and, along the long axis, strictly local. The system therefore is analogous to an elongated Josephson junction. In this Section, I report on the realization of an experimental system with effectively 1D spin dynamics. On this system, common techniques for internal state preparation require revisiting, as the parameters of the local Josephson dynamics depends on the inhomogeneous density profile.

### 4.1.1 Realization of 1D spin dynamics

We experimentally investigate for what parameters our system shows one-dimensional spin dynamics, by changing the aspect ratio of our sample at fixed peak density  $n_0$ . As anticipated in Section 1.3.4, we expect the system to be one-dimensional as long as the radial size is smaller than the dimension of spin-excitations. In the Thomas-Fermi approximation,  $n(\mathbf{r}) = n_0(1 - \frac{x^2}{R_x^2} - \frac{\rho^2}{R_\rho^2})$ , with  $x$  and  $\rho$  respectively the axial and transverse direction of the system, the radial size is given by the Thomas-Fermi radius  $R_\rho$ . We consider that spin excitations have a characteristic length scale given by  $\xi_s$ , calculated at the center of the sample. The ratio  $R_\rho/\xi_s$  depends on the choice of the radial trapping frequency  $\omega_\rho$  and on the peak density as

$$\frac{R_\rho}{\xi_s} = \frac{2n_0g}{\hbar\omega_\rho} \sqrt{\frac{\delta g}{g}}. \quad (4.1)$$

In our experimental setup we can vary this ratio approximately between 1 and 5.

To verify that the spin-dynamics can be approximated as one-dimensional, we try to create spin excitations along the transverse direction. To do so, we leverage the fact that for different densities the spin can be in different dynamical regions of the Josephson equation (Section 1.3.2). Let us consider only the transverse cut at  $x = 0$  of the sample, where the density is  $n_0$  at the center and vanishes at  $R_\rho$ . Starting from a fully polarized system in  $|1, -1\rangle = |\downarrow\rangle$  and suddenly applying a resonant Rabi coupling with  $|1, +1\rangle = |\uparrow\rangle$ , the spin can be either in the Rabi oscillating regime or in the self-trapped regime. Choosing a coupling strength  $\Omega < \frac{n_0 \delta g}{2\hbar}$ , we then expect the center of the cloud to be self-trapped. If the transverse size is large, the center of the cloud remains self-trapped, while the local spin performs Rabi oscillations at some value of  $\rho$ , creating transverse excitations. If the transverse size is small, instead, the spin remains self-trapped at all values of  $\rho$ , since all the atoms evolve with the average value of non-linear coupling strength  $\kappa$  (actually, the condition of self-trapping is more stringent, cf. Section 1.3.4). We test if the system has one-dimensional spin dynamics by applying the coupling for a time corresponding to a  $\pi$ -pulse for a single  $|\downarrow\rangle$  atom. After the pulse, there is no population transferred to  $|\uparrow\rangle$  only in the case of one-dimensional dynamics.

### Trap compression

In order to vary the ratio  $R_\rho/\xi_s$ , we modify the preparation of the condensed sample described in Section 2.3. After the loading of the Hybrid Trap with a thermal cloud, we apply a high-stability magnetic field  $B = 1.3$  G along  $z$ . Then, we transfer the cloud to a purely optical trap formed crossing the Cigar (waist  $18\ \mu\text{m}$ , power  $800\ \text{mW}$ ) and the Xaxis beam (vertical waist  $72\ \mu\text{m}$ , horizontal waist  $700\ \mu\text{m}$ , power  $1\ \text{W}$ ), then remove the magnetic quadrupole. We perform evaporative cooling ramping down the power of the Cigar beam with a 1-s-long exponential ramp, down to a final value of  $\approx 50\ \text{mW}$ . We adjust this final value to set the sample temperature. To change the radial trapping frequency, we then compress the optical trap by adiabatically increasing its power with a 1-s-long half-Gaussian ramp. By compressing the trap, we tune the radial trapping frequency  $\omega_\rho/2\pi$  at values from  $500\ \text{Hz}$  to  $1000\ \text{Hz}$ , while keeping fixed the axial trapping frequency  $\omega_x/2\pi$  at  $10(2)\ \text{Hz}$ .

### Determination of coupling parameters

In the following Sections, we investigate the role of the non-linear coupling strength in the internal dynamics of the system that also depends on the Rabi frequency  $\Omega$  and detuning  $\delta$ . In the measurements presented in this Chapter, we apply the two-photon coupling using the “hook-side” antenna (cf. Section 2.2.6). We stabilize the mixture with an artificial quadratic Zeeman shift using a microwave field radiated from the “hook-vert” antenna blue-detuned with respect to the  $|1, 0\rangle \rightarrow |2, 0\rangle$  transition.

We measure independently  $\Omega$  and  $\delta$  on a very dilute thermal cloud, held in the same optical trap. To produce a thermal cloud instead of a BEC, we lower the power in the Cigar beam during the loading of the Hybrid Trap, to drastically reduce the number of atoms transferred in the optical trap prior to the evaporation ramp. No other

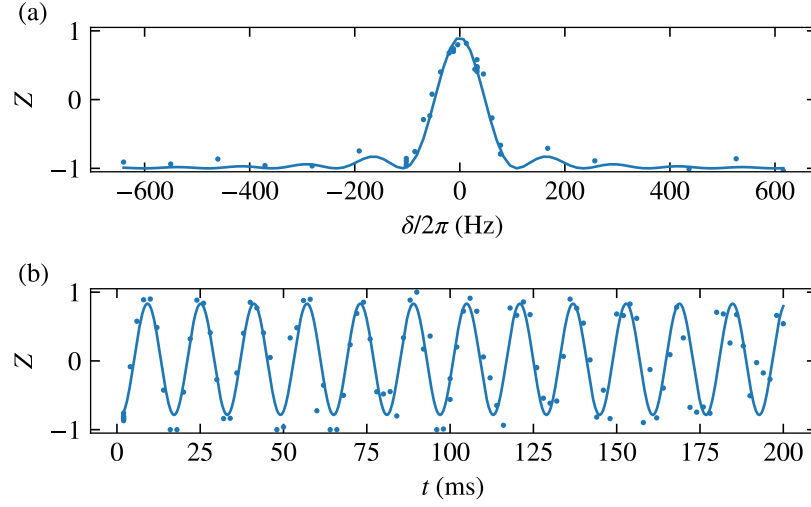


Figure 4.1: Example calibration measurement for  $\delta$  (a) and  $\Omega$  (b) on a thermal cloud. In (a), we observe the magnetization after a  $\pi$ -pulse for different detuning and extract the resonant frequency fitting Eq.(2.3). In (b), we drive Rabi oscillation and extract the oscillation frequency of the centre of the cloud by fitting to a sinusoid. We observe the frequency in the center due to the spatial inhomogeneity of the Rabi coupling (cf. Section 2.4.3)

experimental parameter is modified, and this allows to measure  $\Omega$  and  $\delta$  for the same experimental protocol that normally produces the BEC, while ensuring that the system is deep in the Rabi regime ( $\Omega \gg |n_0 \delta g|$ ).

We determine  $\delta$  with a spectroscopic measurement on this thermal cloud. To determine  $\Omega$ , we drive Rabi dynamics on resonance, and observe full-contrast oscillations with hundreds of ms of coherence time (see Section 2.4.4). An example of these calibration measurements is reported in Fig. 4.1.

## Imaging

Since  $R_\rho$  is comparable to our imaging resolution, the in-situ imaging protocol of Chap. 3 is not suitable to observe the transverse distribution of our sample. Therefore, we expand the sample prior to imaging, in order to magnify the radial distribution of the populations. After releasing the atoms from the trap, we let them freely expand for 2 ms (3 ms) before the state  $|\downarrow\rangle$  ( $|\uparrow\rangle$ ) is imaged. The state-selective imaging is performed by transferring atoms to the imaging state  $|2, 0\rangle$  with a resonant microwave pulse and then performing absorption imaging along the vertical direction. Different expansion times for the two states are necessary for the camera readout and to allow for the atoms of the first image to exit the field-of-view of the camera. Right after the first image, in fact, a pulse of resonant light from the  $x$  direction blows the atoms in the imaging state away.



Due to the different expansion times the atomic clouds have a different radial dimension (see Fig. 4.2a,b). We consider that each cloud is radially expanding following the Castin-Dum equation  $R_\rho(t) = R_\rho(0)\sqrt{1 + \omega_\rho^2 t^2}$  [137]. This equation considers that, during the initial expansion, the mean field energy of the sample is converted into kinetic energy. While this relation holds for an expanding single-component condensate, we expect it to hold also for a two-component system, even in the presence of magnetic excitations. In fact, due to the large energy difference between the density and spin mean-field energy, the former dominates the expansion at short times. In the presence of magnetic excitations only, therefore, the expansion of the sample is nearly equal to the one of a single-component condensate. The expansion at longer times is instead ballistic, and by scanning the expansion time we checked that the Thomas-Fermi radius of the total density and the distribution of each component indeed expand linearly in time, also in the presence of spin excitations. We then rescale the second image along  $y$  in order to account for the spin-dependent expansion time, to measure the magnetization profile of the sample after the expansion. It should be noted that, due to the absorption imaging technique, we observe the radial direction column-integrated along the direction of imaging ( $z$ ), hence we do not observe the true radial distribution in Fig. 4.2. Since the expansion times are much shorter than  $1/\omega_x$ , the axial motion of the sample is negligible, allowing for imaging of the radial distribution as a function of the  $x$  coordinate.

### Spin dimensionality

We then proceed to observe the population distribution after a pulse of duration  $t = \pi/\Omega$  ( $\pi$ -pulse). Fig. 4.2 shows the distributions of both components for a sample with 1D dynamics (a) and one with 3D dynamics (b). In the first case,  $R_\rho/\xi_s = 1.2$  and the population remains self-trapped near the center where the density is sufficiently high. In the second case  $R_\rho/\xi_s = 4.9$ , there is transfer of population also at the center and the radial distribution is clearly inhomogeneous. To ensure self-trapping both in the 1D and 3D case, we set  $\Omega \approx 0.3n_0\delta g/\hbar$ . In Fig. 4.2c, we report the radial magnetization near  $x = 0$  as we vary  $R_\rho/\xi_s$ . For  $R_\rho/\xi_s \lesssim 3$ , the sample remains self-trapped, showing that the spin dynamics is one-dimensional. At larger values, the transfer of population indicates the three-dimensionality of the spin dynamics and the failing of the single-mode approximation. In the rest of the Section, we consider samples with  $R_\rho/\xi_s < 3$ , such that their spin dynamics is one-dimensional. Therefore, referring to Section 1.3.4, the non-linear term of the Josephson dynamics will be expressed with the one-dimensional quantities  $\kappa$  and  $\tilde{n}$ , and the peak value of the linear density is  $\tilde{n}_0$ . Along the  $x$  axis, instead, the size of the condensate  $R_x$  is always much larger than  $\xi_s$ , therefore we consider Josephson dynamics as local (at least for short-time evolutions).

#### 4.1.2 Spectroscopic density shift

In dense atomic clouds, the energy levels are modified by the presence of mean-field interactions, and these frequency shifts, commonly known as collisional shifts, have great importance in metrology [53]. In the Josephson regime, when the non-linear detuning

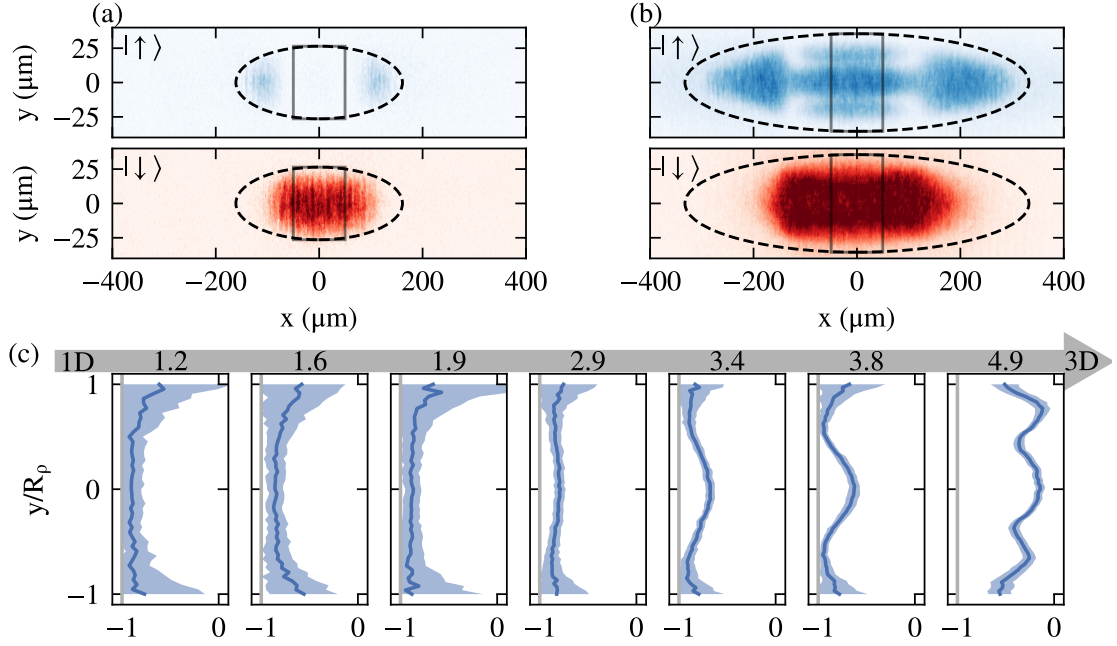


Figure 4.2: ODs of the two components after applying a  $\pi$ -pulse to an elongated sample initially in  $|\downarrow\rangle$ , with 1D (a) and a 3D (b) spin dynamics.  $R_\rho/\xi_s$  are 1.6 and 4.9, respectively. For 1D spin dynamics, the central region at  $x = 0$  is self-trapped for any  $y$ . If the dynamics is 3D, the regions of lower density along the transverse direction are not self-trapped. (c) Magnetization along  $y$  averaged along  $x$ , after a  $\pi$ -pulse for different values of  $R_\rho/\xi_s$  (values are reported above the plots). Confidence interval due to imaging shot-noise of one standard deviation is indicated as shaded region. The averaging region is 100  $\mu\text{m}$ -wide (grey boxes in plot a and b).

and the Rabi coupling are of the same order of magnitude, these shifts can become dramatic. In our system, moreover, the non-linear detuning depends on the local value of the density.

Starting from a fully polarized sample in  $|\downarrow\rangle$ , we apply a  $\pi$ -pulse with Rabi coupling of  $\Omega = 2\pi \times 126 \text{ Hz}$  and observe that the population transferred to  $|\uparrow\rangle$  depends on the (global) detuning  $\delta$  and on the (local) spatially-varying nonlinear coupling strength  $\kappa\tilde{n}(x)$  (see Fig. 4.3a). The experiment is repeated for different values of the detuning  $\delta$  from the transition frequency and we measure the local magnetization of the sample (Fig. 4.3b).

On the edges of the cloud the density is low, therefore the non-linear effects can be neglected and the system is deep in the Rabi regime. Hence the amount of transferred population depends on the detuning  $\delta$  according to the common sinc-like spectroscopic curve (orange points and curve in Fig. 4.3c). At the center of the cloud the non-linear term is no longer negligible and the system is in the Josephson regime (blue points

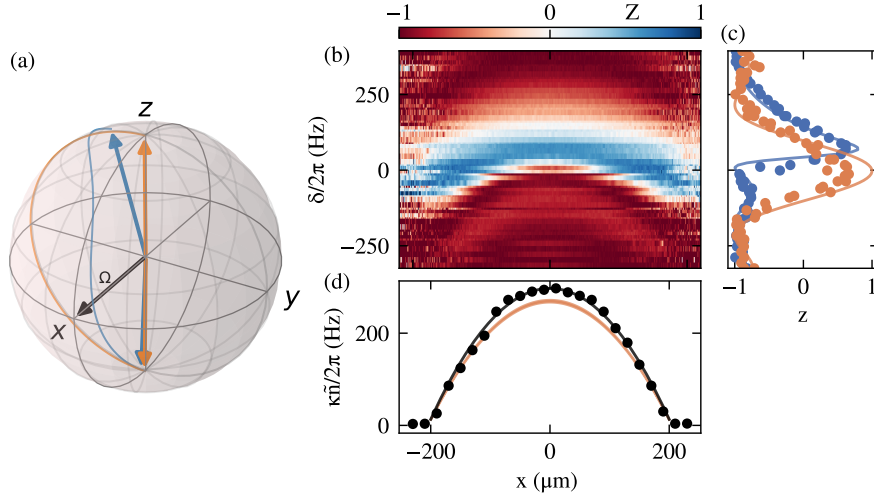


Figure 4.3: (a) Spin evolution during a  $\pi$ -pulse for negligible (orange) and non-negligible (blue) non-linear coupling strength, compared to the Rabi coupling  $\Omega$  (black). (b) Magnetization after a  $\pi$ -pulse as function of  $\delta$ . The center of the cloud is at  $x = 0$  and  $R_x = 200 \mu\text{m}$ . (c) Magnetization for high- (blue,  $x = -20 \mu\text{m}$  to  $20 \mu\text{m}$ ) and low-density (orange,  $|x| = 180 \mu\text{m}$  to  $200 \mu\text{m}$ ) regions of (a), with corresponding fit of the Josephson dynamics (lines). (d) Local  $\kappa\tilde{n}$  at different positions (points). The data well follow a Thomas-Fermi profile (black line) with fixed TF radius (measured on the total atomic density) and amplitude equal to the peak value of  $\kappa\tilde{n}_0/2\pi = 297(15) \text{ Hz}$ . The values of  $\kappa\tilde{n}$  expected from the atomic density and Eq. 1.55 are systematically lower (orange region). Error bars coming from the fit in (b) are smaller than symbol size.

Fig. 4.3c). The spectroscopic curve, obtained by numerical integration of the Josephson equations, becomes asymmetric and its peak is shifted. The direction and magnitude of the shift depends on the sign and magnitude of  $\kappa\tilde{n}$ , respectively, permitting to fit the numerical solution of the Josephson equations (blue line) to the data, with  $\kappa\tilde{n}$  as the only free parameter. By performing this fit on the magnetization observed at different  $x$  we extract the spatial dependence of the local value of the non-linear coupling strength. The obtained values (points in Fig. 4.3c) are in good agreement with the expected Thomas-Fermi profile of the cloud (black line). The measured peak value is  $\kappa\tilde{n}_0/2\pi = 297(15) \text{ Hz}$ . The non-linear coupling strength can be calculated from the atomic density from Eq. (1.55). We estimate the latter from the condensate number and the trapping frequency, finding a systematically lower value (orange line), presumably because of systematic errors in determining the atom number.

### 4.1.3 Density-dependent ARP

When observing the magnetization of Fig. 4.3b, one understands how we cannot prepare a state of spatially uniform magnetization in the regime  $\Omega \sim \kappa\tilde{n}$  by pulsing the Rabi

coupling. In the presence of a spatially inhomogeneous non-linear term, in fact, the exact preparation is possible only in the Rabi regime. A different approach is based on the Adiabatic Rapid Passage (ARP), that was used, for example, in Chap. 3. We now investigate how the non-linear term affects this procedure.

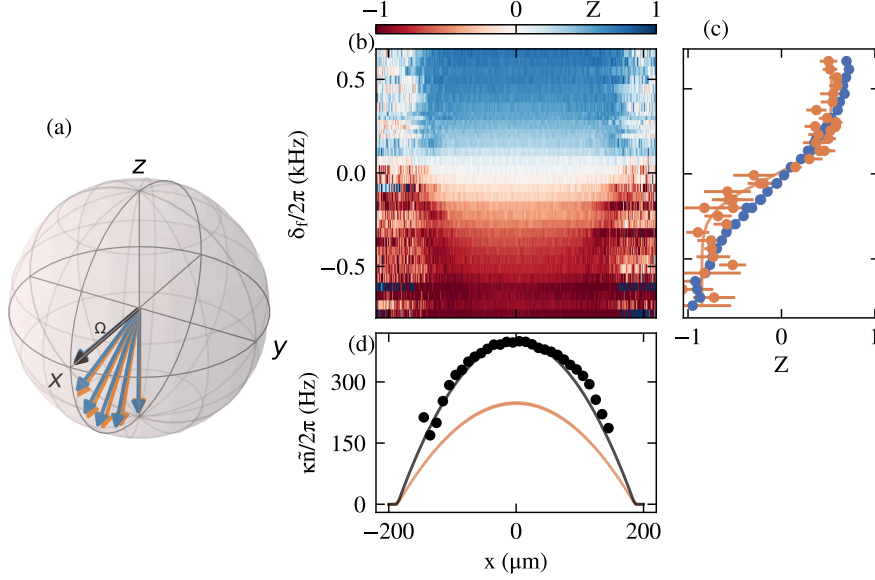


Figure 4.4: (a) Spin evolution during a ARP for negligible (orange) and non-negligible (blue) non-linear coupling strength. (b) Magnetization after a ARP as a function of the final detuning  $\delta_f$ . (c) Magnetization for high- (blue,  $x = -20 \mu\text{m}$  to  $20 \mu\text{m}$ ) and low-density (orange,  $x = -150 \mu\text{m}$  to  $-130 \mu\text{m}$ ) regions. Errorbars are standard deviation in the integrated region. Line is a sigmoidal function fitted to the data. (d) Non-linear parameter extracted from the sigmoidal fit (points). We show a Thomas-Fermi profile (black line) with fixed TF radius (measured on the total atomic density) and amplitude equal to the peak value  $\kappa\tilde{n}_0/2\pi = 398(7)$  Hz. The values of  $\kappa\tilde{n}$  expected from the atomic density and Eq. 1.55 are systematically lower (orange region).

In the ARP, the Rabi coupling is applied to a polarized state with an initial large detuning  $\delta$ , so that the system is in the state of minimum energy. The detuning is then slowly swept, so that the system adiabatically follows the change of  $\delta$  and remains in the energy minimum state. During the ramp,  $\delta$  and  $Z$  satisfy the following condition

$$\delta = \Omega \frac{Z}{\sqrt{1 - Z^2}} + \kappa\tilde{n}Z, \quad (4.2)$$

while  $\phi = 0$  during the whole passage, corresponding to the energy minimum state. This relation can be obtained setting to zero the derivative in  $Z$  of Eq. (1.40). While in the Rabi regime the magnetization depends only on  $\Omega/\delta$ , in the Josephson regime an additional term containing  $\kappa\tilde{n}$  is present. For large values of the detuning, the state

of minimum energy is strongly polarized in both regimes. As  $\delta$  approaches 0, in the Josephson regime the non-linear term brings the magnetization closer to 0, with respect to the Rabi regime. The value  $Z = 0$ , however, is reached for  $\delta = 0$ , independently of the non-linear coupling strength (Fig. 4.4a). It should be noted how the magnetization at  $\delta = 0$  is less sensitive to magnetic field fluctuations, since the state of equal magnetization is favoured by the non-linear term. In a quantum description of the system, this phenomenon produces number-squeezing [66]. Expanding Eq. (4.2) near  $Z = 0$ , one gets the sensitivity of the magnetization

$$\frac{\partial Z}{\partial \delta} = \frac{1}{\Omega + \kappa\tilde{n}}, \quad (4.3)$$

that can be used to measure  $\kappa\tilde{n}$ .

In our experiment, we start from a polarized sample in  $|\downarrow\rangle$ , turn on a coupling with  $\Omega = 2\pi \times 185$  Hz with an initial large detuning  $\delta \approx -2\pi \times 3$  kHz. We then sweep the detuning while keeping constant microwave frequencies and ramping in 50 ms the magnetic field on a half-Gaussian trajectory. The final value of the ramp corresponds to a final  $\delta_f$ . In Fig. 4.4b I plot the magnetization of the sample as a function of the coordinates  $x$  and  $\delta_f$ .

At the beginning of the ramp, all parts of the cloud are close to  $|\downarrow\rangle$ . The magnetization evolves differently in different parts of the system, according to the local value of  $\kappa\tilde{n}$ . As expected, though, all parts of the cloud reach  $Z = 0$  simultaneously when  $\delta = 0$ . Proceeding further with the ramp, the cloud is transferred to  $|\uparrow\rangle$ . Comparing the magnetization as a function of  $\delta$  in different regions of the cloud (Fig. 4.4c), the magnetization transits from  $-1$  to  $+1$  over a larger range of  $\delta$  in regions of higher density. Note that the efficiency of the full rotation is increased by the non-linear term, due to the faster precession of the spin-vector around the coupling vector (see also next Section).

By fitting the dynamics of the magnetization for each position with a sigmoidal function, we extract the derivative in the vicinity of zero magnetization and compute  $\kappa\tilde{n}$  as a function of  $x$  from Eq. (4.3). The peak value of the non-linear term derived from the ARP procedure is  $\kappa\tilde{n}_0/2\pi = 398(7)$  Hz and results larger than the one coming from spectroscopic measurements and the atomic density. However, we expect this method to have larger systematic errors, due to the need to precisely image both states with the same efficiency and due to the not complete adiabaticity of the process. In a late stage of the writing of this Thesis, we improved the ARP procedure by turning on the coupling with a 10 ms linear ramp, instead than abruptly.

#### 4.1.4 Plasma oscillations

The ground state of the Josephson Hamiltonian at  $\delta = 0$  is  $Z = 0$ ,  $\phi = 0$ , and for small deviations near this point the system oscillates at the plasma frequency (see Section 1.3.2)

$$\omega_p = \sqrt{\Omega(\Omega + \kappa\tilde{n})}, \quad (4.4)$$

allowing to determine  $\kappa\tilde{n}$  from independent measurements of  $\Omega$  and  $\omega_p$ . The advantage of this method over the previous ones is the high precision and the immunity to systematic errors related to imaging, as the only quantities to be determined are frequencies.

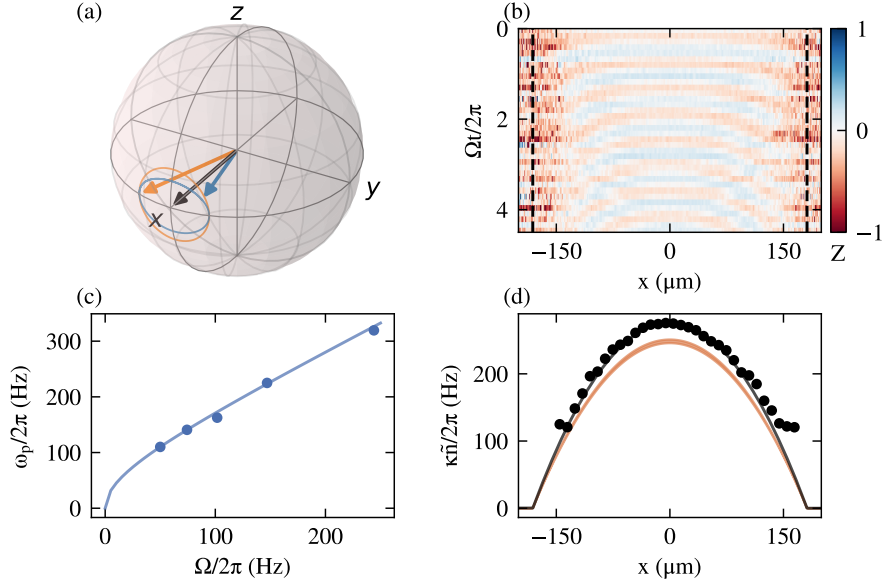


Figure 4.5: (a) The plasma oscillations are orbits near the  $x$ -axis, close to the vector  $\Omega \hat{x}$ . (b) Evolution of the magnetization for the initial state  $Z = 0$ ,  $\phi = 0.1\pi$ , showing position-dependent plasma oscillations. (c) Plasma oscillation frequency at  $x = 0$  for different values of  $\Omega$ . The line is a fit according to Eq. (4.4), hence providing the  $\kappa\tilde{n}$  parameter at the position where the plasma frequency is measured. (d) Local non-linear parameter extracted from plasma oscillation frequency. We show a Thomas-Fermi profile (black line) with fixed TF radius (measured on the total atomic density) and amplitude equal to the peak value  $\kappa\tilde{n}_0/2\pi = 276(3)$  Hz. The values of  $\kappa\tilde{n}$  expected from the atomic density and Eq. 1.55 are systematically lower (orange region).

Following the previously described ARP procedure, the sample is prepared in  $Z = 0, \phi = 0$ . Then, the phase of the coupling is suddenly changed by  $0.1\pi$ , triggering the oscillatory dynamics (Fig. 4.5b). For each position  $x$ , we extract the frequency of the oscillation by fitting the magnetization to a sinusoid. From Eq. (4.4), we extract the value of the local non-linear parameter (Fig. 4.5d). This method works well near the center of the cloud, where we can extract the peak value of  $\kappa\tilde{n}_0/2\pi = 276(3)$  Hz with a relative error on the order of 2%. Near the edges of the cloud, instead, the oscillation is less visible due to the lower signal-to-noise ratio caused by the small change of magnetization and the lower optical density. However, together with the measurement of  $R_x$  from the absorption images, we can fully and accurately measure  $\kappa\tilde{n}(x)$ , as we checked that it follows the expected Thomas-Fermi profile with the spectroscopic measurement.

To check the validity of the method, we repeat the procedure for different values of  $\Omega$ . After the ARP, performed at fixed  $\Omega$ , we change the detuning  $\Delta$  from the virtual state together with the phase. By extracting the oscillation frequency at the center of the cloud we measure the dependence of the plasma frequency on  $\Omega$  (Fig. 4.5c). The

data is compatible with Eq. (4.4), and by fitting the data to this equation with  $\kappa\tilde{n}$  as free parameter, we obtain higher immunity to systematic errors. This method is used to calibrate  $\kappa\tilde{n}$  in the rest of this Chapter and in [138].

## 4.2 Breaking of magnetic heterostructures

In the previous Section, we considered the spin of the sample as evolving with a purely local Josephson dynamics, as if the atoms of the sample were fixed in space. If the spin of the sample becomes inhomogeneous, however, the movement of the atoms causes orbital dynamics of the spin. The description of local Josephson dynamics is now insufficient and we must introduce the orbital motion as a quantum-torque term (cf. Section 1.3.4). In this Section, I present experimental results on the breaking of magnetic interfaces due to quantum-torque.

### 4.2.1 Analogy with magnetic materials

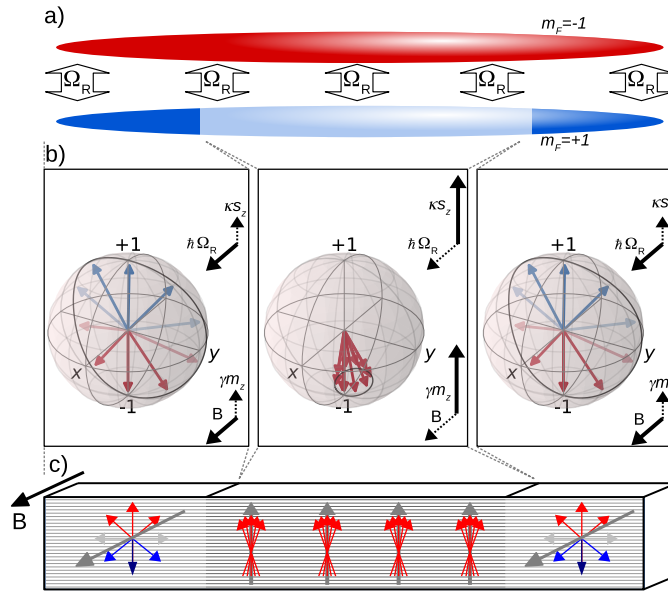


Figure 4.6: An elongated internal Josephson junction (a) mimics a magnetic material with variable ferromagnetic anisotropy (c). The Rabi coupling  $\Omega$  and the non-linear detuning  $\kappa s_z$  are analogous to an external magnetic field  $B$  and the ferromagnetic anisotropy  $\gamma m_z$ . In the regions of low atomic density (left and right), the non-linear field is smaller than the Rabi coupling and the spin precess around the latter. Correspondingly, the magnetic anisotropy is smaller than the external magnetic field and the magnetization precess around the latter. In the regions of high atomic density (center), the opposite happens. The spin is self-trapped around a finite value, while the magnetization is aligned around the direction of preferred magnetization.



The different kind of evolutions of the magnetization evolving under the LLE in a magnetic material are similar to the different dynamical regimes of a spin evolving under the Josephson equation. Fig. 4.6 represents schematically this analogy for an elongated sample with inhomogeneous density.

Considering only the local dynamics, in a magnetic material the evolution is governed by the external magnetic field and the non-linear ferromagnetic anisotropy. A magnetic anisotropic material has some preferred directions of magnetization, and this property can originate for example from the crystalline structure or from the shape of the material. A material with a single preferred magnetization direction has uniaxial magnetic anisotropy, and the effective magnetic field of this material contains a term proportional to the magnetization along this direction. The uniaxial magnetic anisotropy is commonly referred to as *easy-plane* or *easy-axis*, respectively when the magnetization energy is higher or lower in the preferred direction. In an internal bosonic Josephson junction, the external magnetic field corresponds to the electromagnetic Rabi coupling and the uniaxial magnetic anisotropy to the non-linear detuning  $\kappa s_z$ . When the external magnetic field is larger than the magnetic anisotropy, the magnetization precesses around the external field. Similarly, when the Rabi coupling is larger than the non-linear term, the spin precesses around the coupling vector. In the opposite case, when the magnetic anisotropy is larger than the external field, the magnetization precesses around a preferential spatial direction characteristic of the magnetic material. Similarly, when the non-linear term is larger than the Rabi coupling, the spin vector can become self-trapped at a finite value. In the case of mixtures of  $^{23}\text{Na}$  in  $|1, \pm 1\rangle$ , the term  $\kappa$  is positive, therefore this system mimics a magnetic anisotropy of the easy-plane type.

#### 4.2.2 Breaking of magnetic interfaces

##### Breaking of local Josephson dynamics

We shall now consider how this analogy is applied to the elongated Josephson junction characterized in the previous Sections. Due to the spatially inhomogeneous density of the BEC, also the non-linear term of the local Josephson dynamics depends on space as

$$\kappa \tilde{n}(x) = \kappa \tilde{n}_0 (1 - x^2/R_x^2). \quad (4.5)$$

This is analogous to a magnetic material with a space-varying magnetic anisotropy (see Fig. 4.7a). Consequently, if  $\Omega$  is smaller than  $|\kappa \tilde{n}_0|$  the local Josephson dynamics can be in different dynamical regimes at different positions, even if the magnetization is initially homogeneous. The numerical integration of the local Josephson dynamics of a sample that is initially fully polarized in  $Z = -1$  is shown in Fig. 4.7b. Where the density is high, such that  $\Omega < |\kappa \tilde{n}|/2$ , the system is in the self-trapped dynamical regime, the magnetization remains close to  $-1$  and the relative phase runs without bound. The regions where  $\Omega > |\kappa \tilde{n}|/2$ , instead, are in the oscillating dynamical regime, with magnetization and relative phase oscillating around zero. Inside each region the dynamics is approximatively uniform, however the dynamical regimes are separated by a domain wall, at position  $x_c$  such that  $\Omega = |\kappa \tilde{n}(x)|/2$ . At the interface the dynamics sharply



changes characteristics, with different average magnetization and relative-phase on the two sides. Moreover, due to the divergence of the period of the orbits at the domain wall, as time passes the system accumulates features of smaller and smaller size in the vicinity of the domain wall. Clearly, the accumulation of these highly-energetic features cannot proceed indefinitely because of the increasing kinetic energy cost. Therefore, these features must break the strictly local Josephson dynamics.

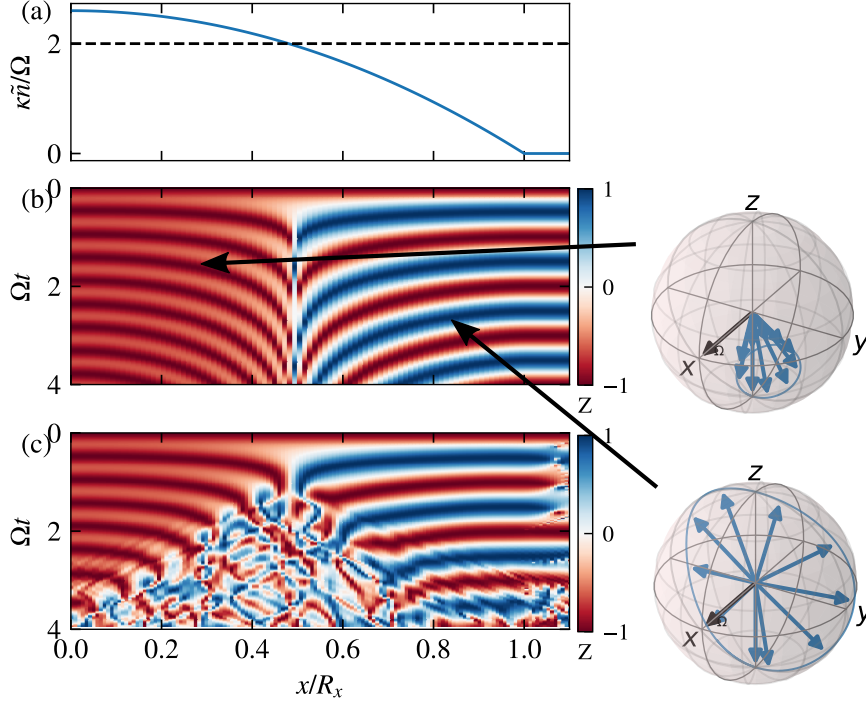


Figure 4.7: (a) The non-linear term  $\kappa\tilde{n}$  of the sample has spatial Thomas-Fermi distribution. The value  $\kappa\tilde{n}/\Omega = 2$  marks the separation between the self-trapped and the oscillating region of the initially polarized sample. (b) Local Josephson dynamics for an initially polarized sample, as function of time. At the domain wall between the self-trapped and the oscillating regimes the dynamics changes abruptly. On the right, the magnetization dynamics in each region is represented on a Bloch sphere. (c) Breaking of the domain wall due to spin-torque. This numerical simulation is from [138]. From the domain wall magnetization excitations originate and disrupt the local Josephson dynamics. All data of the picture are numerical simulations.

We now consider also the orbital degree of freedom of the spin, i.e., the movement of the atoms along the axis of the system. In a magnetic material the Heisenberg exchange leads to the introduction of a term proportional to the Laplacian of the magnetization. Equivalently, in an internal Josephson junction, the motion of the atoms introduces the quantum torque term discussed in Section 1.3.4. These terms introduce an energy cost in “twisting” spatially the magnetization (spin), and become predominant at the domain

wall. In Fig. 4.7c, the quantum torque is added to the numerical simulation and disrupts the local Josephson dynamics, breaking the domain wall into short-wavelength strongly polarized magnetic excitations. This data is adapted from [138] and produced by A. Gallemí. The excitations spread from the domain wall in to the surrounding regions and thorough the sample, as the system started from a very out-of-equilibrium initial condition and has a large amount of excess energy.

As a final remark, it should be noted that in real magnetic materials a strong Gilbert damping term is present. It aligns the magnetization to the effective magnetic field. The dynamics of a low-temperature BEC instead is mainly dissipation-less, hence excluding damping mechanisms.

### Experimental observation of domain wall breaking

We experimentally investigate the breaking of the magnetic interface in our elongated Josephson junction. Starting from a BEC in  $|\downarrow\rangle$ , we suddenly apply a coupling  $\Omega < |\kappa\tilde{n}_0|/2$  to  $|\uparrow\rangle$ , at  $\delta = 0$ . We determine  $\kappa\tilde{n}_0$  using the method described in Section 4.1.4. In Fig. 4.8 we show the results for a sample of  $\approx 5 \times 10^5$  atoms and trapping frequencies  $[\omega_x, \omega_\rho]/2\pi = [10(1) \text{ Hz}, 1006(1) \text{ Hz}]$ . The corresponding Thomas-Fermi radii are  $R_x = 210 \mu\text{m}$  and  $R_\rho = 2.2 \mu\text{m}$ , and the ratio  $R_\rho/\xi_s = 2.8$ . We apply a coupling of  $\Omega = 2\pi \times 118(1) \text{ Hz} = 0.33 \kappa\tilde{n}_0$ . In such a way, the cloud is self trapped from the center to  $x_c \approx 110(7) \mu\text{m}$ . The uncertainty of this value is evaluated from the uncertainties in  $\kappa\tilde{n}_0$  and  $R_x$  and shown as black bars on the top of Fig. 4.8a. We apply the coupling for a variable time  $t$  and then measure the population in each state (see Section 4.1.1). For this experimental parameters the spin dynamics is one-dimensional, hence all the quantities in this Section are integrated along the transverse direction and are presented as a function only of the axial dimension  $x$ .

We show the evolution of the magnetization as a function of time in Fig. 4.8a, with each row of the image being the magnetization in an experimental run. At short times, the two distinct dynamical regions are clearly visible, separated by a magnetic domain wall. At larger times the domain wall breaks into short-wavelength magnetic excitations, creating a strongly fluctuating region that then spread thorough the sample.

To highlight the fluctuating region, we calculate the standard deviation of the magnetization in  $5 \mu\text{m}$ -wide windows (Fig. 4.8b). Even if the magnetization has different values in the self-trapped and oscillating region, its standard deviation has approximately the same (low) value. In the fluctuating region, instead, the standard deviation has a larger and strongly fluctuating value. We perform a 1DGPE simulation for the same experimental parameters of the experiment (Fig. 4.8c,d), that is qualitatively in agreement with the experimental results. Fig. 4.8e-g show the linear densities of the components at different evolution times, and Fig. 4.8h-j the corresponding simulated ones. From these figures one observes how the short-wavelength magnetic excitations start to spread from the position of the domain wall. The agreement within simulation and experiment is remarkable in the region of local Josephson dynamics.

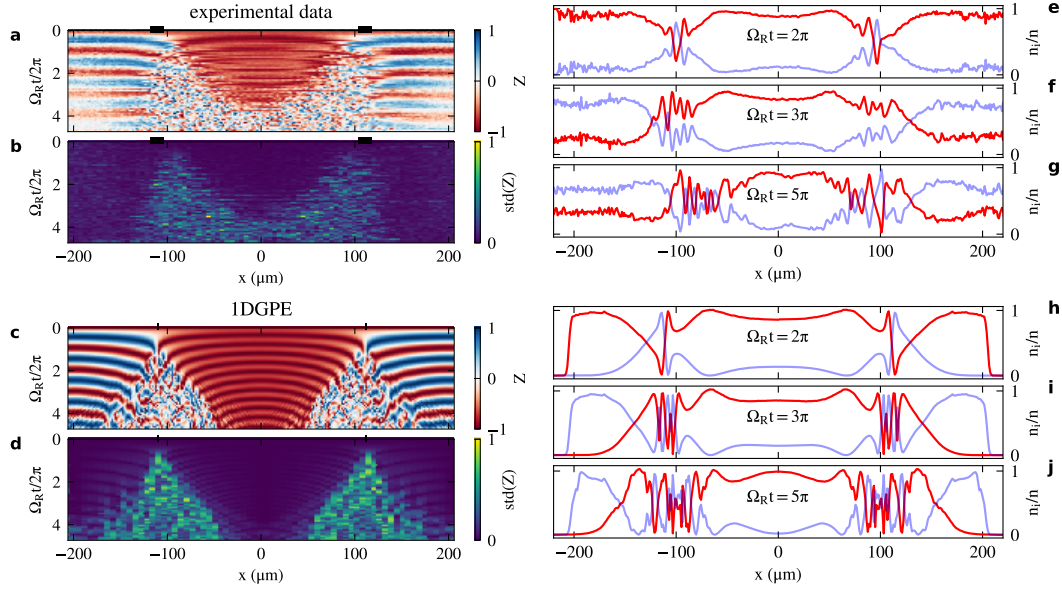


Figure 4.8: (a) Observed magnetization as a function of time for an initially polarized sample in the presence of coupling ( $\Omega = 0.33 \kappa \tilde{n}_0$ ). (b) Standard deviation of the magnetization for spatial windows of  $5 \mu\text{m}$ . (c,d) Numerical Gross-Pitaevskii simulation of the same system. Around the critical position  $x_c$  (black bars), we observe a net change in the behaviour from the oscillating to the self-trapped regime. (e-g) and (h-j) Measured and simulated density profile of each component, normalized to the local total density, for  $\Omega_R t = 2\pi, 3\pi$  and  $5\pi$ .

### Scan of the Rabi coupling

The initial position of the magnetic domain wall depends on the value of the Rabi coupling  $\Omega$ . By changing the value of  $\Omega$ , we investigate the behaviour of magnetic excitations for different initial positions of the domain wall. For low values of the coupling (Fig. 4.9a), the domain wall is formed close to the Thomas-Fermi radius of the sample, and the fluctuating region reaches the center of the self-trapped region after a longer time. As the coupling is increased (Fig. 4.9b,c), the domain wall is formed closer to the center, and the self-trapped region is consumed faster. Finally, when the coupling is greater than  $\kappa \tilde{n}_0 / 2$  (Fig. 4.9d), the sample is completely in the Rabi oscillating region. In this case we also observe creation of short-wavelength magnetic excitations, even in the absence of a domain wall. Differently than the domain-wall breaking case, the excitations originate simultaneously in a wide region at the center of the cloud. We suppose they are originated from the quantum-torque since, due to the density-dependent frequency of oscillation, the magnetization becomes inhomogeneous. On the other hand, numerical simulations indicates that the excitations induced by the quantum torque in this regime should appear at much longer times. For even higher values of the coupling, instead, the magnetic excitations are suppressed.

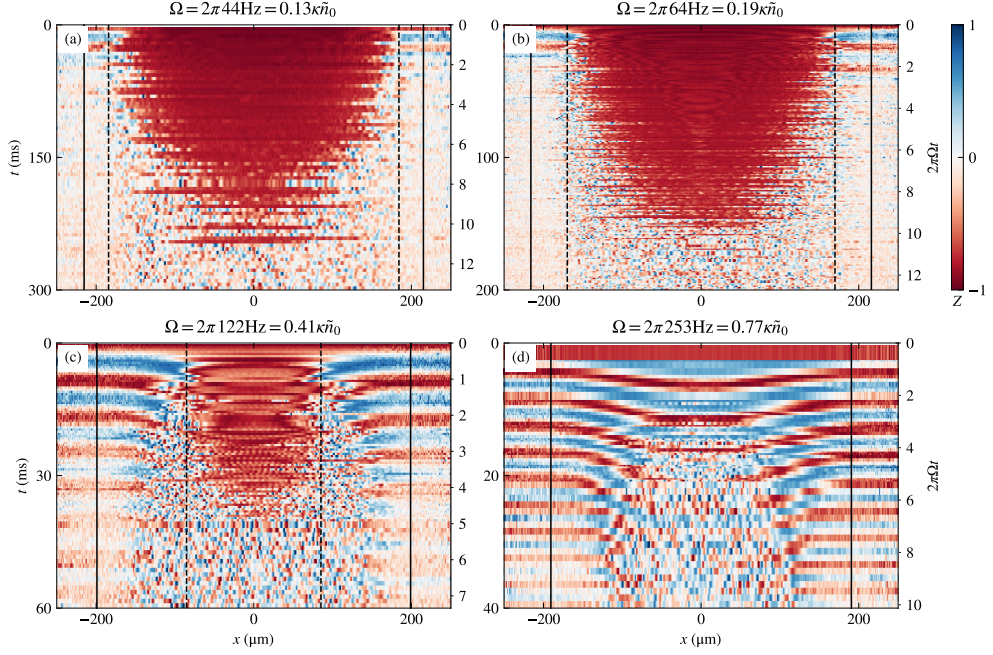


Figure 4.9: (a-c) Evolution of the magnetization of an initially polarized sample for different values of Rabi coupling. As the coupling is increased, the domain-wall position  $x_c$  (black dashed line), calculated from  $\kappa\tilde{n}_0$  and  $R_x$ , moves from the TF radius (black solid line) closer to the center, reducing the time of the spread of the magnetic fluctuation. In (d), the sample is completely in the Rabi oscillating regime.

It should be noted that the initial position of the domain-wall depends not only on  $\Omega$  and  $\kappa\tilde{n}(x)$ , but also on  $\delta$  (see Fig. 4.3). Therefore, shot-to-shot magnetic field fluctuations affect the measurement and their contribution is larger for small values of the coupling. The data presented in this Section was taken at an earlier stage of the experimental activity, with lower values of  $\kappa\tilde{n}_0$  and  $\Omega$  than the data in the previous Section, hence increasing the sensitivity to magnetic field fluctuations.

### 4.2.3 Velocity of the wavefront

The breaking of the magnetic domain walls generates a strongly fluctuating region that spreads into the self-trapped region. In Fig. 4.8(b,d), the “wavefront” of the fluctuating region moves with approximatively constant velocity. For each spatial position, the standard deviation of the magnetization has a transition from a low (self-trapped region) to a high value (fluctuating region) (see Fig. 4.10a,b). We empirically determine the time  $t_j$  of the transition from one condition to the other by fitting a sigmoidal function (black line) and taking its center (black dot) as time of passage of the wavefront. From the  $(x, t_j)$  points, we determine the velocity of the wavefront (Fig. 4.10c, dashed line) to be, for this particular dataset, 4.1(1) mm/s. We compare this velocity with the sound velocity

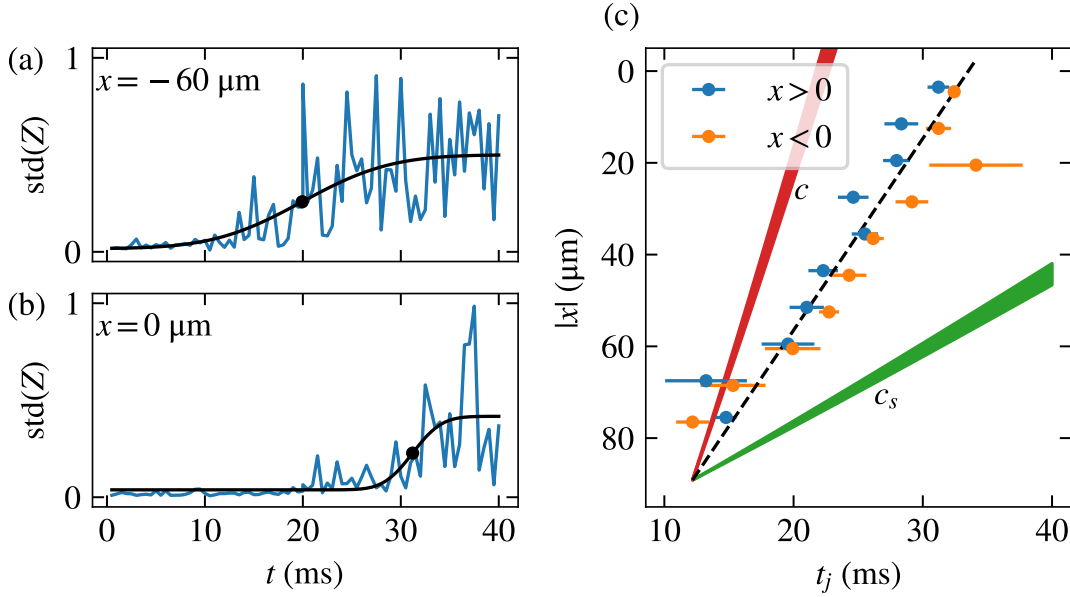


Figure 4.10: (a,b) Standard deviation of the magnetization (blue) as function of time for different positions  $x$  in the sample. We determine the time  $t_j$  (black dot) of the jump from self-trapped to fluctuating dynamics with a sigmoidal fit (black). (c) Velocity of the fluctuating region from the sigmoidal fit. The region spreads from the domain walls at  $x \approx \pm 110 \mu\text{m}$  towards the center of the sample at  $x = 0$  with approximatively constant velocity of  $4.1(1) \text{ mm/s}$  (black dashed line). Red and green lines indicates spread at the sound and spin-sound velocity, respectively.

$c = 9.2 \text{ mm/s}$  and the spin-sound velocity  $c_s = 1.7 \text{ mm/s}$ . We calculate this quantities at the center of the cloud since the density at  $x = \pm 80 \mu\text{m}$  is only 15% lower than the peak value.

Waves travelling faster than the sound velocity of the fluid are known as shock waves, and are typically non-linear waves that abruptly change the property of the fluid itself. Shock waves in single component BECs have been studied, for example, in [139, 140, 141]. Since the wavefront moves faster than the spin-sound velocity, it forms a magnetic shock wave, that have been so far only theoretically investigated for two-components BECs in the absence of coherent coupling [70, 142] and in the presence of spin-orbit coupling [143].

#### 4.2.4 Correlation length

We select portions of the data in the three dynamical regions of the sample and analyse the magnetization (Fig. 4.11a). In the self-trapped and Rabi oscillating regions, the magnetization is spatially uniform, while having different mean value due to the different Josephson dynamics. In the strongly fluctuating region, instead, the magneti-

ization changes apparently randomly from shot to shot and, in the same experimental realization, in space.

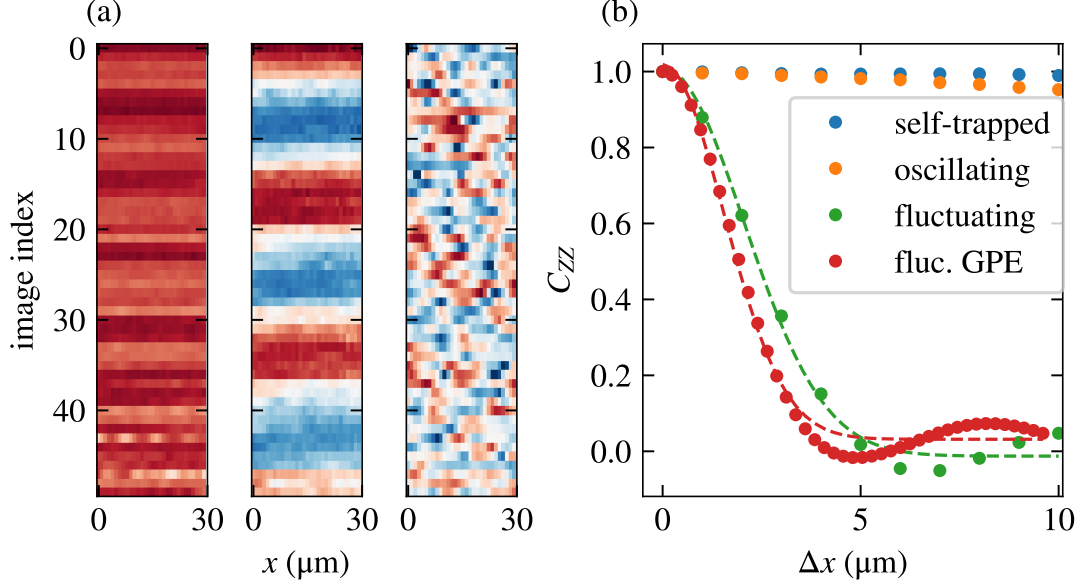


Figure 4.11: (a) From left to right, magnetization of the sample in the self-trapped, Rabi oscillating and fluctuating regions. (b) Autocorrelation  $C_{ZZ}$  of the magnetization in the corresponding regions of experimental data and for a numerical simulation, as a function of the separation  $\Delta x$ .

We measure the autocorrelation of the magnetization

$$C_{ZZ}(\Delta x) = \frac{\int Z(x)Z(x + \Delta x) dx}{\int Z(x)^2 dx} \quad (4.6)$$

in each region separately (Fig. 4.11b). Due to their near-uniform dynamics, the self-trapped and Rabi oscillating regions show strong autocorrelation at long distances. In the fluctuating region instead, the autocorrelation drops to zero after  $\approx 5 \mu\text{m}$ . The autocorrelation of the magnetization, in the fluctuating region of a 1DGPE numerical simulation with the same parameters as the experiment, shows a similar behaviour. To compare the experimental result with the numerics, we fit the autocorrelations in the fluctuating regions to a Gaussian, and measure their standard deviation. The values of  $2.1(1) \mu\text{m}$  (experimental) and  $1.55(3) \mu\text{m}$  (numerical) are qualitatively similar but incompatible given the error bars. In calculating the autocorrelation of the numerical experiment, we take into account the contribution of the finite imaging resolution, however the ballistic expansion before the imaging protocol is not taken into account and may contribute to the larger value of the experimental autocorrelation. The (spatial) dimension of the region considered is limited to  $30 \mu\text{m}$ , with limit set by the largest region with uniform dynamics of the sample.



## 4.2.5 3D system

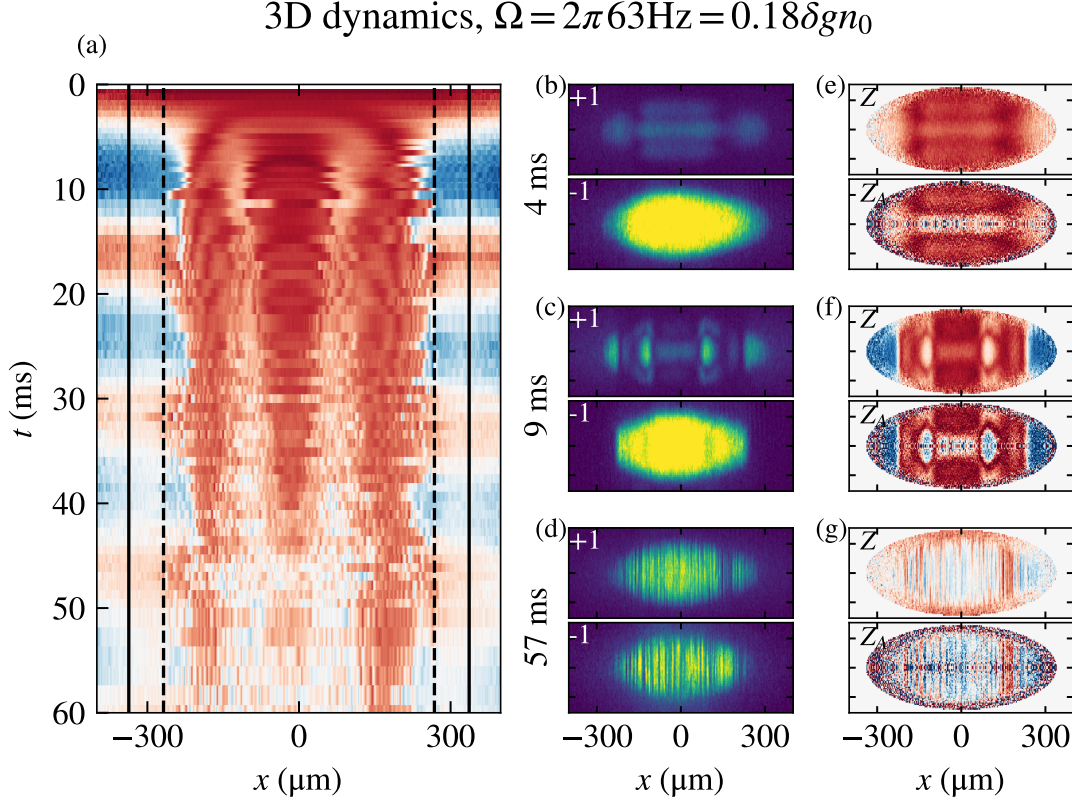


Figure 4.12: (a) Evolution of the magnetization  $Z(x)$  ( $Z(x,y)$  integrated along  $y$ ) for a sample with 3D spin dynamics. Experimental ODs (b-d), column-integrated magnetization  $Z(x,y)$  (e-g, top) and magnetization after inverse-Abel transform  $Z_A(x,\rho)$  (e-g, bottom) at evolution times of 4, 9 and 57 ms. At short times, the system is self-trapped for  $|x| < x_c$  (black dashed lines) and Rabi oscillating elsewhere. Differently from the 1D-dynamics case, even inside the self-trapped region some population is transferred, and short-wavelength magnetic excitations develop. A closer look at the ODs shows that even at short time the 3D spin dynamics break the self-trapping. At longer times short-wavelength magnetic excitations spread everywhere in the sample.

The discussion in this Chapter so far has been limited, with appropriate choice of experimental parameters, to samples with one-dimensional spin dynamics. By increasing the ratio  $R_\rho/\xi_s$  of the sample, however, the spin dynamics becomes three-dimensional, and in a preliminary stage of this work we observed such 3D spin dynamics. We did not perform a detailed investigation of this condition, but I report an example of experimental data with  $R_\rho/\xi_s \approx 5$ , as a starting point for further investigations.

A sample with 3D spin dynamics poses some additional challenges for the experi-

mentalist. First, determining the distribution of the components in the presence of 3D dynamics is more complicated than in the 1D case. In particular, the imaging resolution of our apparatus does not allow us to observe features below the radial size of the sample. The imaging procedure of Section 4.1.1 relied on ballistic expansion to magnify the radial direction. This ballistic expansion along the radial direction might then alter the observed component distribution from the in-situ one.

Second, we cannot consider the dynamics at a position  $x$  in the local Josephson approximation, hence the calibration and preparation techniques of Section 4.1 cannot be applied. In particular, due to 3D spin dynamics we observed that the magnetization  $Z(x)$  after a  $\pi$ -pulse is incompatible with the numerical integration of the Josephson equation (see Fig. 4.3). We observe that the ARP procedure can still be used successfully for state preparation. To determine the non-linear parameter  $n(\mathbf{r})\delta g/\hbar$ , the three-dimensional counterpart to  $\kappa\tilde{n}(x)$ , one could use the plasma frequency and Eq. (4.4), however we observed a reduced, but not negligible, radial-dependence of the magnetization dynamics during a plasma oscillation. Due to this, for 3D samples we calculated the value of the non-linear parameter from the atomic density. We corrected the atomic density from absorption imaging, in a sample with 1D spin dynamics, such that  $\kappa\tilde{n}_0$  from Eq. (4.4) and Eq. (1.55) coincide.

In Fig. 4.12 we report experimental data resulting from applying the protocol of the previous Sections on a sample with  $R_\rho/\xi_s = 4.3$ . Specifically, we prepare a sample with non-linear parameter at its center of  $n\delta g/\hbar = 2\pi \times 350$  Hz and apply the coupling  $\Omega = 2\pi \times 63$  Hz, such that most of the cloud is in the self-trapped regime. Observing the magnetization integrated along the radial directions (Fig. 4.12a), at short times one observes as expected the self-trapped and Rabi oscillating regimes. At  $t = 10$  ms, however, the dynamics in the self-trapped region is different with respect to the 1D case, with a large transfer of population concentrated at two positions  $x \approx \pm 100 \mu\text{m}$ . At even longer times, from these positions are generated short-wavelength magnetic excitations, that disrupt the self-trapped dynamics much sooner than in the 1D case (cf. Fig. 4.9).

To explain this change in dynamics, we must observe the OD of the components before integrating along the radial direction in Fig. 4.12(b-d). We show the components separately after rescaling of the  $y$ -axis. The  $|\uparrow\rangle$  component, that should be only minimally populated in the self-trapped region, instead shows a population with inhomogeneous radial distribution even when the coupling is applied only for 4 ms. In particular, we observe  $|\uparrow\rangle$  population at the center of the cloud, where the sample should be deeper in the self-trapped region. We suspect that either this component is converted at the (radial) edge of the sample and then migrates to the center, or the imaged distribution does not coincide with the in-situ one. At longer times, complex structures develop in the components, with non-trivial dependence on the axial and radial position. The structure concentrates the  $|\uparrow\rangle$  population at the  $x \approx \pm 100 \mu\text{m}$  position, from where the short-wavelength magnetic excitations develop. At longer times, the magnetic excitations have spread everywhere in the sample. These excitations appear mostly one-dimensional along the  $x$  axis, however we occasionally observe tilted excitations that we speculate may be the magnetic analogue of solitonic vortices [134].



Finally, in Fig. 4.12(e-g), we show the magnetization extracted from the distributions of the components. Due to the absorption imaging procedure, the observed distributions are integrated along the imaging direction, hence the observed magnetization  $Z(x, y)$  (top panels) is also similarly integrated. To extract the three-dimensional magnetization profile, it is necessary to reconstruct the 3D density distribution of each component from the column-integrated ones. Assuming cylindrical symmetry around the  $x$  axis, we use the inverse-Abel transform method [144, 145], in the particular implementation used in [146]. With this method, we reconstruct the three-dimensional density distribution  $n_{\pm 1}(x, \rho)$  of each component, from the column-integrated one  $n_{\pm 1}(x, y)$ . From the distributions, we extract the magnetization as

$$Z_A(x, \rho) = \frac{n_{+1}(x, \rho) - n_{-1}(x, \rho)}{n_{+1}(x, \rho) + n_{-1}(x, \rho)}, \quad (4.7)$$

shown in the lower plot of Fig. 4.12(e-g). Observing in particular  $Z_A$  in Fig. 4.12f, one observes how the population is transferred nearly completely to the state  $|\uparrow\rangle$  at some positions inside the self-trapped regions.

Due to limited time, we did not perform a in-detail investigation of the spin dynamics in this regime. However, the measurements show how studies of spin dynamics in two and three dimensions are accessible in our apparatus. In higher dimensions, in fact, interesting physical phenomena have been theoretically predicted, for example magnetic domain-wall formation and vortex confinement [147, 148].



# Conclusions

In this Thesis I reported the results obtained during the course of my Ph.D. in the realization and study of spin dynamics in two-component quantum mixtures of  $^{23}\text{Na}$  atoms in the  $|F = 1, m_F = \pm 1\rangle$  hyperfine states.

I realized and characterized a new experimental apparatus to realize ultracold atomic samples in a highly-stable magnetic field. This apparatus enables the study of coherently-coupled quantum mixtures of internal states with different magnetic moments in a previously inaccessible parameter regime, namely where the strength of the coherent coupling is comparable to the energy of the spin excitations. I then studied solitonic spin waves (Magnetic Solitons) in an equally-populated sample in  $|F = 1, m_F = \pm 1\rangle$ , in the absence of coherent coupling. I deterministically created solitons and observed their dynamics on a timescale of the order of the second, and their robustness to collisions with other solitons. Finally, I realized coherently-coupled two-component BECs with effectively one dimensional spin dynamics, realizing an elongated internal bosonic Josephson junction. In this system, I studied analogues to magnetic heterostructures realized in material science, observing the creation and breaking of spontaneously-created magnetic interfaces by the quantum torque effect.

This work prepares the way toward furthers studies of the spin dynamics in the  $|F = 1, m_F = \pm 1\rangle$  mixture. With the degree of control achieved, new experimental investigations in the presence of coherent coupling are possible. For example, solitonic topological excitations in one-dimensional systems [69], or dynamical instabilities at finite momenta of the self-trapped state [149]. In higher dimensionality systems, an intriguing phenomenon is the formation of bound states of magnetic vortices [147, 148, 150]. This phenomenon has analogies with the quark confinement of QCD, allowing for the simulation of high-energy physics in Bose-Einstein condensates.



# Bibliography

- [1] Chunlei Qu, Lev P. Pitaevskii, and Sandro Stringari. “Magnetic Solitons in a Binary Bose-Einstein Condensate”. In: *Phys. Rev. Lett.* 116.16 (Apr. 2016), p. 160402. DOI: [10.1103/PhysRevLett.116.160402](#) (cit. on pp. [2](#), [13](#), [23](#), [63](#)).
- [2] Lev Pitaevskii and Sandro Stringari. *Bose-Einstein Condensation and Superfluidity*. Oxford University Press, Jan. 2016. DOI: [10.1093/acprof:oso/9780198758884.001.0001](#) (cit. on pp. [6–8](#), [15](#), [18](#)).
- [3] L. Salasnich, A. Parola, and L. Reatto. “Effective wave equations for the dynamics of cigar-shaped and disk-shaped Bose condensates”. In: *Phys. Rev. A* 65.4 (Apr. 2002), p. 043614. DOI: [10.1103/PhysRevA.65.043614](#) (cit. on p. [8](#)).
- [4] Panayotis G. Kevrekidis, Dimitri J. Frantzeskakis, and Ricardo Carretero-González, eds. *Emergent Nonlinear Phenomena in Bose-Einstein Condensates*. Vol. 45. Atomic, Optical, and Plasma Physics. Berlin, Heidelberg: Springer Berlin Heidelberg, 2008. DOI: [10.1007/978-3-540-73591-5](#) (cit. on pp. [8](#), [13](#)).
- [5] Hermann A Haus and William S Wong. “Solitons in optical communications”. In: *Rev. Mod. Phys.* 68.2 (Apr. 1996), pp. 423–444. DOI: [10.1103/RevModPhys.68.423](#) (cit. on pp. [8](#), [66](#)).
- [6] K E Lonngren. “Soliton experiments in plasmas”. In: *Plasma Phys.* 25.9 (Sept. 1983), pp. 943–982. DOI: [10.1088/0032-1028/25/9/001](#) (cit. on p. [8](#)).
- [7] Francesco Ancilotto et al. “First Observation of Bright Solitons in Bulk Superfluid 4He”. In: *Phys. Rev. Lett.* 120.3 (Jan. 2018), p. 035302. DOI: [10.1103/PhysRevLett.120.035302](#) (cit. on p. [8](#)).
- [8] Francisco R. Villatoro. “Nonlinear Gravitational Waves and Solitons”. In: *Underst. Complex Syst.* Springer Verlag, 2018, pp. 207–240. DOI: [10.1007/978-3-319-66766-9\\_7](#) (cit. on p. [8](#)).
- [9] Toshio Tsuzuki. “Nonlinear waves in the Pitaevskii-Gross equation”. In: *J. Low Temp. Phys.* 4.4 (Apr. 1971), pp. 441–457. DOI: [10.1007/BF00628744](#) (cit. on p. [8](#)).

- [10] S Burger et al. “Dark Solitons in Bose-Einstein Condensates”. In: *Phys. Rev. Lett.* 83.25 (Dec. 1999), pp. 5198–5201. DOI: [10.1103/PhysRevLett.83.5198](#) (cit. on pp. 8, 73).
- [11] J Denschlag. “Generating Solitons by Phase Engineering of a Bose-Einstein Condensate”. In: *Science* (80-. ). 287.5450 (Jan. 2000), pp. 97–101. DOI: [10.1126/science.287.5450.97](#) (cit. on pp. 8, 73).
- [12] L. Khaykovich et al. “Formation of a Matter-Wave Bright Soliton”. In: *Science* (80-. ). 296.5571 (May 2002), pp. 1290–1293. DOI: [10.1126/science.1071021](#) (cit. on p. 9).
- [13] J Sanz et al. “Interaction control and bright solitons in coherently-coupled Bose-Einstein condensates”. In: *arXiv* (2019). arXiv: [1912.06041 \[cond-mat.quant-gas\]](#) (cit. on p. 9).
- [14] B. Eiermann et al. “Dispersion Management for Atomic Matter Waves”. In: *Phys. Rev. Lett.* 91.6 (Aug. 2003), p. 060402. DOI: [10.1103/PhysRevLett.91.060402](#) (cit. on p. 9).
- [15] A M Kamchatnov et al. “Nonlinear polarization waves in a two-component Bose-Einstein condensate”. In: *Phys. Rev. A* 89.3 (Mar. 2014), p. 033618. DOI: [10.1103/PhysRevA.89.033618](#) (cit. on pp. 9, 13).
- [16] A. Mosk et al. “Mixture of ultracold lithium and cesium atoms in an optical dipole trap”. In: *Appl. Phys. B* 73.8 (Dec. 2001), pp. 791–799. DOI: [10.1007/s003400100743](#) (cit. on p. 9).
- [17] G. Modugno. “Bose-Einstein Condensation of Potassium Atoms by Sympathetic Cooling”. In: *Science* (80-. ). 294.5545 (Nov. 2001), pp. 1320–1322. DOI: [10.1126/science.1066687](#) (cit. on p. 9).
- [18] Tetsu Takekoshi et al. “Ultracold Dense Samples of Dipolar RbCs Molecules in the Rovibrational and Hyperfine Ground State”. In: *Phys. Rev. Lett.* 113.20 (Nov. 2014), p. 205301. DOI: [10.1103/PhysRevLett.113.205301](#) (cit. on p. 9).
- [19] Bo Huang et al. “Breathing mode of a Bose-Einstein condensate repulsively interacting with a fermionic reservoir”. In: *Phys. Rev. A* 99.4 (Apr. 2019), p. 041602. DOI: [10.1103/PhysRevA.99.041602](#) (cit. on p. 9).
- [20] Cheng-Hsun Wu et al. “Ultracold Fermionic Feshbach Molecules of  $^{23}\text{Na}$ - $^{40}\text{K}$ ”. In: *Phys. Rev. Lett.* 109.8 (Aug. 2012), p. 085301. DOI: [10.1103/PhysRevLett.109.085301](#) (cit. on p. 9).
- [21] F. Ferlaino et al. “Dipolar oscillations in a quantum degenerate Fermi Bose atomic mixture”. In: *J. Opt. B Quantum Semiclassical Opt.* 5.2 (Apr. 2003), S3–S8. DOI: [10.1088/1464-4266/5/2/351](#) (cit. on p. 9).
- [22] Z. Hadzibabic et al. “Fiftyfold Improvement in the Number of Quantum Degenerate Fermionic Atoms”. In: *Phys. Rev. Lett.* 91.16 (Oct. 2003), p. 160401. DOI: [10.1103/PhysRevLett.91.160401](#) (cit. on p. 9).

- 
- [23] F. Schreck et al. “Quasipure Bose-Einstein Condensate Immersed in a Fermi Sea”. In: *Phys. Rev. Lett.* 87.8 (Aug. 2001), p. 080403. DOI: [10.1103/PhysRevLett.87.080403](#) (cit. on p. 9).
  - [24] I. Ferrier-Barbut et al. “A mixture of Bose and Fermi superfluids”. In: *Science* (80-. ). 345.6200 (Aug. 2014), pp. 1035–1038. DOI: [10.1126/science.1255380](#) (cit. on p. 9).
  - [25] M. Taglieber et al. “Quantum Degenerate Two-Species Fermi-Fermi Mixture Coexisting with a Bose-Einstein Condensate”. In: *Phys. Rev. Lett.* 100.1 (Jan. 2008), p. 010401. DOI: [10.1103/PhysRevLett.100.010401](#) (cit. on p. 9).
  - [26] E. Wille et al. “Exploring an ultracold Fermi-Fermi mixture: Interspecies Feshbach resonances and scattering properties of 6Li and 40K”. In: *Phys. Rev. Lett.* 100.5 (Nov. 2007), p. 053201. DOI: [10.1103/PhysRevLett.100.053201](#) (cit. on p. 9).
  - [27] D. S. Hall et al. “Dynamics of Component Separation in a Binary Mixture of Bose-Einstein Condensates”. In: *Phys. Rev. Lett.* 81.8 (Aug. 1998), pp. 1539–1542. DOI: [10.1103/PhysRevLett.81.1539](#) (cit. on pp. 9, 14).
  - [28] C. J. Myatt et al. “Production of Two Overlapping Bose-Einstein Condensates by Sympathetic Cooling”. In: *Phys. Rev. Lett.* 78.4 (Jan. 1997), pp. 586–589. DOI: [10.1103/PhysRevLett.78.586](#) (cit. on p. 9).
  - [29] M. D. Barrett, J. A. Sauer, and M. S. Chapman. “All-Optical Formation of an Atomic Bose-Einstein Condensate”. In: *Phys. Rev. Lett.* 87.1 (June 2001), p. 010404. DOI: [10.1103/PhysRevLett.87.010404](#) (cit. on p. 9).
  - [30] G. Semeghini et al. “Self-Bound Quantum Droplets of Atomic Mixtures in Free Space”. In: *Phys. Rev. Lett.* 120.23 (June 2018), p. 235301. DOI: [10.1103/PhysRevLett.120.235301](#) (cit. on pp. 9, 11).
  - [31] J. Stenger et al. “Spin domains in ground-state Bose-Einstein condensates”. In: *Nature* 396.6709 (Nov. 1998), pp. 345–348. DOI: [10.1038/24567](#) (cit. on pp. 10, 14).
  - [32] Tin-Lun Ho. “Spinor Bose Condensates in Optical Traps”. In: *Phys. Rev. Lett.* 81.4 (July 1998), pp. 742–745. DOI: [10.1103/PhysRevLett.81.742](#) (cit. on p. 10).
  - [33] Seji Kang et al. “Observation of Wall-Vortex Composite Defects in a Spinor Bose-Einstein Condensate”. In: *Phys. Rev. Lett.* (2019), pp. 1–9. DOI: [10.1103/PhysRevLett.122.095301](#) (cit. on p. 10).
  - [34] E. M. Bookjans, A. Vinit, and C. Raman. “Quantum Phase Transition in an Antiferromagnetic Spinor Bose-Einstein Condensate”. In: *Phys. Rev. Lett.* 107.19 (Nov. 2011), p. 195306. DOI: [10.1103/PhysRevLett.107.195306](#) (cit. on p. 10).
  - [35] Xin-Yu Luo et al. “Deterministic entanglement generation from driving through quantum phase transitions”. In: *Science* (80-. ). 355.6325 (Feb. 2017), pp. 620–623. DOI: [10.1126/science.aag1106](#) (cit. on p. 10).

- [36] M. S. Chang et al. “Observation of Spinor Dynamics in Optically Trapped 87Rb Bose-Einstein Condensates”. In: *Phys. Rev. Lett.* 92.14 (Apr. 2004), p. 140403. DOI: [10.1103/PhysRevLett.92.140403](https://doi.org/10.1103/PhysRevLett.92.140403) (cit. on p. 10).
- [37] H. Schmaljohann et al. “Dynamics and thermodynamics in spinor quantum gases”. In: *Appl. Phys. B* 79.8 (Dec. 2004), pp. 1001–1007. DOI: [10.1007/s00340-004-1664-6](https://doi.org/10.1007/s00340-004-1664-6) (cit. on p. 10).
- [38] Dan M. Stamper-Kurn and Masahito Ueda. “Spinor Bose gases: Symmetries, magnetism, and quantum dynamics”. In: *Rev. Mod. Phys.* 85.3 (July 2013), pp. 1191–1244. DOI: [10.1103/RevModPhys.85.1191](https://doi.org/10.1103/RevModPhys.85.1191) (cit. on p. 10).
- [39] D. S. Petrov. “Quantum Mechanical Stabilization of a Collapsing Bose-Bose Mixture”. In: *Phys. Rev. Lett.* 115.15 (Oct. 2015), p. 155302. DOI: [10.1103/PhysRevLett.115.155302](https://doi.org/10.1103/PhysRevLett.115.155302) (cit. on p. 11).
- [40] C. R. Cabrera et al. “Quantum liquid droplets in a mixture of Bose-Einstein condensates”. In: *Science (80-. )*. 359.6373 (2018), pp. 301–304. DOI: [10.1126/science.aao5686](https://doi.org/10.1126/science.aao5686) (cit. on p. 11).
- [41] C. J. Pethick and H. Smith. *Bose-Einstein Condensation in Dilute Gases*. Cambridge: Cambridge University Press, 2008. DOI: [10.1017/CB09780511802850](https://doi.org/10.1017/CB09780511802850) (cit. on p. 11).
- [42] Joon Hyun Kim, Deokhwa Hong, and Yong-il Shin. “Observation of two sound modes in a binary superfluid gas”. In: *Phys. Rev. A* 101.6 (June 2020), p. 061601. DOI: [10.1103/PhysRevA.101.061601](https://doi.org/10.1103/PhysRevA.101.061601) (cit. on p. 12).
- [43] Tom Bienaimé et al. “Spin-dipole oscillation and polarizability of a binary Bose-Einstein condensate near the miscible-immiscible phase transition”. In: *Phys. Rev. A* 94.6 (Dec. 2016), p. 063652. DOI: [10.1103/PhysRevA.94.063652](https://doi.org/10.1103/PhysRevA.94.063652) (cit. on pp. 13, 14).
- [44] Th. Busch and J R Anglin. “Dark-Bright Solitons in Inhomogeneous Bose-Einstein Condensates”. In: *Phys. Rev. Lett.* 87.1 (June 2001), p. 010401. DOI: [10.1103/PhysRevLett.87.010401](https://doi.org/10.1103/PhysRevLett.87.010401) (cit. on p. 13).
- [45] Christoph Becker et al. “Oscillations and interactions of dark and dark-bright solitons in Bose-Einstein condensates”. In: *Nat. Phys.* 4.6 (May 2008), pp. 496–501. DOI: [10.1038/nphys962](https://doi.org/10.1038/nphys962) (cit. on pp. 13, 73).
- [46] M. A. Hoefer et al. “Dark-dark solitons and modulational instability in miscible two-component Bose-Einstein condensates”. In: *Phys. Rev. A* 84.4 (Oct. 2011), p. 041605. DOI: [10.1103/PhysRevA.84.041605](https://doi.org/10.1103/PhysRevA.84.041605) (cit. on p. 13).
- [47] S Komineas and N Papanicolaou. “Solitons, solitonic vortices, and vortex rings in a confined Bose-Einstein condensate”. In: *Phys. Rev. A* 68.4 (Oct. 2003), p. 043617. DOI: [10.1103/PhysRevA.68.043617](https://doi.org/10.1103/PhysRevA.68.043617) (cit. on pp. 13, 64, 83).
- [48] A. Gallemí et al. “Magnetic defects in an imbalanced mixture of two Bose-Einstein condensates”. In: *Phys. Rev. A* 97.6 (June 2018), p. 063615. DOI: [10.1103/PhysRevA.97.063615](https://doi.org/10.1103/PhysRevA.97.063615) (cit. on p. 13).



- 
- [49] A. Muñoz Mateo and J. Brand. “Chladni solitons and the onset of the snaking instability for dark solitons in confined superfluids”. In: *Phys. Rev. Lett.* 113.25 (Dec. 2014), p. 255302. DOI: [10.1103/PhysRevLett.113.255302](https://doi.org/10.1103/PhysRevLett.113.255302) (cit. on p. 13).
  - [50] H. E. Nistazakis et al. “Bright-dark soliton complexes in spinor Bose-Einstein condensates”. In: *Phys. Rev. A* 77.3 (Mar. 2008), p. 033612. DOI: [10.1103/PhysRevA.77.033612](https://doi.org/10.1103/PhysRevA.77.033612) (cit. on p. 13).
  - [51] Stefan Lannig et al. “Collisions of Three-Component Vector Solitons in Bose-Einstein Condensates”. In: *Phys. Rev. Lett.* 125.17 (Oct. 2020), p. 170401. DOI: [10.1103/PhysRevLett.125.170401](https://doi.org/10.1103/PhysRevLett.125.170401) (cit. on p. 13).
  - [52] D. S. Hall et al. “Measurements of Relative Phase in Two-Component Bose-Einstein Condensates”. In: *Phys. Rev. Lett.* 81.8 (Aug. 1998), pp. 1543–1546. DOI: [10.1103/PhysRevLett.81.1543](https://doi.org/10.1103/PhysRevLett.81.1543) (cit. on pp. 14, 15, 69).
  - [53] D M Harber et al. “Effect of cold collisions on spin coherence and resonance shifts in a magnetically trapped ultracold gas”. In: *Phys. Rev. A* 66.5 (Nov. 2002), p. 053616. DOI: [10.1103/PhysRevA.66.053616](https://doi.org/10.1103/PhysRevA.66.053616) (cit. on pp. 14, 93).
  - [54] M Egorov et al. “Measurement of s -wave scattering lengths in a two-component Bose-Einstein condensate”. In: *Phys. Rev. A* 87.5 (May 2013), p. 053614. DOI: [10.1103/PhysRevA.87.053614](https://doi.org/10.1103/PhysRevA.87.053614) (cit. on p. 14).
  - [55] Satoshi Tojo et al. “Controlling phase separation of binary Bose-Einstein condensates via mixed-spin-channel Feshbach resonance”. In: *Phys. Rev. A* 82.3 (Sept. 2010), p. 033609. DOI: [10.1103/PhysRevA.82.033609](https://doi.org/10.1103/PhysRevA.82.033609) (cit. on p. 14).
  - [56] A. Görlitz et al. “Sodium Bose-Einstein Condensates in the F=2 State in a Large-Volume Optical Trap”. In: *Phys. Rev. Lett.* 90.9 (Mar. 2003), p. 090401. DOI: [10.1103/PhysRevLett.90.090401](https://doi.org/10.1103/PhysRevLett.90.090401) (cit. on pp. 14, 51, 72).
  - [57] S. Knoop et al. “Feshbach spectroscopy and analysis of the interaction potentials of ultracold sodium”. In: *Phys. Rev. A* 83.4 (Apr. 2011), p. 042704. DOI: [10.1103/PhysRevA.83.042704](https://doi.org/10.1103/PhysRevA.83.042704) (cit. on p. 14).
  - [58] Marta Abad and Alessio Recati. “A study of coherently coupled two-component Bose-Einstein condensates”. In: *Eur. Phys. J. D* 67.7 (July 2013), p. 148. DOI: [10.1140/epjd/e2013-40053-2](https://doi.org/10.1140/epjd/e2013-40053-2) (cit. on pp. 15, 16).
  - [59] E. Nicklas et al. “Nonlinear dressed states at the miscibility-immiscibility threshold”. In: *Phys. Rev. A* 92.5 (Nov. 2015), p. 053614. DOI: [10.1103/PhysRevA.92.053614](https://doi.org/10.1103/PhysRevA.92.053614) (cit. on pp. 16, 24).
  - [60] Tilman Zibold et al. “Classical Bifurcation at the Transition from Rabi to Josephson Dynamics”. In: *Phys. Rev. Lett.* 105.20 (Nov. 2010), p. 204101. DOI: [10.1103/PhysRevLett.105.204101](https://doi.org/10.1103/PhysRevLett.105.204101) (cit. on pp. 16, 24, 89).
  - [61] Paolo Tommasini et al. “Bogoliubov theory for mutually coherent condensates”. In: *Phys. Rev. A - At. Mol. Opt. Phys.* 67.2 (Feb. 2003), p. 17. DOI: [10.1103/PhysRevA.67.023606](https://doi.org/10.1103/PhysRevA.67.023606) (cit. on p. 16).

- [62] L. Landau and E. Lifshitz. “On the theory of the dispersion of magnetic permeability in ferromagnetic bodies”. In: *Perspect. Theor. Phys.* 1992. DOI: [10.1016/b978-0-08-036364-6.50008-9](#) (cit. on pp. 17, 20).
- [63] V. G. Bar'yakhtar and B. A. Ivanov. “The Landau-Lifshitz equation: 80 years of history, advances, and prospects”. In: *Low Temp. Phys.* 41.9 (2015), pp. 663–669. DOI: [10.1063/1.4931649](#) (cit. on pp. 17, 20).
- [64] B.D. Josephson. “Possible new effects in superconductive tunnelling”. In: *Phys. Lett.* 1.7 (July 1962), pp. 251–253. DOI: [10.1016/0031-9163\(62\)91369-0](#) (cit. on p. 17).
- [65] G. J. Milburn et al. “Quantum dynamics of an atomic Bose-Einstein condensate in a double-well potential”. In: *Phys. Rev. A* 55.6 (June 1997), pp. 4318–4324. DOI: [10.1103/PhysRevA.55.4318](#) (cit. on p. 17).
- [66] M. J. Steel and M. J. Collett. “Quantum state of two trapped Bose-Einstein condensates with a Josephson coupling”. In: *Phys. Rev. A* 57.4 (Apr. 1998), pp. 2920–2930. DOI: [10.1103/PhysRevA.57.2920](#) (cit. on pp. 17, 97).
- [67] I. Marino et al. “Bose-condensate tunneling dynamics: Momentum-shortened pendulum with damping”. In: *Phys. Rev. A* 60.1 (July 1999), pp. 487–493. DOI: [10.1103/PhysRevA.60.487](#) (cit. on p. 19).
- [68] A. V. Chumak et al. “Magnon spintronics”. In: *Nat. Phys.* 11.6 (2015), pp. 453–461. DOI: [10.1038/nphys3347](#) (cit. on p. 20).
- [69] Chunlei Qu et al. “Magnetic solitons in Rabi-coupled Bose-Einstein condensates”. In: *Phys. Rev. A* 95.3 (Mar. 2017), p. 033614. DOI: [10.1103/PhysRevA.95.033614](#) (cit. on pp. 23, 111).
- [70] Thibault Congy, Anatoly Kamchatnov, and Nicolas Pavloff. “Dispersive hydrodynamics of nonlinear polarization waves in two-component Bose-Einstein condensates”. In: *SciPost Phys.* 1.1 (Oct. 2016), p. 006. DOI: [10.21468/SciPostPhys.1.1.006](#) (cit. on pp. 23, 105).
- [71] M. Madami et al. “Direct observation of a propagating spin wave induced by spin-transfer torque”. In: *Nat. Nanotechnol.* 6.10 (Oct. 2011), pp. 635–638. DOI: [10.1038/nnano.2011.140](#) (cit. on p. 23).
- [72] T. Nikuni and J. E. Williams. “Kinetic Theory of a Spin-1/2 Bose-Condensed Gas”. In: *J. Low Temp. Phys.* 133.December (Apr. 2003), pp. 1–6. arXiv: [0304095 \[cond-mat\]](#). URL: <https://link.springer.com/article/10.1023%7B%5C%7D2FA%7B%5C%7D3A1026206724886> (cit. on p. 23).
- [73] E. Nicklas et al. “Observation of Scaling in the Dynamics of a Strongly Quenched Quantum Gas”. In: *Phys. Rev. Lett.* 115.24 (Dec. 2015), p. 245301. DOI: [10.1103/PhysRevLett.115.245301](#) (cit. on p. 24).
- [74] Michael Albiez et al. “Direct Observation of Tunneling and Nonlinear Self-Trapping in a Single Bosonic Josephson Junction”. In: *Phys. Rev. Lett.* 95.1 (June 2005), p. 010402. DOI: [10.1103/PhysRevLett.95.010402](#) (cit. on pp. 24, 89).

- 
- [75] Giacomo Valtolina et al. “Josephson effect in fermionic superfluids across the BEC-BCS crossover”. In: *Science* 350.6267 (2015), pp. 1505–1508. DOI: [10.1126/science.aac9725](https://doi.org/10.1126/science.aac9725) (cit. on p. 24).
  - [76] G Spagnolli et al. “Crossing Over from Attractive to Repulsive Interactions in a Tunneling Bosonic Josephson Junction”. In: *Phys. Rev. Lett.* 118.23 (June 2017), p. 230403. DOI: [10.1103/PhysRevLett.118.230403](https://doi.org/10.1103/PhysRevLett.118.230403) (cit. on pp. 24, 25).
  - [77] F. S. Cataliotti et al. “Josephson junction arrays with Bose-Einstein condensates”. In: *Science* (80-. ). 293.5531 (Aug. 2001), pp. 843–846. DOI: [10.1126/science.1062612](https://doi.org/10.1126/science.1062612) (cit. on p. 24).
  - [78] S. Levy et al. “The a.c. and d.c. Josephson effects in a Bose-Einstein condensate”. In: *Nature* 449.7162 (Oct. 2007), pp. 579–583. DOI: [10.1038/nature06186](https://doi.org/10.1038/nature06186) (cit. on pp. 24, 89).
  - [79] Marine Pigneur et al. “Relaxation to a Phase-Locked Equilibrium State in a One-Dimensional Bosonic Josephson Junction”. In: *Phys. Rev. Lett.* 120.17 (Apr. 2018), p. 173601. DOI: [10.1103/PhysRevLett.120.173601](https://doi.org/10.1103/PhysRevLett.120.173601) (cit. on pp. 24, 25, 89).
  - [80] T. Betz et al. “Two-Point Phase Correlations of a One-Dimensional Bosonic Josephson Junction”. In: *Phys. Rev. Lett.* 106.2 (Jan. 2011), p. 020407. DOI: [10.1103/PhysRevLett.106.020407](https://doi.org/10.1103/PhysRevLett.106.020407) (cit. on pp. 25, 89).
  - [81] S. Raghavan et al. “Coherent oscillations between two weakly coupled Bose-Einstein condensates: Josephson effects, pi oscillations, and macroscopic quantum self-trapping”. In: *Phys. Rev. A* 59.1 (Jan. 1999), pp. 620–633. DOI: [10.1103/PhysRevA.59.620](https://doi.org/10.1103/PhysRevA.59.620) (cit. on p. 25).
  - [82] Jan-Frederik Mennemann et al. “Relaxation in an Extended Bosonic Josephson Junction”. In: *arXiv* (Dec. 2020). arXiv: [2012.05885](https://arxiv.org/abs/2012.05885). URL: <http://arxiv.org/abs/2012.05885> (cit. on pp. 25, 89).
  - [83] C.J. Foot. *Atomic Physics (Oxford Master Series in Atomic, Optical and Laser Physics)*. 2005 (cit. on pp. 27, 70).
  - [84] Eleonora Fava. “Static and dynamics properties of a miscible two-component Bose–Einstein Condensate”. PhD thesis. University of Trento, 2018. URL: <http://eprints-phd.biblio.unitn.it/2789/> (cit. on pp. 28, 29, 31, 34, 35).
  - [85] Giacomo Colzi. “A new apparatus to simulate fundamental interactions with ultracold atoms”. PhD thesis. University of Trento, 2018. URL: <http://eprints-phd.biblio.unitn.it/2869/> (cit. on pp. 28, 35, 36, 48, 49).
  - [86] Immanuel Bloch, Theodor W Hänsch, and Tilman Esslinger. “Atom Laser with a cw Output Coupler”. In: *Phys. Rev. Lett.* 82.15 (Apr. 1999), pp. 3008–3011. DOI: [10.1103/PhysRevLett.82.3008](https://doi.org/10.1103/PhysRevLett.82.3008) (cit. on p. 28).
  - [87] André Kubelka-Lange et al. “A three-layer magnetic shielding for the MAIUS-1 mission on a sounding rocket”. In: *Rev. Sci. Instrum.* 87.6 (June 2016), p. 063101. DOI: [10.1063/1.4952586](https://doi.org/10.1063/1.4952586) (cit. on pp. 28, 29).

- [88] T van Zoest et al. “Bose-Einstein Condensation in Microgravity”. In: *Science* (80-. ). 328.5985 (June 2010), pp. 1540–1543. DOI: [10.1126/science.1189164](https://doi.org/10.1126/science.1189164) (cit. on p. 28).
- [89] B Canuel et al. “Exploring gravity with the MIGA large scale atom interferometer”. In: *Sci. Rep.* 8.1 (Dec. 2018), p. 14064. DOI: [10.1038/s41598-018-32165-z](https://doi.org/10.1038/s41598-018-32165-z) (cit. on p. 28).
- [90] S. J. Smullin et al. “Low-noise high-density alkali-metal scalar magnetometer”. In: *Phys. Rev. A* 80.3 (Sept. 2009), p. 033420. DOI: [10.1103/PhysRevA.80.033420](https://doi.org/10.1103/PhysRevA.80.033420) (cit. on p. 28).
- [91] O.L. Krivanek et al. “An electron microscope for the aberration-corrected era”. In: *Ultramicroscopy* 108.3 (Feb. 2008), pp. 179–195. DOI: [10.1016/j.ultramic.2007.07.010](https://doi.org/10.1016/j.ultramic.2007.07.010) (cit. on p. 28).
- [92] P Mansfield and B Chapman. “Multishield active magnetic screening of coil structures in NMR”. In: *J. Magn. Reson.* 72.2 (Apr. 1987), pp. 211–223. DOI: [10.1016/0022-2364\(87\)90283-6](https://doi.org/10.1016/0022-2364(87)90283-6) (cit. on p. 28).
- [93] Andrea Bertoldi et al. “Magnetoresistive magnetometer with improved bandwidth and response characteristics”. In: *Rev. Sci. Instrum.* 76.6 (June 2005), p. 065106. DOI: [10.1063/1.1922787](https://doi.org/10.1063/1.1922787) (cit. on p. 28).
- [94] Techmfg. *Techmfg website*. URL: <https://www.techmfg.com/products/electric-and-magnetic-field-cancellation/mag-netx> (cit. on p. 28).
- [95] C J Dedman et al. “Active cancellation of stray magnetic fields in a Bose-Einstein condensation experiment”. In: *Rev. Sci. Instrum.* 78.2 (Feb. 2007), p. 024703. DOI: [10.1063/1.2472600](https://doi.org/10.1063/1.2472600) (cit. on p. 29).
- [96] Laura Botti et al. “Noninvasive system for the simultaneous stabilization and control of magnetic field strength and gradient”. In: *Rev. Sci. Instrum.* 77.3 (Mar. 2006), p. 035103. DOI: [10.1063/1.2173846](https://doi.org/10.1063/1.2173846) (cit. on p. 29).
- [97] T. J. Sumner, J. M. Pendlebury, and K. F. Smith. “Convectional magnetic shielding”. In: *J. Phys. D. Appl. Phys.* 20.9 (Sept. 1987), pp. 1095–1101. DOI: [10.1088/0022-3727/20/9/001](https://doi.org/10.1088/0022-3727/20/9/001) (cit. on pp. 29–31, 34).
- [98] Xiao-Tian Xu et al. “Ultra-low noise magnetic field for quantum gases”. In: *Rev. Sci. Instrum.* 90.5 (May 2019), p. 054708. DOI: [10.1063/1.5087957](https://doi.org/10.1063/1.5087957) (cit. on p. 29).
- [99] COMSOL AB. *COMSOL Multiphysics®*. \url{www.comsol.com} (cit. on p. 29).
- [100] Magnetic Shields. *Company page*. URL: <https://magneticshields.co.uk/technical/material-technical-data> (cit. on p. 31).
- [101] Bartington Instruments. *Company website*. URL: <https://www.bartington.com/> (cit. on p. 33).
- [102] Giacomo Colzi et al. “Production of large Bose-Einstein condensates in a magnetic-shield-compatible hybrid trap”. In: *Phys. Rev. A* 97.5 (May 2018), p. 053625. DOI: [10.1103/PhysRevA.97.053625](https://doi.org/10.1103/PhysRevA.97.053625) (cit. on pp. 35, 50).

- 
- [103] J Simpson et al. “Simple Analytic Expressions for the Magnetic Field of a Circular Current Loop”. In: (2001). URL: <https://ntrs.nasa.gov/search.jsp?R=20010038494> (cit. on p. 39).
- [104] Rudolf Grimm, Matthias Weidemüller, and Yurii B. Ovchinnikov. “Optical Dipole Traps for Neutral Atoms”. In: *Adv. At. Mol. Opt. Phys.* Feb. 2000, pp. 95–170. DOI: [10.1016/S1049-250X\(08\)60186-X](https://doi.org/10.1016/S1049-250X(08)60186-X) (cit. on pp. 45, 74).
- [105] *LDC501 Datasheet from the manufacturer*. URL: <https://www.thinksrs.com/downloads/pdfs/catalog/LDC500c.pdf> (visited on 12/21/2020) (cit. on p. 47).
- [106] K. Dieckmann et al. “Two-dimensional magneto-optical trap as a source of slow atoms”. In: *Phys. Rev. A* 58.5 (Nov. 1998), pp. 3891–3895. DOI: [10.1103/PhysRevA.58.3891](https://doi.org/10.1103/PhysRevA.58.3891) (cit. on p. 49).
- [107] G Lamporesi et al. “Compact high-flux source of cold sodium atoms”. In: *Rev. Sci. Instrum.* 84.6 (June 2013), p. 063102. DOI: [10.1063/1.4808375](https://doi.org/10.1063/1.4808375) (cit. on p. 49).
- [108] Wolfgang Ketterle et al. “High densities of cold atoms in a dark spontaneous-force optical trap”. In: *Phys. Rev. Lett.* 70.15 (Apr. 1993), pp. 2253–2256. DOI: [10.1103/PhysRevLett.70.2253](https://doi.org/10.1103/PhysRevLett.70.2253) (cit. on p. 49).
- [109] A Aspect et al. “Laser Cooling below the One-Photon Recoil Energy by Velocity-Selective Coherent Population Trapping”. In: *Phys. Rev. Lett.* 61.7 (Aug. 1988), pp. 826–829. DOI: [10.1103/PhysRevLett.61.826](https://doi.org/10.1103/PhysRevLett.61.826) (cit. on p. 50).
- [110] Giacomo Colzi et al. “Sub-Doppler cooling of sodium atoms in gray molasses”. In: *Phys. Rev. A* 93.2 (Feb. 2016), p. 023421. DOI: [10.1103/PhysRevA.93.023421](https://doi.org/10.1103/PhysRevA.93.023421) (cit. on p. 50).
- [111] D Budker et al. “Resonant nonlinear magneto-optical effects in atoms”. In: *Rev. Mod. Phys.* 74.4 (Nov. 2002), pp. 1153–1201. DOI: [10.1103/RevModPhys.74.1153](https://doi.org/10.1103/RevModPhys.74.1153) (cit. on p. 51).
- [112] Joachim Brand and William P. Reinhardt. “Solitonic vortices and the fundamental modes of the “snake instability”: Possibility of observation in the gaseous Bose-Einstein condensate”. In: *Phys. Rev. A - At. Mol. Opt. Phys.* 65.4 (Apr. 2002), p. 4. DOI: [10.1103/PhysRevA.65.043612](https://doi.org/10.1103/PhysRevA.65.043612) (cit. on pp. 64, 83).
- [113] Peter Wittek and Luca Calderaro. “Extended computational kernels in a massively parallel implementation of the Trotter–Suzuki approximation”. In: *Comput. Phys. Commun.* 197 (Dec. 2015), pp. 339–340. DOI: [10.1016/j.cpc.2015.07.017](https://doi.org/10.1016/j.cpc.2015.07.017) (cit. on p. 65).
- [114] Ling-Zheng Meng, Yan-Hong Qin, and Li-Chen Zhao. *Spin Solitons in Spin-1 Bose-Einstein Condensates*. 2019. arXiv: [1912.00182](https://arxiv.org/abs/1912.00182) [[cond-mat.quant-gas](https://arxiv.org/archive/cond-mat)] (cit. on p. 66).

- [115] Kazuya Fujimoto, Ryusuke Hamazaki, and Masahito Ueda. “Flemish Strings of Magnetic Solitons and a Nonthermal Fixed Point in a One-Dimensional Antiferromagnetic Spin-1 Bose Gas”. In: *Phys. Rev. Lett.* 122.17 (May 2019), p. 173001. DOI: [10.1103/PhysRevLett.122.173001](https://doi.org/10.1103/PhysRevLett.122.173001) (cit. on p. 66).
- [116] D. V. Freilich et al. “Real-Time Dynamics of Single Vortex Lines and Vortex Dipoles in a Bose-Einstein Condensate”. In: *Science* (80-. ). 329.5996 (Sept. 2010), pp. 1182–1185. DOI: [10.1126/science.1191224](https://doi.org/10.1126/science.1191224) (cit. on p. 68).
- [117] Anand Ramanathan et al. “Partial-transfer absorption imaging: A versatile technique for optimal imaging of ultracold gases”. In: *Rev. Sci. Instrum.* 83.8 (Aug. 2012), p. 083119. DOI: [10.1063/1.4747163](https://doi.org/10.1063/1.4747163) (cit. on p. 68).
- [118] C. Mordini et al. “Single-shot reconstruction of the density profile of a dense atomic gas”. In: *Opt. Express* 28.20 (Sept. 2020), p. 29408. DOI: [10.1364/OE.397567](https://doi.org/10.1364/OE.397567) (cit. on p. 68).
- [119] M. R. Matthews et al. “Vortices in a Bose-Einstein Condensate”. In: *Phys. Rev. Lett.* 83.13 (Sept. 1999), pp. 2498–2501. DOI: [10.1103/PhysRevLett.83.2498](https://doi.org/10.1103/PhysRevLett.83.2498) (cit. on p. 69).
- [120] Bruce Shore. *The Theory of Coherent Atomic Excitation*. Vol. 1. Wiley-Interscience, New York, 1990 (cit. on p. 71).
- [121] A. Farolfi et al. “Observation of Magnetic Solitons in Two-Component Bose-Einstein Condensates”. In: *Phys. Rev. Lett.* 125.3 (July 2020), p. 030401. DOI: [10.1103/PhysRevLett.125.030401](https://doi.org/10.1103/PhysRevLett.125.030401) (cit. on p. 73).
- [122] Xiao Chai et al. “Magnetic Solitons in a Spin-1 Bose-Einstein Condensate”. In: *Phys. Rev. Lett.* 125.3 (July 2020), p. 030402. DOI: [10.1103/PhysRevLett.125.030402](https://doi.org/10.1103/PhysRevLett.125.030402) (cit. on p. 73).
- [123] C Hamner et al. “Phase Winding a Two-Component Bose-Einstein Condensate in an Elongated Trap: Experimental Observation of Moving Magnetic Orders and Dark-Bright Solitons”. In: *Phys. Rev. Lett.* 111.26 (Dec. 2013), p. 264101. DOI: [10.1103/PhysRevLett.111.264101](https://doi.org/10.1103/PhysRevLett.111.264101) (cit. on p. 73).
- [124] C. Hamner et al. “Generation of Dark-Bright Soliton Trains in Superfluid-Superfluid Counterflow”. In: *Phys. Rev. Lett.* 106.6 (Feb. 2011), p. 065302. DOI: [10.1103/PhysRevLett.106.065302](https://doi.org/10.1103/PhysRevLett.106.065302) (cit. on p. 73).
- [125] I Danaila et al. “Vector dark-antidark solitary waves in multicomponent Bose-Einstein condensates”. In: *Phys. Rev. A* 94.5 (Nov. 2016), p. 053617. DOI: [10.1103/PhysRevA.94.053617](https://doi.org/10.1103/PhysRevA.94.053617) (cit. on p. 73).
- [126] A. R. Fritsch et al. “Creating solitons with controllable and near-zero velocity in Bose-Einstein condensates”. In: *Phys. Rev. A* 101.5 (May 2020), p. 053629. DOI: [10.1103/PhysRevA.101.053629](https://doi.org/10.1103/PhysRevA.101.053629) (cit. on p. 74).
- [127] HCPhotonics. *Company website*. URL: <https://www.hcphotonics.com/ppln-chips> (cit. on p. 74).



- 
- [128] Pauli Virtanen et al. “SciPy 1.0: fundamental algorithms for scientific computing in Python”. In: *Nat. Methods* 17.3 (Mar. 2020), pp. 261–272. DOI: [10.1038/s41592-019-0686-2](https://doi.org/10.1038/s41592-019-0686-2) (cit. on p. 78).
  - [129] Qimin Zhang and Arne Schwettmann. “Quantum Interferometry with Microwave-dressed F=1 Spinor Bose-Einstein Condensates: Role of Initial States and Long Time Evolution”. In: *Phys. Rev. A* 100.6 (Sept. 2019). DOI: [10.1103/PhysRevA.100.063637](https://doi.org/10.1103/PhysRevA.100.063637) (cit. on p. 80).
  - [130] B P Anderson et al. “Watching Dark Solitons Decay into Vortex Rings in a Bose-Einstein Condensate”. In: *Phys. Rev. Lett.* 86.14 (Apr. 2001), pp. 2926–2929. DOI: [10.1103/PhysRevLett.86.2926](https://doi.org/10.1103/PhysRevLett.86.2926) (cit. on p. 83).
  - [131] I. Shomroni et al. “Evidence for an oscillating soliton/vortex ring by density engineering of a Bose-Einstein condensate”. In: *Nat. Phys.* 5.3 (Jan. 2009), pp. 193–197. DOI: [10.1038/nphys1177](https://doi.org/10.1038/nphys1177) (cit. on p. 83).
  - [132] C. Becker et al. “Inelastic collisions of solitary waves in anisotropic Bose-Einstein condensates: sling-shot events and expanding collision bubbles”. In: *New J. Phys.* 15.11 (Nov. 2013), p. 113028. DOI: [10.1088/1367-2630/15/11/113028](https://doi.org/10.1088/1367-2630/15/11/113028) (cit. on p. 83).
  - [133] Mark J.H. Ku et al. “Cascade of Solitonic Excitations in a Superfluid Fermi gas: From Planar Solitons to Vortex Rings and Lines”. In: *Phys. Rev. Lett.* 116.4 (Jan. 2016), p. 045304. DOI: [10.1103/PhysRevLett.116.045304](https://doi.org/10.1103/PhysRevLett.116.045304) (cit. on p. 83).
  - [134] Simone Donadello et al. “Observation of Solitonic Vortices in Bose-Einstein Condensates”. In: *Phys. Rev. Lett.* 113.6 (Aug. 2014), p. 065302. DOI: [10.1103/PhysRevLett.113.065302](https://doi.org/10.1103/PhysRevLett.113.065302) (cit. on pp. 84, 108).
  - [135] Florin Radu and Hartmut Zabel. *Magnetic Heterostructures; Advances and Perspectives in Spinstructures and Spintransport; Series: Springer Tracts in Modern Physics*. Vol. 227. 2008, pp. 97–184. URL: <https://www.springer.com/gp/book/9783540734611> (cit. on p. 89).
  - [136] N. Locatelli, V. Cros, and J. Grollier. “Spin-torque building blocks”. In: *Nat. Mater.* 13.1 (Dec. 2014), pp. 11–20. DOI: [10.1038/nmat3823](https://doi.org/10.1038/nmat3823) (cit. on p. 89).
  - [137] Y. Castin and R. Dum. “Bose-Einstein Condensates in Time Dependent Traps”. In: *Phys. Rev. Lett.* 77.27 (Dec. 1996), pp. 5315–5319. DOI: [10.1103/PhysRevLett.77.5315](https://doi.org/10.1103/PhysRevLett.77.5315) (cit. on p. 93).
  - [138] Arturo Farolfi et al. “Quantum-torque-induced breaking of magnetic domain walls in ultracold gases”. In: *arXiv* (Nov. 2020). arXiv: [2011.04271](https://arxiv.org/abs/2011.04271). URL: <https://arxiv.org/abs/2011.04271v1> (cit. on pp. 99, 101, 102).
  - [139] M. A. Hoefer et al. “Dispersive and classical shock waves in Bose-Einstein condensates and gas dynamics”. In: *Phys. Rev. A* 74.2 (Aug. 2006), p. 023623. DOI: [10.1103/PhysRevA.74.023623](https://doi.org/10.1103/PhysRevA.74.023623) (cit. on p. 105).

- [140] J. J. Chang, P. Engels, and M. A. Hoefer. “Formation of Dispersive Shock Waves by Merging and Splitting Bose-Einstein Condensates”. In: *Phys. Rev. Lett.* 101.17 (Oct. 2008), p. 170404. DOI: [10.1103/PhysRevLett.101.170404](https://doi.org/10.1103/PhysRevLett.101.170404) (cit. on p. 105).
- [141] Maren E. Mossman et al. “Dissipative shock waves generated by a quantum-mechanical piston”. In: *Nat. Commun.* 9.1 (Dec. 2018), p. 4665. DOI: [10.1038/s41467-018-07147-4](https://doi.org/10.1038/s41467-018-07147-4) (cit. on p. 105).
- [142] S. K. Ivanov et al. “Solution of the Riemann problem for polarization waves in a two-component Bose-Einstein condensate”. In: *Phys. Rev. E* 96.6 (Dec. 2017), p. 062202. DOI: [10.1103/PhysRevE.96.062202](https://doi.org/10.1103/PhysRevE.96.062202) (cit. on p. 105).
- [143] Maren E. Mossman et al. “Shock Waves in a Superfluid with Higher-Order Dispersion”. In: *arXiv* (Apr. 2020). arXiv: [2004.00832](https://arxiv.org/abs/2004.00832). URL: <http://arxiv.org/abs/2004.00832> (cit. on p. 105).
- [144] N. H. Abel. “EUDML — Auflösung einer mechanischen Aufgabe.” In: *J. für die reine und Angew. Math.* 1 (1826). URL: <https://eudml.org/doc/183021> (cit. on p. 109).
- [145] Daniel D. Hickstein et al. “PyAbel (v0.7): A Python Package for Abel Transforms”. In: (Mar. 2016). DOI: [10.5281/ZENODO.47423](https://doi.org/10.5281/ZENODO.47423) (cit. on p. 109).
- [146] Carmelo Mordini. “Measurement of the density profile of quantized vortices and of the equation of state in a 3D interacting Bose gas”. PhD thesis. Università degli studi di Trento, 2019. URL: <http://eprints-phd.biblio.unitn.it/3728/> (cit. on p. 109).
- [147] D. T. Son and M. A. Stephanov. “Domain walls of relative phase in two-component Bose-Einstein condensates”. In: *Phys. Rev. A* 65.6 (June 2002), p. 063621. DOI: [10.1103/PhysRevA.65.063621](https://doi.org/10.1103/PhysRevA.65.063621) (cit. on pp. 109, 111).
- [148] Marek Tylutki et al. “Confinement and precession of vortex pairs in coherently coupled Bose-Einstein condensates”. In: *Phys. Rev. A* 93.4 (Apr. 2016), p. 043623. DOI: [10.1103/PhysRevA.93.043623](https://doi.org/10.1103/PhysRevA.93.043623) (cit. on pp. 109, 111).
- [149] Nathan R Bernier, Emanuele G Dalla Torre, and Eugene Demler. “Unstable Avoided Crossing in Coupled Spinor Condensates”. In: *Phys. Rev. Lett.* 113.6 (Aug. 2014), p. 065303. DOI: [10.1103/PhysRevLett.113.065303](https://doi.org/10.1103/PhysRevLett.113.065303) (cit. on p. 111).
- [150] Minoru Eto and Muneto Nitta. “Confinement of half-quantized vortices in coherently coupled Bose-Einstein condensates: Simulating quark confinement in a QCD-like theory”. In: *Phys. Rev. A* 97.2 (Feb. 2018), p. 023613. DOI: [10.1103/PhysRevA.97.023613](https://doi.org/10.1103/PhysRevA.97.023613) (cit. on p. 111).